Towards a Model System for Lamellar Magnetism by Atomic Layer Deposition

Jon Einar Bratvold

Nanostructures and Functional Materials

Department of Chemistry and

Centre for Material Science and Nanotechnology

Faculty of Mathematics and Natural Sciences

University of Oslo

A dissertation submitted for the degree of

Philosophiae Doctor (Ph.D.)

2018

Cover: Hanne Baadsgaard Utigard.
Print production: Reprosentralen, University of Oslo.

"Few subjects in science are more difficult to understand than magnetism."
-    Encyclopædia Britannica, 15th edition 1989

Acknowledgements

The thesis presented here represents part of the requirements for the degree of Philosophiae Doctor at the Department of Chemistry, Faculty of Mathematics and Natural Sciences, University of Oslo, Norway. Starting in September 2009, the experimental work was carried out at the group for Nanostructures and Functional Materials (NAFUMA) under the supervision of Professor Dr. Ola Nilsen and Professor Helmer Fjellvåg.

Regarding the environment I have worked in, I could not have asked for more. I would like to thank all my past and present colleagues at NAFUMA for creating an inspiring academic environment as well as an enjoyable social milieu. I would also like to thank Suzanne McEnroe, Peter Robinson, Karl Fabian, Hiroshi Okamoto and Chris Thomas for all the (endless) discussions and the great times we shared through the MATERA project.

Lightening up everyday life at work with (occasional) scientific discussions, but most importantly lunch, coffee and hogwash: a big thank you to Amund, Ina, Ingvild, Jon Magnus, Kristian and Øystein.

I am also grateful to my mother, father, sister, brother-in-law and two nieces for their patience and support. The same goes for all my friends outside work—especially my "extended family" Bente, Eivind, Helle and Jon: thank you for providing a mental refuge from studies and work.

Every ph.d. student has supervisors. Luckily, mine have been encouraging and helpful. Thank you, Helmer and Ola, for all your guidance and support, and the opportunities you have given me. Professor Dr. Nilsen deserves special attention. He has gone far beyond his supervising duties, and I have come to know him both as a friend and as an employer. His scientific knowledge is extraordinary, and only eclipsed by his infectious enthusiasm, curiosity and big heart. Motivating me must have felt like a Sisyphean undertaking at times, but you managed to pull me through. For that, you have my biggest gratitude.

Finally, Henrik. I am not sure if this thesis would have been finished without your enormous support, both academically and mentally. We share an interest for all kinds of knowledge, obscure as it may be. I also believe we are masters of the highly unacknowledged art of switching seamlessly between poppycock and rationality. Thank you for all the help you have provided, in all forms. I hope we find time for more mischief and adventures in the future. This is not the end.

II

Abstract

This thesis describes how atomic layer deposition (ALD) can be used to produce model systems of magnetic heterostructures. In particular, one objective has been to mimic naturally formed minerals with multilayers of Fe_2O_3 (hematite) and $FeTiO_3$ (ilmenite) with nanosized dimensions. Such structures exhibit exotic magnetic phenomena, like strong and extremely stable natural remanent magnetization, self-reversed thermoremanent magnetization and exchange bias. The peculiar magnetic properties of these minerals originate from the interfaces of the layered nanostructure rather than from the individual materials themselves. Manufacture of such lamellar structures in a controllable manner is not straightforward. ALD is shown to be a good candidate for the task, as the technique enables deposition of uniform films over larger areas, with excellent control of composition and thickness. A prerequisite for successful ALD growth is well-behaving processes for the individual oxide materials. Direct deposition of $FeTiO_3$ proved challenging, due to lack of an ALD process that yields films containing only divalent iron. As an alternative, a model system with $NiTiO_3$ instead of $FeTiO_3$ was developed to study the effects of interfaces and nanolayering. This in turn, prompted us to establish a process for $NiTiO_3$ by ALD.

The magnetic structure of $NiTiO_3$ is very similar to $FeTiO_3$, however, with magnetic moments aligned perpendicular rather than parallel to the crystallographic c axis. To explore the magnetic phenomena, films with a (001) orientation is desirable, as the cation layers in the natural ilmenite type minerals are stacked along [001]. $NiTiO_3$ films were deposited on several different single crystal substrates and their crystallographic correlation with the substrates have been mapped. Highly epitaxial films of $NiTiO_3$ on Al_2O_3(001) were obtained, as also previously observed in our group for growth of Fe_2O_3 on the same type of substrates.

Based on the processes for producing epitaxial films of Fe_2O_3 and $NiTiO_3$ on Al_2O_3(001) at hand, multilayered structures were deposited. To record magnetic features from the constituents of the multilayered film, single layered samples of Fe_2O_3 and $NiTiO_3$ were also prepared and characterized. Distinct features at low temperature not present in single layered films were observed, but the origin of these features were not conclusively identified.

An Fe(II) precursor completely new to ALD was explored: $Fe(hfa)_2\cdot TMEDA$. Different co-reactants were tested, and a self-limiting process using oxalic acid was established. XPS investigations confirmed the preservation of the +2 oxidation state of Fe from precursor to film. This represents the first direct deposition of solely Fe(II) containing films by ALD. However, this process is not suitable for direct deposition of $FeTiO_3$.

Finally, a multilayered oxide film containing Fe(II) and Ti(IV) was deposited, with the target to obtain $FeTiO_3$ (ilmenite) after post-deposition annealing.

XPS confirmed Fe(II) in the film, and XRD supported the presence of epitaxial $FeTiO_3$ on Al_2O_3(001), after annealing.

The successful formation of $FeTiO_3$ represents one of the two constituents in the natural hematite/ilmenite minerals, while the study of multilayered Fe_2O_3/$NiTiO_3$ films act as a model system to study lamellar magnetism.

Table of contents

1   Introduction

1.1   Marvelous magnetic Modum minerals

While mapping out the mineral deposits of Norway through aeromagnetic investigations in the mid-2000s, researchers from Norwegian Geological Survey (Norges geologiske undersøkelse, NGU) came across large magnetic anomalies in Modum. Irregularities are normally what geologists look for when conducting these kinds of surveys, but the deviations in Modum turned out to be anything but normal. Rock samples from the site were shown to have a strong and extremely stable natural remanent magnetization. As the minerals responsible for the anomalies formed nearly 1 billion years ago, they adopted a direction of magnetization parallel to the magnetic field of the Earth at the time. Since formation, and numerous exposures to heat and pressure through tectonic movement, the minerals retained the direction of its magnetization, unaffected also by changes in the Earth's magnetic field. What could be the origin of such an unusually stable magnetization? The samples from Modum were mainly composed of hematite (α-Fe_2O_3, hereafter referred to as Fe_2O_3) and ilmenite ($FeTiO_3$). Individually, both minerals have an antiferromagnetic structure ($FeTiO_3$ is paramagnetic above 57 K) with magnetic moments ordered antiparallel, cancelling each other out. The moments in Fe_2O_3 are not perfectly antiparallel, making it canted antiferromagnetic, but the net magnetic moment is very small. Trace amounts of ferrimagnetic magnetite (Fe_3O_4) were also present, but the high Curie temperature and the strong coercivity of the rock samples were not consistent with Fe_3O_4. Hence, none of the minerals in the samples could independently explain the magnetic properties of the rocks. The solution, or more correctly: exsolution, was found in-between hematite and ilmenite. At high temperatures, intermediate compositions of $(1-x)Fe_2O_3-(x)FeTiO_3$ exist as solid solutions. Starting from such a solid solution, the rocks from Modum slowly cooled down as they travelled up in the Earth's crust. Upon this cooling, an abundance of ilmenite exsolution lamellae in a larger hematite matrix evolved, the thinnest lamellae being < 1 nm.[1] Lamellae with an odd number of atomic layers and a certain position in the matrix resulted in uncompensated moments at the interfaces between lamellae and matrix. This phenomenon has been coined lamellar magnetism, and *that* was the origin of the unusual magnetization observed today.[2-4] In these layered structures, ilmenite and hematite are magnetically coupled across the interface. This coupling results in the rocks exhibiting a feature known as exchange bias, in which the center of gravity of the magnetic hysteresis loop is shifted with respect to the origin. One of the measured samples from Modum recorded a shift of more than 1 T, the largest recorded exchange bias in a natural mineral.[1, 5] In comparison, the first material to display this property, core-shell particles of Co-CoO, had a shift of 0.16 T.[6]

1.2   From nature to science

The naturally occurring exsolution lamellae in the Modum rocks enforces the idea that new materials with exotic properties can be formed at the interface between well-known compounds. The effect is strongly enhanced in the Modum rocks due to the vast number of lamellae present. However, the idea is not new. Magnetic exchange bias was first shown in 1956 at the interfaces between ferromagnetic cobalt particles and antiferromagnetic cobalt(II) oxide layers.[6] Contrary to pure Co particles, which have a magnetic hysteresis loop symmetrical around origin, the CoO shell results in a material with a shift of the magnetic hysteresis loop along the field axis in the field cooled state.[7, 8] A more detailed explanation is found in chapter 0. Although exchange bias is still usually understood in terms of, and observed at, ferromagnetic/antiferromagnetic interfaces, the phenomenon has been shown in other combinations of ferromagnetic, antiferromagnetic, spin glass, canted antiferromagnetic, cluster glass and distorted magnetic phases.[8-12]

Exchange bias has been exploited in several technological applications since its discovery. It can be used to enhance performance in permanent magnets, or stabilize the magnetization of superparamagnetic particles.[13-17] However, the greatest impact of exchange bias has been in magnetic data storage devices. Based on a design from the 1970's,[18] readback heads of anisotropic magnetoresistance (AMR) hard disk drives used exchange bias to stabilize the ferromagnetic part of the device and reduce Barkhausen noise.[19, 20] Becoming the first commercially available devices to employ exchange bias in 1990, AMR hard drives did not dominate the market of magnetic data storage for long. Another type of magnetoresistance had already been discovered in 1988: giant magnetoresistance (GMR).[21, 22] Introduced in 1997, the readback head in GMR based hard drives consisted of a multilayered stack (Figure 1.1).[23, 24] The stack is built up of a ferromagnetic layer free to switch magnetic direction depending on the bit it hoovers over, a non-magnetic metallic layer to avoid magnetic interference, and a ferromagnetic layer pinned through exchange bias with an antiferromagnetic layer. The pinned ferromagnetic layer serves as a reference to the free layer.
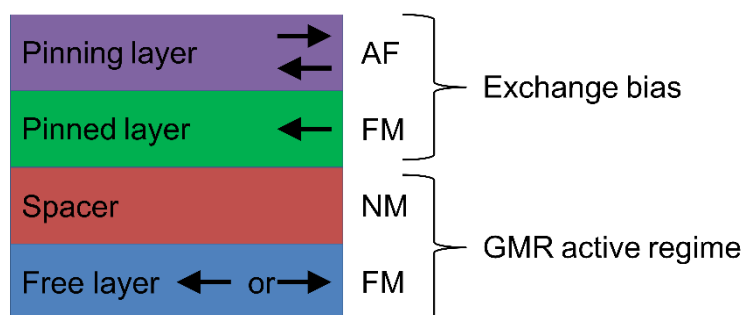

Figure 1.1: Cartoon of a multilayered stack in a giant magnetoresistance (GMR) read head sensor. AF indicates an antiferromagnetic material, FM a ferromagnetic and NM a non-magnetic material. Arrows indicate the direction of the magnetic moments in the different layers.

Essentially acting as a spin valve, the principle of GMR technology utilizes the difference in electrical resistance due to spin dependent scattering of electrons.[25, 26] In a conductor (metal), the number of electrons with spin-up and spin-down is the same at the Fermi level, and thus the electrical resistance is independent of spin. In ferromagnetic materials, however, the density of states at the Fermi level is different for electrons with spin-up and spin-down. When a current is passed through a ferromagnetic material, electrons with the same spin as those responsible for the magnetic moment of the ferromagnet will pass through more easily than electrons with opposite spin. This results in a spin polarization of the electrons. A simple spin polarized valve with two ferromagnetic metals separated by a non-magnetic metal, will serve as an example in the following (Figure 1.2). Incoming electrons are polarized by the first ferromagnetic layer (*Pinned* in Figure 1.2). The spin direction is preserved as the electrons pass through the non-magnetic metal (yellow part of Figure 1.2). Upon entering into the second ferromagnetic layer (*Free* in Figure 1.2), one of two things can occur: In the low resistance state, the magnetic moment of the second ferromagnetic layer (*Free*) is parallel to that in the first layer, and the electrons pass through easily. In the high resistance state, the moments of the two ferromagnets are aligned antiparallel to each other. The polarized electrons will then either "reflect" back or flip its spin in order to find an empty energy state in the new material, both resulting in a higher electrical resistance.
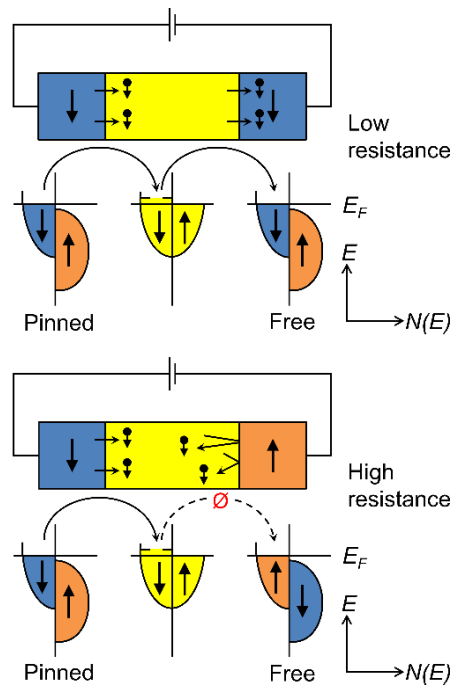

Figure 1.2: Schematic of a spin valve, with spin polarized transport from a ferromagnetic metal (Pinned), through a normal metal (yellow), and into a second ferromagnetic metal (Free). Upper part shows the configuration where magnetic moments are aligned (Low resistance), while the lower part shows the anti-aligned configuration (High resistance). From G. A. Prinz, "Magnetoelectronics," Science, Vol. 282, 1998, pp. 1660-1663. Reprinted with permission from AAAS.

The implementation of GMR technology fueled the exponential increase in areal density of magnetic disk storage devices.[27-31] With the first devices sold in 2004, tunneling magnetoresistive (TMR) heads took over as the leading technology in 2014. The principle of TMR is similar, but fundamentally different, to that of GMR. Replacing the non-magnetic metal in Figure 1.1 with a thin insulating barrier, such as MgO, a magnetic tunneling junction (MTJ) is obtained.[32] With the magnetization of the two ferromagnetic layers in a parallel orientation, it is more likely for electrons to tunnel through the insulating barrier than if the magnetizations are antiparallel.[33-35] MTJ's are also the essential part of magnetoresistive random access memory (MRRAM), anticipated to replace all other memory types as a universal memory device.[36-40]

Considering the above, it becomes evident that the magnetic properties of the Modum rocks make them interesting candidates for use in spin valves. For this reason, in addition to being of interest for geologists, synthetic bulk and mineral samples of ilmenite-hematite have been extensively studied for the last 60 years.[41-47] To elucidate the mechanisms behind these interface dependent properties further, the ability to produce the layers artificially, in a controlled manner, is essential.[48-51] In order to do this, a thin film technique with control of the composition at the atomic level, in addition to a precise thickness control, is required. Thin films of various $(1-x)Fe_2O_3-(x)FeTiO_3$ compositions have indeed already been made, primarily by pulsed laser deposition (PLD),[52-57] but also sputtering.[58] Yet, little or no effort has been made to tailor the lamellar structure observed in mineral samples. Precise control of the stoichiometry in films grown by sputtering is a challenge.[59] While PLD presents a better control of the deposited stoichiometry, it suffers from poor uniformity over larger areas,[59] as well as a risk of particle incorporation.[60] For excellent control of ultra-thin layers, molecular beam epitaxy (MBE) is usually the go-to technique. However, it is quite expensive and there are limitations to the flexibility, in regards of depositing different materials with the same system. In addition, control of the composition of oxides can be an issue.[61]

Disregarding the practical drawbacks of MBE, the technique still enables the thickness of the deposited film to be controlled down to a single layer of atoms. This is obviously an advantage if trying to make layered structures on a nanometer-scale. However, another thin film technique also offers this level of thickness control. Atomic layer deposition (ALD) utilizes surface chemistry to limit the deposition of the film to one monolayer at a time. There are several prerequisites for a process to be successful, but for well-behaving systems, the thickness can be controlled down to sub-monolayers, and compositional control is in theory only limited by the number of precursor sources available. Unlike physical deposition methods, ALD does not depend on line-of-sight, but rather the sterical availability of reactive surface sites for precursor molecules. This ensures conformal growth, even on high aspect ratio surfaces, and is the key to the self-limiting nature of the process. It also

facilitates seamless switching between depositions of different materials, enabling tailor-made layered structures, much like the lamellar structures of the ilmenite-hematite rocks. The current thesis is all about the path towards such lamella by ALD.

While utilizing the advantages of ALD to make exotic interfaces and multilayered structures is nothing new, most of the work has focused on binary oxides. The properties of nanostructures can often be tuned by varying the thickness and number of individual layers. The first report of multilayers by ALD was on HfO_2/Ta_2O_5 as low leakage dielectrics.[62] These nanolaminates could be tuned to improve the charge storage. Another example is Al_2O_3/ZnO multilayers, with tunable optical properties for sensor purposes.[63] These multilayers have also been shown to enable surface topography with a controlled surface roughness.[64] Mechanical properties can be tuned in stacks of Al_2O_3/TiO_2, which can also function as excellent water and gas barriers.[65, 66] With the aid of post-deposition annealing to produce Fe_3O_4, alternating layers of Al_2O_3 and Fe_3O_4 have shown tunable microwave absorption properties.[67] The photoluminescence of Eu_2O_3/TiO_2 stacks have been investigated with control of layer thickness down to one unit cell,[68] while Al_2O_3/Y_2O_3 multilayers have been studied for optical waveguide purposes.[69] With the flexibility ALD provides, changing between depositions of different materials is, as mentioned, easy. This feature has been exploited to make bottom and top electrodes (TiN) during deposition of a ferroelectric material ($Hf_{0.5}Zr_{0.5}O_2$), thus producing a contacted sample ready for testing.[70] This also shows the capability of fabricating complete electrical components for integrated circuits, entirely by ALD.

Exchange bias occurs at interfaces between different types of magnetic materials. Several other type of features have also been demonstrated originating from interfaces. The $LaAlO_3||SrTiO_3$ interface has received massive attention due to the occurrence of exotic properties such as 2D electron gas and superconductivity.[71, 72] Similar to this is the $DyScO_3||SrTiO_3$ interface,[73] while it is predicted that $LaNiO_3||SrTiO_3$ can be used to design oxide-based thermoelectrics. The latter could potentially be realized by ALD, as there are reported processes for both $LaNiO_3$ and $SrTiO_3$.[74, 75] Usually, other thin film techniques are used to make these interfaces, like the already mentioned MBE and PLD. This might be due to the common view that ALD is not appropriate for depositing high quality, single crystal, epitaxial films of complex oxides. However, as Figure 1.3 shows, this is not necessarily the case.
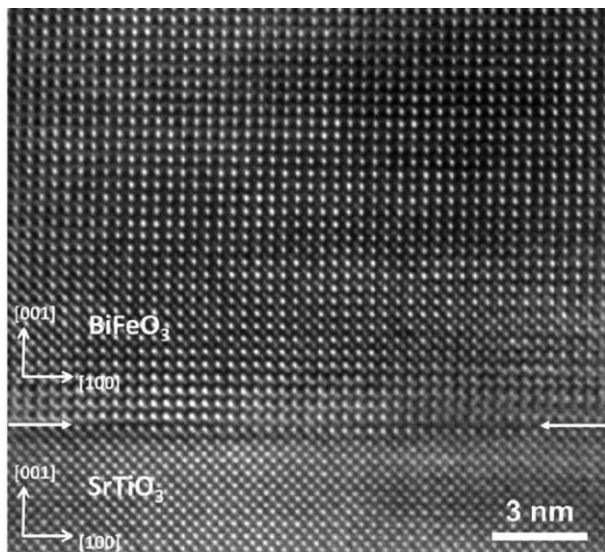
Figure 1.3: High resolution transmission electron microscopy (TEM) image of ALD grown BiFeO$_3$ on a SrTiO$_3$ substrate, post-deposition annealed in air at 700 °C for 3 min. White arrows indicate the interface. Reused with permission from American Chemical Society.[76]

This thesis aims at developing artificial layered structures for design of interface materials with ALD. To recreate the Modum rocks, processes for depositing Fe$_2$O$_3$ and FeTiO$_3$ is necessary. There are several routes for ALD of Fe$_2$O$_3$,[77-83] but given the knowledge within the NAFUMA group where this work has been carried out, a natural choice is the precursor pair Fe(thd)$_3$/O$_3$ (thd = 2,2,6,6-tetramethyl-3,5-heptanedionate).[84, 85] Deposition of FeTiO$_3$, on the other hand, involves chemistry with Fe(II). Reports on direct ALD of oxides with cations in lower oxidation states, like Fe(II), are scarce. Only phases with mixed oxidation states, or phases with mixed oxidation states accompanied by a second phase, are obtained.[82, 83, 86, 87] Producing films of Fe(II) containing oxides typically involves post-deposition reduction from Fe$_2$O$_3$,[88] with the notable exception of direct deposition of Fe$_3$O$_4$, using Fe(2,4-C$_7$H$_{11}$)$_2$ (bis(2,4-dimethylpentadienyl)iron),[83] as well as plasma assisted ALD using Fe(Cp)$_2$/O$_2$.[89] In an attempt to directly deposit Fe(II) containing films, a precursor completely new to ALD was explored, namely: Fe(hfa)$_2$TMEDA, (hfa = 1,1,1,5,5,5-hexafluoro-2,4-pentanedionate, TMEDA = N,N,N',N'-tetramethylethylenediamine). This precursor has previously been used in chemical vapor deposition (CVD).[90-96] Currently, it is used in the first ever process for depositing purely Fe(II) containing films by ALD.

Given the difficulty of acquiring Fe(II) containing films with ALD, a process for depositing NiTiO$_3$ was developed. The idea was thereby to replace FeTiO$_3$ and create a model system to mimic the layers in the Modum rocks. There is a range of alternatives for depositing TiO$_2$ with ALD,[97] but the most used are TiCl$_4$/H$_2$O and Ti(O^{i}Pr)$_4$/H$_2$O. The latter was chosen in this work, due to the low remains of residue in the obtained films. There are also a range of processes studied for ALD of NiO.[98] The precursor pair Ni(acac)$_2$/O$_3$ was selected, as other processes present narrow or no proper ALD window. Since

this system is not well examined, a proper study of the growth of NiO was done first, prior to the combination with TiO_2. The combination gave a robust process for deposition of $NiTiO_3$, and the study was further expanded to investigate the effects of different substrates on the crystal structure and orientation of the obtained films. When combined with deposition of Fe_2O_3, multilayered structures of $Fe_2O_3/NiTiO_3$ was obtained and their magnetic properties are discussed in chapter 5.2.2.

2 Background and theory

This chapter presents an introduction to magnetism and magnetic materials, as well as crystal structures and their magnetic properties relevant to the work in this thesis. Finally, some selected magnetic phenomena are discussed.

2.1 Magnetism

We are all constantly surrounded by the earth's magnetic field, and have an impression of the electromagnetic force through encounters with what we refer to simply as "magnets". Still, to comprehend the origins of magnetism, and exactly why some materials are "magnetic" and others not, can be quite complicated. While most macroscopic observations are explained by classical physics and electromagnetism, the *atomic* origin of magnetism was first understood in the early 1900's, with the development of quantum mechanics. This makes the work of André-Marie Ampère in the 1820's especially impressing. Earlier, Hans Christian Ørsted had discovered that a magnetic needle is deflected by a nearby electric current, and that electric currents generate magnetic fields. By developing a mathematical and physical theory regarding these phenomena, Ampère proved the intimate relationship between electricity and magnetism. After experimenting with current loops, he realized that currents circulating counter-clockwise correspond to the north pole of a bar magnet, and conversely, clockwise circulating currents correspond to the south pole. This led him to the surprisingly accurate hypothesis, given the level of knowledge at the time, that current loops are responsible for all magnetic effects, and that magnetic effects in a material are due to "molecular currents" within the material. Today, we know that there are two kinds of contributions to a system's magnetic moment: the motion of electric charges, and the intrinsic magnetism of elementary particles. To understand magnetism and magnetic properties on a macroscopic scale, an understanding of atomic magnetism is needed.

So, what makes an atom magnetic? In short: the motion and properties of its elementary particles, namely its electrons and protons. Although the nucleus contributes to the magnetic moment of an atom, the magnitude of the contribution is much smaller than that of electrons. Techniques measuring nuclear magnetism, e.g. nuclear magnetic resonance (NMR) and Mössbauer spectroscopy can be important tools to get a full understanding of a material. However, to explain the atomic origins of magnetism and the different kinds of magnetic materials relevant to the work in this thesis, it is sufficient to consider only the contribution from electrons.

Due to their electric charge, electrons behave like circulating currents when orbiting a nucleus, corresponding to Ampère's current loops. But in addition,

electrons also possess a magnetic moment because of their spin: an intrinsic quantum mechanical property. Electrons and atoms are quantum systems, and can only be described by quantum mechanics. Unlike classical mechanics, where values range continuously, quantum mechanics describe the energy, spatial distribution and properties of a quantum system through a set of discrete quantum numbers. The magnetic properties of electrons are determined by the orbital angular momentum quantum number (or azimuthal quantum number), l, and the spin quantum number, s. Corresponding to the atomic orbitals, l is a non-negative integer (0, 1, 2, 3 etc.), while for electrons (and all other fermions), s is always ½. Whenever a reference system is defined, e.g. by the direction of an applied magnetic field, the angular momentum and spin is assigned an orientation in relation to the reference system. Two additional quantum numbers describe this orientation: the magnetic quantum number, m_l, refers to the direction of the angular momentum and can take integer values from $-l$ to $+l$. The spin analog is the secondary spin quantum number, m_s, ranging from $-s$ to $+s$ in steps of one. For an electron, m_s can be $+½$ or $-½$, corresponding to spin-up and spin-down, respectively.

Considering an individual electron, the magnitude of the orbital angular momentum, $|\mathbf{L}|$, and the spin angular momentum, $|\mathbf{S}|$, is given by:

$$|\mathbf{L}| = \hbar\sqrt{l(l+1)} \qquad\qquad \textbf{(2.1)}$$

$$|\mathbf{S}| = \hbar\sqrt{s(s+1)} \qquad\qquad \textbf{(2.2)}$$

where $\hbar$ is the Planck constant, h, divided by 2π ($\hbar = h/2\pi$), called the reduced Planck constant or Dirac constant.

One could imagine that adding together the individual orbital and spin contributions from each electron in an atom would yield a total magnetic moment for that atom. However, it is not that straightforward. The spin and orbital contributions interact, both for individual electrons and between different electrons. All these interactions are called: spin-spin, spin-orbit and orbit-orbit couplings. Their relative magnitudes are different throughout the periodic table, which both simplifies and complicates the calculation of the total magnetic moment of an atom.

For lighter elements (atomic number ≤ 30), the spin-orbit coupling is much weaker than the other two, and can be ignored. A good approximation is therefore first to combine all the orbital angular momenta for individual electrons to get a many-electron orbital angular momentum (L), and then do the same for the individual spin angular momenta to get a many-electron spin momentum (S). This is called Russel-Saunders coupling, or LS-coupling. Combining L and S by vector addition results in the total angular momentum quantum number, J. The exact calculations of L, S and J are tedious and serves no purpose here. Instead, it is noted that the magnitude of total angular

momentum for an individual atom with negligible spin-orbit coupling can be calculated from:

$$|\boldsymbol{J}| = \hbar\sqrt{J(J+J)}$$ (2.3)

For heavier atoms, the spin-orbit coupling is much stronger, and must be taken into account. A good approximation here is to employ jj-coupling. To do this, corresponding spin and orbital angular momenta of each electron, i, are combined to form individual total angular momenta, j_i ($j_i = l_i + s_i$). These individual momenta then couple to form a total angular momentum:

$$J = \sum_i j_i$$ (2.4)

With J obtained, from either Russel-Saunders or jj-coupling, the total magnetic moment of an atom can be calculated:

$$\mathbf{m}_{\mathrm{atom}} = g_j \mu_{\mathrm{B}} \sqrt{J(J+1)}$$ (2.5)

where μ_{B} is the Bohr magneton[a] and g_j is the Landé g-factor, given by:

$$g_j = 1 + \frac{J(J+1) + S(S+1) - L(L+1)}{2J(J+1)}$$ (2.6)

While L and S can be found through Russel-Saunders coupling, they are not specified for jj-coupling. However, an important observation should be pointed out: for a completely filled orbital (shell) of electrons, the values of L, S and J are all zero. Consequently, there is no net magnetic moment, and atoms with only completely filled orbitals are called diamagnetic. This also means that for all other atoms it is sufficient to only consider the incomplete orbitals, or the number of unpaired electrons, when calculating L, S and J.

Equation (2.5) works especially well for salts of lanthanide ions. However, for some elements, the magnetic moment can be estimated in another way. For the transition elements, particularly the 3d elements, a curious feature called "orbital quenching" occurs. The result of this is that the magnetic moment is determined almost entirely by the spin contribution. Equation

---

[a] The Bohr magneton, μ_{B}, is a physical constant representing the magnetic moment of an electron caused by either its spin or orbital angular momentum. An individual electron moving with angular momentum $\hbar$ has a magnetic moment approximately equal to 1 μ_{B}. The value of a Bohr magneton for an electron is defined as: $\mu_{\mathrm{B}} = e\hbar/2m_e c$ = $9.274 \cdot 10^{-24}$ J/T, where e is the elementary charge, m_e is the mass of an electron and c is the speed of light. In quantum physics, it is practical to express the magnetic moment of an atom in terms of μ_{B}.

(2.6) is simplified (g_j becomes approximately 2), and equation (2.5) can be rewritten by replacing J with S:

$$\mathbf{m}_{\text{atom}} = g_j \mu_\text{B} \sqrt{S(S+1)} \qquad\qquad \textbf{(2.7)}$$

Further, when there are n unpaired electrons on each ion, each of which have s equal to ½, the total spin quantum number, S, becomes $n/2$: $S = s_1 + s_2 + s_3 \dots s_n =$ ½ + ½ + ½ + $\cdots$ = $n/2$. Remembering that we only need to consider the number of unpaired electrons, n, to calculate the magnetic moment, we finally arrive at the spin-only formula:

$$\mathbf{m}_{\text{atom}} = \mu_\text{B} \sqrt{n(n+2)} \qquad\qquad \textbf{(2.8)}$$

Even with the approximations above, remarkably accurate values for the magnetic moments of 3d elements are obtained. For example, equation (2.8) gives a value of 5.92 μ_B for the magnetic moment of Fe^{3+} with an octahedral high-spin d^5 configuration, while the measured values are 5.7–6.1 μ_B.

So far, we have considered contributions to an atom's magnetic moment from its electrons spin and orbital angular momenta. However, to understand the difference between different kinds of magnetic *materials* we will look at how they respond to a magnetic field.

The change in orbital motion of electrons when exposed to an external magnetic field is called the diamagnetic effect. It occurs in all atoms and materials, but the phenomenon is so weak (compared to other phenomena) that only atoms and materials with no net magnetic moment (J = 0) are classified as diamagnetic. A diamagnetic material will be deflected by an external magnetic field. The reason for this is that the field induces currents in the material, opposing the field. These currents induce a magnetic field in the opposite direction of the external field (according to Lenz's law), and diamagnetic materials are thus repelled from the applied magnetic field. The diamagnetic effect is larger in a stronger field, however, the effect is still small, and diamagnets are considered non-magnetic by laypeople.

Magnetic measurements are not performed on isolated atoms. It is therefore convenient to consider the magnetization of a material as a whole. This magnetization, $\mathbf{M}$, is defined as the magnetic moment per unit volume. Further, magnetic materials are categorized according to how their magnetic dipole moments (or absence of moments, as in diamagnets) are arranged, and how they respond to an applied field. This response to, or variation in magnetization with, an applied field is called magnetic susceptibility, χ (sometimes denoted χ_v to distinguish it from mass and molar susceptibilities).

Diamagnetic materials have a small, negative magnetic susceptibility, linearly increasing in magnitude with increasing field strength. The magnetic

susceptibility is given by the ratio between magnetization (**M**) and the applied field (**H**):

$$\chi = \frac{\mathbf{M}}{\mathbf{H}} \qquad (2.9)$$

As both **M** and **H** are measured in A/m, χ is a dimensionless quantity. Diamagnets have a small, negative susceptibility, independent of temperature.

Atoms with unpaired electrons (and $J \neq 0$) are called paramagnetic. Paramagnetic materials consist of paramagnetic atoms, with no collective ordering of the dipole moments. In the absence of a magnetic field, the directions of the magnetic dipole moments in paramagnets are randomly oriented in space, and the net magnetic moment is therefore zero. However, in the presence of a small magnetic field, the moments will start to align along the field direction, and the material is therefore (weakly) attracted by the magnetic field. This process increases as the strength of the applied field increases, but if the field is removed, the moments go back to a random orientation. Hence, starting at zero, the magnetic susceptibility of a paramagnetic material is positive and linearly increasing with increasing field strength. Unlike diamagnets, the susceptibility of paramagnets is also affected by temperature. For a paramagnetic material in a given field, χ is inversely proportional to the temperature, T, by a factor called the Curie constant, C. This is known as Curie's law:

$$\chi = \frac{\mathbf{M}}{\mathbf{H}} = \frac{N\mu_0 m_{\text{atom}}^2}{3k_{\text{B}}} \cdot \frac{1}{T} = \frac{C}{T} \qquad (2.10)$$

where N is the number of magnetic dipole moments per unit volume, μ_0 is the permeability of free space ($4\pi \cdot 10^{-7}$ H/m), k_{B} is the Boltzmann constant ($1.380\,648 \cdot 10^{-23}$ J/K) and m_{atom} is given by equation (2.5) or (2.8). Note that χ is still dimensionless. To sum up: for a given temperature, the susceptibility of a paramagnet is positive and increases with increasing field strength. For a given field strength, the susceptibility is still positive, but decreasing with increasing temperature.

As with the diamagnetic effect, the paramagnetic response is rather weak. However, among the materials with unpaired electrons, a handful have all their magnetic moments aligned parallel to each other, even in the absence of an external magnetic field. Materials with this property are called ferromagnetic. Their permanent collective ordering of magnetic moments is explained not only by the magnetic properties of the electrons, but also by the electrons interactions with each other. A comprehensive explanation of ferromagnetism involves complicated quantum mechanics and band theory,

which is beyond the scope of this text. A conceptual introduction is given instead.

Quantum mechanics is governed by energy, and quantum mechanical systems wants to have the lowest possible total energy. This is reflected in the electronic configuration of atoms: how the electrons are placed in atomic orbitals surrounding the nucleus. In general, orbitals closer to the nucleus are lower in energy, and are filled up first. Each orbital can accommodate two electrons, but *only* if they have opposite spins (values of m_s). This is known as the Pauli exclusion principle, which is valid for molecular orbitals, or bonding orbitals, as well. In a covalent bond, atoms share electrons in bonding orbitals. Each orbital has one electron with spin-up ($m_s = +\frac{1}{2}$) and one with spin-down ($m_s = -\frac{1}{2}$). The bonding energy arising from the formation of chemical bonds lowers the energy of a system. However, when two electrons occupy the same orbital, they are also closer in space. Since electrons have the same electric charge, this means that bringing them closer together results in a higher Coulomb repulsion. If the spins are parallel, they cannot occupy the same orbital, and are thus farther apart. The energy decrease due to the lower Coulomb repulsion is known as exchange energy. In general, a lower energy is obtained through bonding than from exchange energy. The opposite is true for only four elements in the periodic table. Iron (Fe), cobalt (Co), nickel (Ni) and gadolinium (Gd) are ferromagnetic at room temperature (there are also several compounds that are ferromagnetic at room temperature). These elements have unpaired electrons, all with parallel spins. A consequence of exchange energy dominating over bonding energy is that there is weak bonding interactions between the electrons responsible for the ferromagnetic property. Although covalent bonds are not the primary bonding scheme in these materials, the idea of covalent bonds gives an intuitive explanation for exchange energy.

Even though a configuration with parallel spins is energetically favorable for ferromagnetic materials, there is always an upper temperature limit, called the Curie temperature (T_C). Above this critical temperature, the thermal energy overcomes the ferromagnetic ordering, and the spontaneous magnetization is lost. The material then behaves like a paramagnet, and the susceptibility of ferromagnetic materials well above T_C is described by the Curie-Weiss law, a modification of the Curie law:

$$\chi = \frac{C}{T - T_C} \tag{2.11}$$

It should be noted that the Curie-Weiss law does not hold for temperatures close to the Curie temperature. T_C in equation (2.11) is actually slightly larger than the observed Curie temperature, and is sometimes denoted θ (the Weiss constant) to distinguish it from the real Curie temperature. Due to the diminishing thermal energy, the susceptibility increases rapidly with

decreasing temperature below the Curie temperature, before reaching a maximum value.

The statement that all magnetic moments in a ferromagnetic material are aligned parallel is not entirely correct. In short, the material wants to lower its total energy, composed of the exchange, magnetostatic, magnetocrystalline and magnetostrictive energies. A full description of the mechanisms behind this is beyond the purpose of the explanation presented here, so attention is focused on the magnetostatic energy.

A ferromagnet with all its moments aligned in one direction will set up a magnetic field extending into the space outside of the material. This requires a lot of magnetostatic energy. To lower this energy term, it forms magnetic domains, smaller regions within which the magnetic moments are aligned parallel to each other. By having these domains pointing in all directions, the portion of the magnetic field extending outside of the material is minimized, thus minimizing the magnetostatic energy. The actual ordering of the domains is more complicated than a simple random orientation, but this serves as a starting point to understand a characteristic feature exhibited by ferromagnetic materials in response to an applied magnetic field: the magnetic hysteresis loop (Figure 2.1).
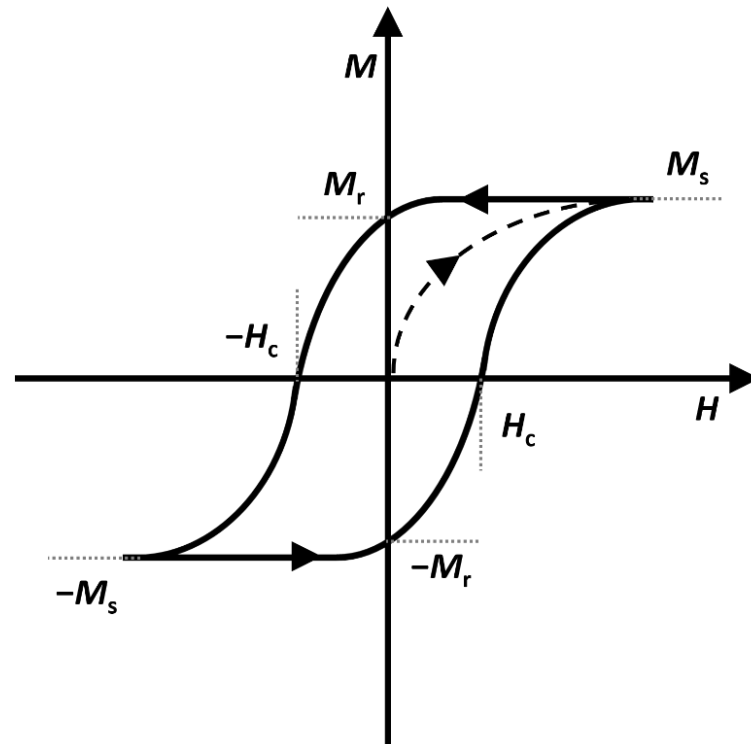

Figure 2.1: Idealized hysteresis curve for a ferro- or ferrimagnetic material, showing the magnetization of the material (M) as a function of applied field (H). The saturation magnetization (M_s), remanence (M_r) and coercivity (H_c) are indicated in both field directions.

If the individual magnetic domains in a ferromagnet are completely randomly oriented, and of equal size, the material has no net magnetization (the net moments of the different domains cancel each other). When subjected to an increasing magnetic field, the domains that have moments parallel to the applied field start to expand at the expense of domains in other directions. This results in an increased magnetization of the material (dashed line in Figure 2.1), up to a point where the magnetic domains aligned along the field direction cannot grow anymore. At this point and the material has reached saturation magnetization, M_s. Decreasing the field back to zero does not demagnetize the material, but instead leaves it with a remanent magnetization or remanence, M_r. A field in the opposite direction of the first, a negative field $(-H_c)$, is required to reduce the magnetization of the material to zero. [b] If the negative field is increased even more, the material will eventually saturate again, but this time in the opposite direction $(-M_s)$. Analogous to the positive field first applied, reducing the negative field to zero again leaves a remanent magnetization, but in the opposite direction of the first $(-M_r)$. A complete hysteresis curve, or loop, is then obtained if a positive field through H_c and up to M_s is applied. Note that the hysteresis loop is symmetrical around origin.

There are two additional types of magnetism with collective ordering of moments. Both antiferromagnetism and ferrimagnetism are similar to ferromagnetism in the way that the magnetic moments are ordered in space. The difference in the case of antiferromagnetism is that half of the moments are ordered antiparallel to the other half. This results in a material with no net magnetic moment, as all the moments cancel each other out. The temperature below which this spontaneous ordering occurs is called the Néel temperature (T_N). Above T_N, the material becomes paramagnetic and obeys the Curie-Weiss law, but with $+\theta$ replacing $-T_C$ in equation (2.11) (negative θ). The moments in antiferromagnetic materials can all be aligned parallel, but that requires very high fields.

Just like in antiferromagnetic materials, the magnetic moments in ferrimagnetic materials are aligned antiparallel. However, in a ferrimagnet the magnitude of the moments aligned in one direction is not exactly the same as the ones aligned antiparallel, resulting in a net magnetic moment. As with ferromagnetic materials, ferrimagnets also exhibit magnetic hysteresis and have a Curie temperature (T_C), above which they are paramagnetic.

---

[b] The size of H_c is called coercivity. Ferromagnetically hard materials have a large magnetocrystalline anisotropy, and a large field (more energy) is required to change the direction of the magnetic moments. A hard ferromagnet has large coercivity and require a large field to reach saturation (M_s). Conversely, the direction of the magnetic moments in a soft ferromagnet can be changed more easily, resulting in a steeper M(H) curves (but not necessarily a larger M_s) and smaller coercivity.

2.2   Hematite and ilmenite

With the quick introduction to the origins of magnetism and different classes of magnetic materials above, it is time to look at some specific materials relevant to this thesis.

2.2.1   Crystal structure

Hematite (Fe_2O_3) and ilmenite ($FeTiO_3$) are closely related structurally. With only one type of cation, Fe_2O_3 adopts the $R-3c$ space group, known as the corundum type structure. Each Fe^{3+} is surrounded by six O^{2-}, in an octahedral geometry. Pairs of face-sharing octahedra lie along the c axis, with a "missing" octahedron separating each pair (Figure 2.2, left).
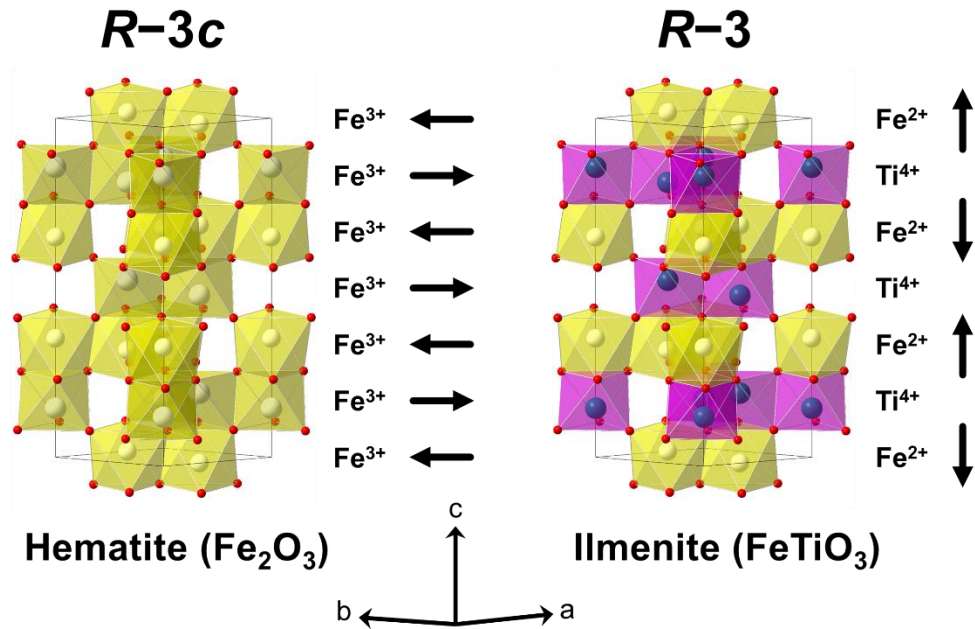
Figure 2.2: The crystal structures of Fe_2O_3 (left) and $FeTiO_3$ (right).

The crystal structure of $FeTiO_3$ is closely related to the corundum structure. However, the inclusion of a second cationic element spices up the symmetry possibilities, without major changes to the position of the atoms in the lattice. At elevated temperatures, diffraction data suggest a random distribution of Fe^{2+} and Ti^{4+} and the crystal structure is then regarded as "disordered". As any cation position can be occupied by either element in the high temperature form, the symmetry is identical to Fe_2O_3, and the space group is $R-3c$. At lower temperatures, the different cationic elements "order" into alternating layers perpendicular to the c axis (Figure 2.2, right). One Fe^{2+} and one Ti^{4+} then occupy each pair of octahedra. With this ordered layering, the c-glide plane is lost; $FeTiO_3$ adopts the $R-3$ space group, and the crystal structure to which ilmenite lends its name.

2.2.2   Magnetic structure

Both hematite and ilmenite are antiferromagnetic materials, and their magnetic structures are shown in Figure 2.3. Below the Néel temperature (T_N ~950 K),[41, 99] the magnetic moments in Fe_2O_3 align perpendicular to the c axis, with ferromagnetic ordering within each Fe^{3+} layer (Figure 2.3 i). Alternating layers are antiparallel, cancelling each other along the c axis. However, the moments are not perfectly antiparallel. There is a slight rotation of the moments in each layer within the (001) plane. Alternating layers have the same angle of rotation, but in opposite direction from the previous one. Thus, a very weak net magnetic moment in the ab plane (basal plane), perpendicular to the c axis, is present in Fe_2O_3. This tilting of moments is called canted antiferromagnetism (CAF), and Fe_2O_3 is actually a weak ferrimagnet.
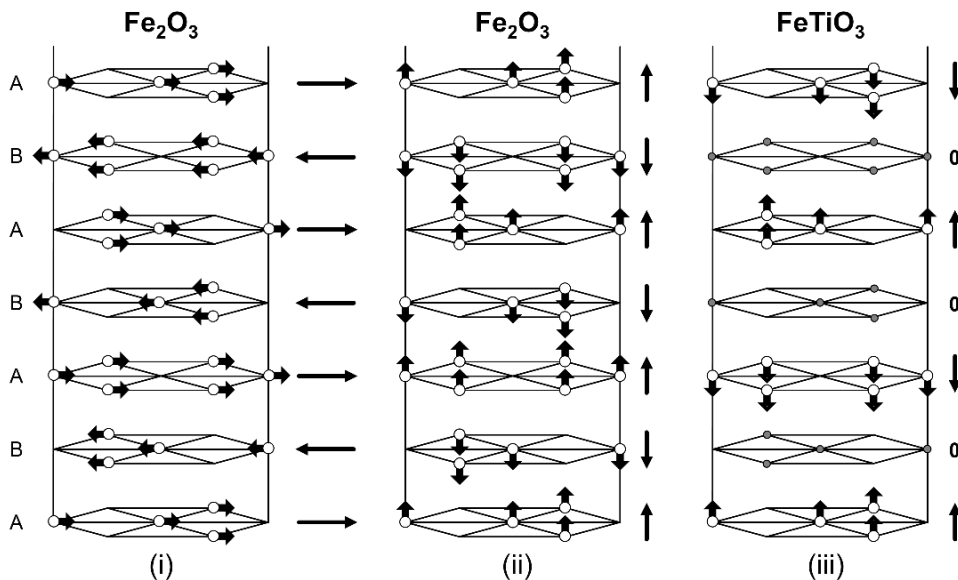
Figure 2.3: The magnetic structures below T_N (950 K) of Fe_2O_3 above (i) and below (ii) the Morin transition (260 K), as well as the magnetic structure (half the magnetic unit cell) of $FeTiO_3$ (iii) below T_N (55 K). The direction of net magnetic moments within each layer is indicated to the right of each structure. Oxygen atoms are omitted for clarity. A and B layers lie along the crystallographic c axis.

At 260 K,[41, 100, 101] the so-called Morin transition occurs: the magnetic moments flip, now pointing *along* the c axis (Figure 2.3 ii), still with ferromagnetic ordering within the layers and each layer with an antiparallel coupling to the next. The moments are no longer tilted, and the net magnetic moment is zero.

$FeTiO_3$ has a Néel temperature of 55 K,[41] below which the moments of the Fe^{2+} layers align along the c axis (Figure 2.3 iii), a configuration analogous to the ordering in Fe_2O_3 below the Morin transition. The antiparallel ordering transcends the non-magnetic Ti^{4+} layers, and there is no net magnetic moment.

2.3 Selected compounds related to Fe_2O_3 and $FeTiO_3$

There are several compounds magnetically related to Fe_2O_3 and $FeTiO_3$. The magnetic structures for a selection of them are depicted in Figure 2.4. Below the Néel temperatures, magnetic moments in $NiTiO_3$ (23–26 K)[102, 103] and $CoTiO_3$ (37 K)[103] order ferromagnetically within each layer of Ni^{2+}/Co^{2+}, with non-magnetic layers of Ti^{4+} separating the antiferromagnetic coupling along the c axis, similar to $FeTiO_3$ (Figure 2.4 i). Contrary to $FeTiO_3$, the moments are directed perpendicular to the c axis. As for $FeTiO_3$, the magnetic moments in $MnTiO_3$ below T_N (41 K)[104, 105] are aligned parallel to the c axis (Figure 2.4 ii). However, an important difference with respect to $FeTiO_3$ is that the moments have an antiparallel coupling within every layer, thereby cancelling each other. Hence, $MnTiO_3$ does not have ferromagnetic coupling within the layered structure, in contrast to the other antiferromagnetic compounds visited so far.
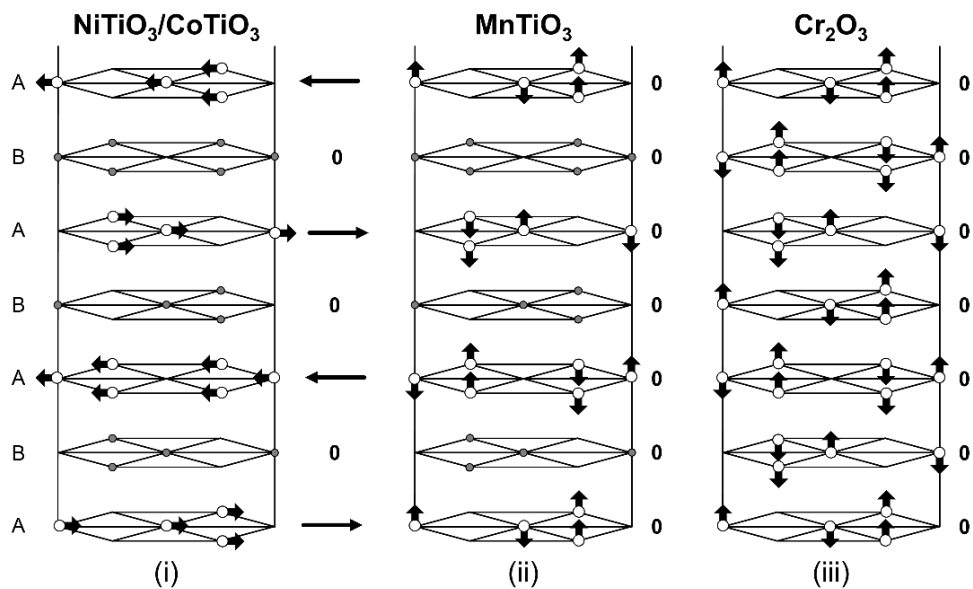

Figure 2.4: The magnetic structures (half the magnetic unit cell) of selected $ABO3$ compounds and Cr_2O_3, below T_N, with A and B layers along the crystallographic c axis. The direction, or absence, of net magnetic moments within each cation layer is indicated to the right of each structure. Oxygen atoms are omitted for clarity.

Interestingly, the difference between $FeTiO_3$ and $MnTiO_3$ is analogous to that of Fe_2O_3 and Cr_2O_3. Like Fe_2O_3 (below the Morin transition), the magnetic moments in Cr_2O_3 order parallel to the c axis below the Néel temperature (307 K) (Figure 2.4 iii).[99, 106] However, similar to $MnTiO_3$, there is no ferromagnetic coupling, as the magnetic moments are antiferromagnetically coupled within every layer.

2.4 Lamellar magnetism and exchange bias

As previously mentioned, the fact that rock samples of hematite-ilmenite composites have a net magnetic moment at all is counter-intuitive when considering the constituents individually. To explain the observed magnetic nature the concept of "lamellar magnetism" has been introduced.[3, 107-109] Exsolution lamellae of ilmenite in a hematite "host", or vice versa, are abundant in these aggregates, with sizes ranging from micrometers to nanometers. For simplicity, only ilmenite lamellae in a hematite host will be considered. As oxygen does not contribute to the magnetization, it is sufficient to look at the cation layers, which lie in planes along the crystallographic c axis (Figure 2.3). It turns out that the number of cation layers and position of the lamellae in the host is what governs the macroscopic magnetic properties. Monte Carlo simulations have shown that it is favorable to form "contact layers" at the interface between host and lamella.[3, 107] These contact layers consist of equal parts Fe^{2+} and Fe^{3+}, and improve the local Pauli bond-strength satisfaction of oxygen in layers parallel to (001), but they are also decisive for the total magnetization according to the lamellar magnetism theory.[109] An idealized cartoon of two different placements of nanoscopic ilmenite inclusions in a hematite host is depicted in Figure 2.5.

Ilmenite Ti^{4+} layer
Ilmenite Fe^{2+} layer
Hematite Fe^{3+} layer
Contact Fe^{2+}/Fe^{3+} layer
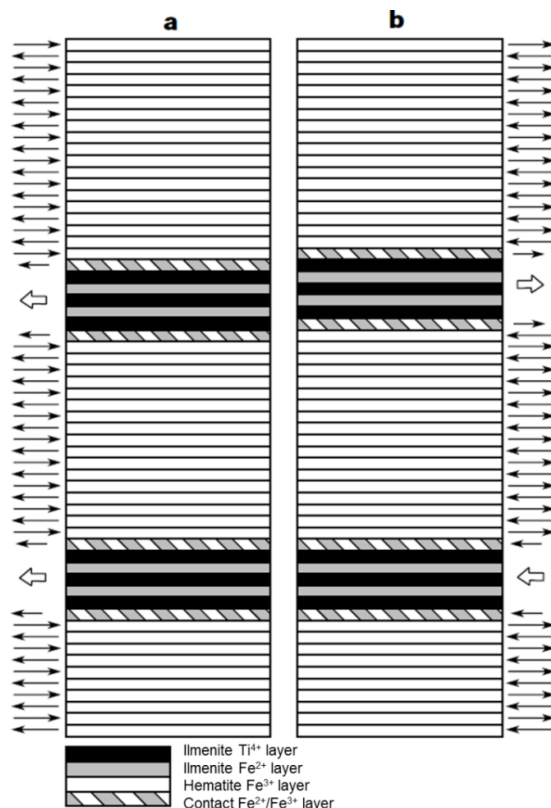
Figure 2.5: Cation layer models showing possible placements of two ilmenite lamellae in a hematite host. An odd number of host layers separating the lamellae yields a net magnetic moment (a). With an even number of host layers, the lamellae moments cancel each other (b). Reused with permission from Nature Publishing Group.[3]

The insertion of a lamella removes an odd number of cation layers from the host. This leads to the moments of the two contact layers for that lamella to be aligned parallel to each other, antiferromagnetically coupled to the hematite. With the insertion of a second lamella, two situations can occur: if the number of cation layers between the lamellae is odd, the moments of the contact layers are in phase with each other, pointing in the same direction (Figure 2.5 a). An uncompensated moment is left in the host, since an odd number of layers were replaced by the lamella. If there is an even number of cation layers between the lamellae, the moments of the contact layers cancel each other (Figure 2.5 b). In this case, the moments of the hematite host also cancel each other, leaving the whole system with no net moment.

The net moment of a lamella can easily be calculated. One contact layer consists of equal parts of Fe^{2+} and Fe^{3+}, and there are two contact layers per lamella. Subtracting the oppositely pointing Fe^{3+} layer (from the hematite host) leaves a net moment per lamella of:

$$M_{\text{lamella}} = 2(0.5M_{Fe^{2+}} + 0.5M_{Fe^{3+}}) - M_{Fe^{3+}} = M_{Fe^{2+}} \qquad \textbf{(2.12)}$$

These lamellar systems can be regarded as giving rise to a type of ferrimagnetic material. Given a correct placement and number of layers in the lamellae, it is intuitive that maximizing the number of lamellae will maximize the total net magnetic moment of a sample. Indeed, transmission electron microscopy (TEM) of hematite-ilmenite rock samples with a large remanent magnetization has shown an abundance of nanoscale exsolution of lamellae (Figure 2.6).[1]
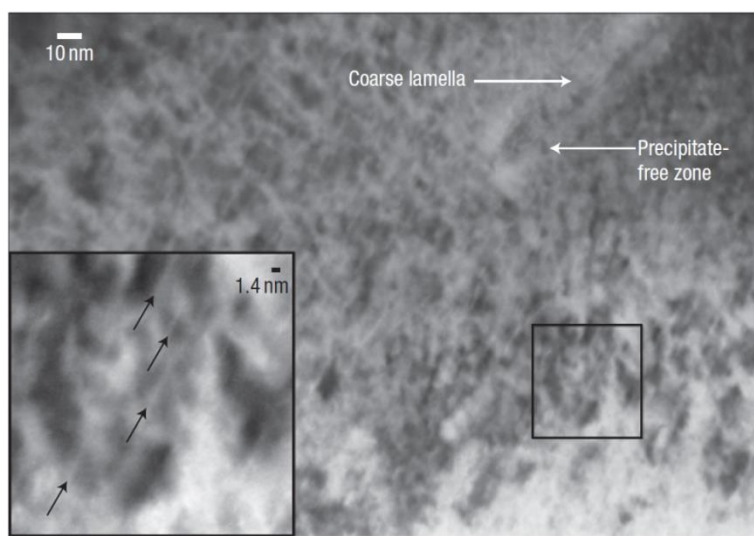

Figure 2.6: TEM of ~1 nm thick ilmenite lamellae (black arrows in inset) in a hematite host. Reused with permission from Nature Publishing Group.[1]

The strong antiferromagnetic coupling between the contact layer and the first cation layer in the host results in a magnetically hard material, and the high T_N of hematite makes the system stable with regards to temperature. But the coupling also gives rise to a rather exotic magnetic property: exchange bias. As mentioned, the hysteresis loop of a ferromagnetic material is symmetrical around origin. Exchange bias shifts the hysteresis loop, either vertically or horizontally. This phenomenon was first observed in a bilayered material consisting of cobalt, a ferromagnet, and cobalt(II) oxide, an antiferromagnet.[6, 7]

A complete understanding of the mechanisms behind exchange bias has been elusive. In the following, an imagined interface between a soft ferromagnetic and a hard antiferromagnetic layer will serve as qualitative example. In the presence of a magnetic field, the bilayer is cooled from a temperature below T_C, but above T_N (where the antiferromagnetic layer is actually paramagnetic). Upon cooling through T_N, the direction of the ferromagnetic layer dictates the direction of the first layer of magnetic moments in the antiferromagnetic layer. [c] This, in turn, decides the direction of the alternating moments throughout the rest of the antiferromagnet. Figure 2.7 illustrates the effect of applying a magnetic field to this system, once the exchange coupling is established.

As with a simple ferromagnet, not all the domains within the ferromagnetic layer are perfectly aligned. Applying a magnetic field will align the domains, and the system eventually reaches magnetic saturation (Figure 2.7 i), as if only the ferromagnetic layer is present.[d] However, when the field is reversed, the system appears "harder" than if the antiferromagnetic layer was absent: a larger negative field is needed to change the direction of the ferromagnetic moments (Figure 2.7 ii). This is because the hard antiferromagnetic layer exerts a force on the moments in the ferromagnetic layer, competing with the applied field, to retain the original direction of magnetization. Eventually, a large enough (negative) field will flip the moments in the ferromagnetic layer (Figure 2.7 iii), and saturate the system. When the applied field is reduced, the force from the antiferromagnetic layer will aid the reversal of the moments in the ferromagnetic layer (Figure 2.7 iv). The center of mass of the resulting hysteresis loop is shifted away from origin by H_E (in size, sometimes referred to simply as "exchange bias" or "biasing field"), as opposed to what would have been the case with only the ferromagnetic layer present.

---

[c] The first layer of moments in the antiferromagnet can be aligned parallel, antiparallel or so-called non-collinear to the magnetic direction of the ferromagnetic layer.[110] However, the theory behind the different constellations is beyond the purpose of this text, and a parallel alignment will be assumed in the following.

[d] As mentioned, the moments in an antiferromagnetic material can also be to reorient and order ferromagnetically, but that usually (depending on the hardness of the material) requires a much larger field.
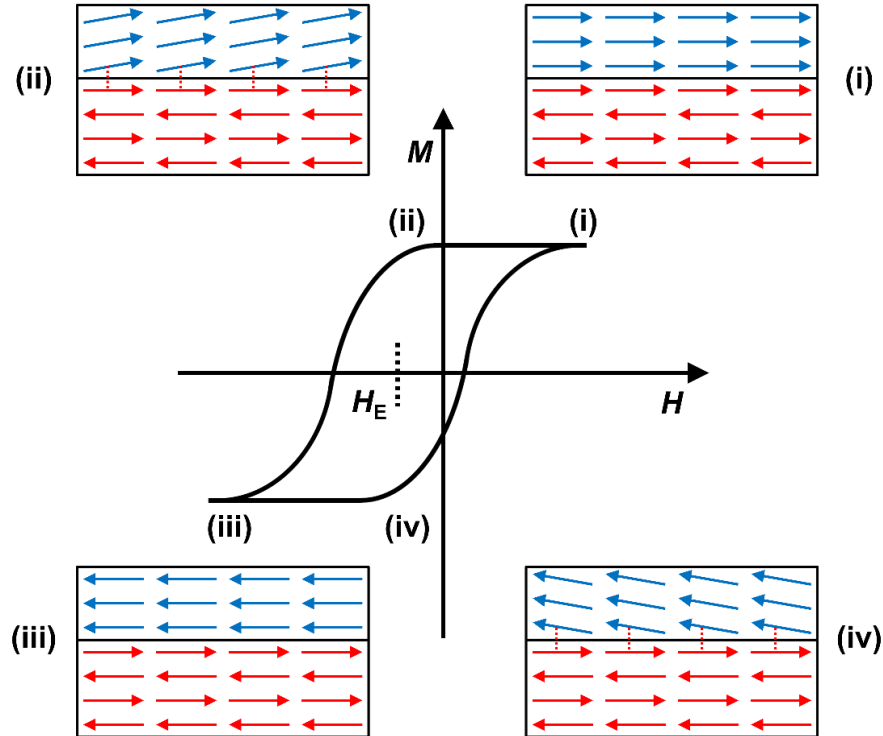
Figure 2.7: The effect of an applied field on an exchange bias coupled bilayer consisting of a ferromagnet (black arrows) and an antiferromagnet (grey arrows). The arrows represent magnetic dipole moments, while H_E denotes the exchange bias field exerted by the antiferromagnetic layer.

The example presented here gives an intuitive understanding of how the hysteresis loop can be shifted in an exchange bias coupled system. Other effects are also observed, like the training effect and the minor loop effect. The loop can also be shifted in other directions, or in the case of one constituent having a low anisotropy: not be present at all. The details of these effects will not be explored here. However, it is reminded that not all systems are comprised of a ferromagnet and an antiferromagnet. In the hematite-ilmenite system, both constituents are antiferromagnetic, and the ilmenite is the magnetically hard material, with a high anisotropy. The coupling mechanism is more complex than in the example above,[48-51] and the hysteresis loop is shifted both horizontally and vertically, with recorded values up to 1 T.[1] This is an order of magnitude larger than for most systems, e.g. the first report of exchange bias by Meiklejohn and Bean in 1957.[7] However, more recently shifts of up to 4 T have been observed in $DyCo_4$ films.[111]

It is intriguing that such remarkable materials are discovered in nature, and it would be even more rewarding to be able to design and build such structures artificially in the laboratory. The latter will be the focus of the following parts of this thesis, but first we will look at the technique that is probably best suited to realize the required nanostructured manufacturing of materials that may provide lamellar magnetism.

3 Atomic Layer Deposition

While certainly not a new technique, atomic layer deposition (ALD) deserves special attention, as it is a crucial part of this thesis.

3.1 Basic principle

Atomic layer deposition (ALD) is a technique using sequenced and separated pulses of precursors to grow thin solid films. Unlike other chemical thin film deposition methods, the only reactions occurring in ALD are between the gaseous precursor and reactive sites on the surface. As an illustrative example of binary oxide deposition, ALD of Al_2O_3 from trimethyl aluminium (TMA) and water in a continuous gas flow reactor is depicted in Figure 3.1. The process consists of two stages. The first half-cycle (A) represents the cation part of the process, and the other half-cycle contributes the oxygen (B). Starting with a surface saturated with OH-groups (A_0), TMA is introduced to the reaction chamber and chemisorbed through reactions with the OH-groups (A_1). After all available sites have reacted (A_2), excess precursor and by-products (CH_3) are purged from the reaction chamber by an inert gas flow, typically N_2 (A_3). The new surface, terminated by fragments of TMA (B_0), is then exposed to H_2O (B_1), analogous to step A_1. Again, the surface is saturated with precursor (B_2) before another purge (B_3), leaving an OH-saturated surface similar to the starting point (A_0), but with the addition of an Al_2O_3 layer. As this reaction is self-limiting, it can be repeated to deposit one monolayer per cycle, until the desired thickness is obtained.
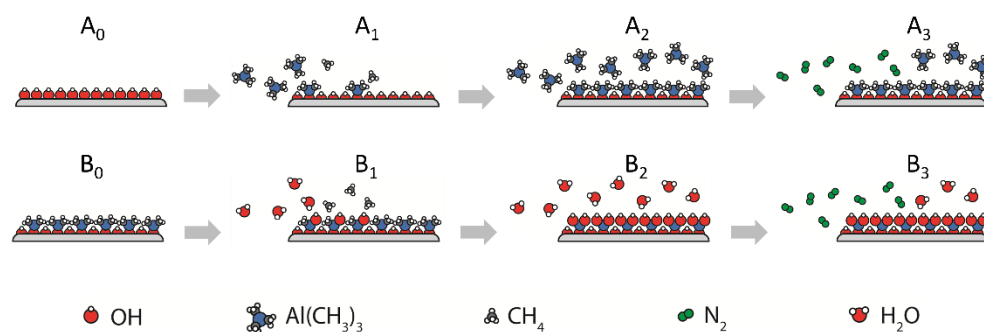

Figure 3.1: An idealized cartoon of the TMA/H_2O process for deposition of Al_2O_3 by ALD. The gas flow direction is left to right.

Typically, well-behaving ALD processes have a temperature range within which the growth rate, or growth per cycle (GPC), remains unchanged. When this is the case, it is an indication that the surface is completely saturated with precursor molecules for every cycle (Figure 3.2 M1). For larger precursor molecules, steric hindrance can be an issue, as some reaction sites are "shielded" by precursor fragments. In some cases, an increase in temperature might lead to reconstruction of such a surface. The reaction can

still be self-limiting even though a slight increase in GPC is observed within the ALD window (Figure 3.2 M2). At lower temperatures, a process can be inhibited by activation energy, resulting in a decreasing GPC (Figure 3.2 L1). If an increasing GPC is observed at lower temperature, it is typically a result of the precursor condensing on the surface (Figure 3.2 L2). In both cases, the self-limiting nature of the process is no longer present. This is also true for temperatures above the ALD window. Desorption or dissociation of species on the surface can be the cause of a decreasing GPC at higher temperatures (Figure 3.2 H1), while an increase in GPC is most often observed when the precursor decomposes (Figure 3.2 H2).[112]
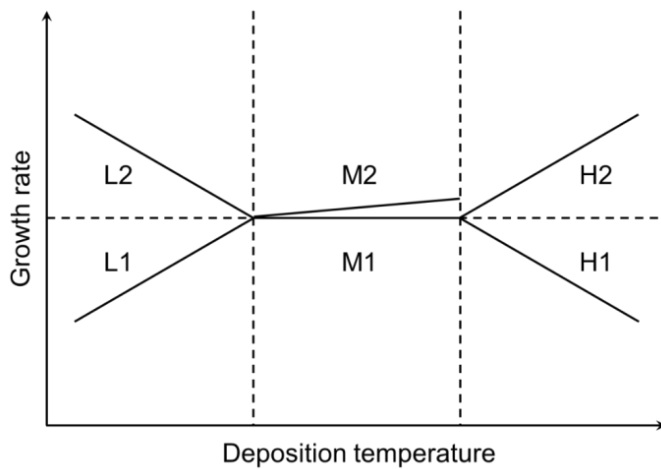
Figure 3.2: The different temperature regions of a typical ALD process.

The focus of the current work is oxides, and although other compounds have been deposited by ALD, they will not be discussed here.

3.2 Complex oxides by ALD

Precursor molecules are usually larger than the (initial) density of reactive sites on the surface. Consequently, steric hindrance is the most important factor determining the GPC of a given process. This is normally not a problem for binary oxides, as it only affects the number of cycles required for a desired thickness. However, to deposit ternary oxides two binary oxide processes are pulsed alternatingly, effectively creating a super-cycle to grow the ternary oxide. If one of the cation precursors is much larger than the other (the largest difference is usually between the cation precursors), the deposited composition can deviate considerably from the pulsed stoichiometry. This is quite intuitive when considering the GPC of binary oxides, but even if the GPC is the same, a 1:1 pulsing ratio between two cation processes does not necessarily result in a 1:1 cation composition for the ternary oxide. This could be explained by different processes requiring different reactive sites. For instance, a process with water as co-reactant would typically result in OH-groups covering the surface as an intermediate step, while ozone based processes might require other surface species. In some cases, this can be

overcome by re-activating the surface, either by implementing a pulse of the next oxidant (e.g. ozone) before the second binary oxide process, or simply by repeating the whole cycle for the second binary oxide. For some ternary oxide processes, this is not an issue, even when different oxidizing agents are used.

Finding the optimal pulsing ratio between two binary oxide processes to obtain a desired ternary composition is usually done by trial–and–error. For ternary oxides, this is not a huge undertaking, but for more complex oxides (quaternary oxides etc.) it can be quite tedious. Based on the work by Ylilammi[113] regarding the surface area that precursor molecules cover (or rather precursor molecule fragments) Lie et al.[114] developed a model to predict the pulsed ratio of binary oxides needed to deposit the wanted composition. This model is also valid for ternary oxides, and can be employed to reduce the number of test depositions needed to develop a new process. Given the binary oxides AO and BO, the model gives a set of equations:

$$D_A = \frac{P_A U_A}{P_A U_A + P_B U_B} \tag{3.1}$$

$$D_B = \frac{P_B U_B}{P_A U_A + P_B U_B} \tag{3.2}$$

$$1 = D_A + D_B \tag{3.3}$$

where D_M represents the deposited stoichiometry, P_M the pulsed stoichiometry and U_M the relative growth rate (or surface utilization coefficient) of element M. Expressed in terms of P_M, equations (3.1), (3.2) and (3.3) take the form:

$$P_A = \frac{D_A U_A}{D_A U_A + D_B U_B} \tag{3.4}$$

$$P_B = \frac{D_B U_B}{D_A U_A + D_B U_B} \tag{3.5}$$

$$1 = P_A + P_B \tag{3.6}$$

Absolute values for the surface utilization coefficient can be calculated from the growth rates of the binary oxides, but in practice only relative values are needed. After the composition of a deposited film has been determined, the model is fitted by adjusting the relative growth rate of one of the binary processes (with the U_M of the other set to 1) to yield an estimate of the pulsing ratio needed to deposit the desired stoichiometry.

For convenience, when addressing complex oxide systems, the whole cycle for depositing for instance a ternary oxide will be referred to as a super-cycle. In this context, a sub-cycle refers to the binary oxide process, even though this process itself consists of two half-cycles.

3.3   Advantages and limitations

ALD has some major advantages over other thin film deposition techniques. Two of the most attractive properties for the current project is the excellent control of stoichiometry and the ability to control the deposited thickness down to less than one atomic layer.

These traits are of course dependent on the process. For some systems, e.g. processes involving group 1 cations, it is not possible to incorporate more than 50% of the alkali constituent,[115] but for most systems all compositions between end-members can be deposited.[116] Sometimes, a certain stoichiometry is favored and can actually stabilize the system, as seen in the $La_{1-x}Ca_xMnO_3$ system.[117] A stabilizing effect was also observed in this work when depositing $NiTiO_3$. A distinct drop in the thickness gradient was accompanied by an increase in GPC for a 1:1 Ni:Ti composition (Figure 3.3).
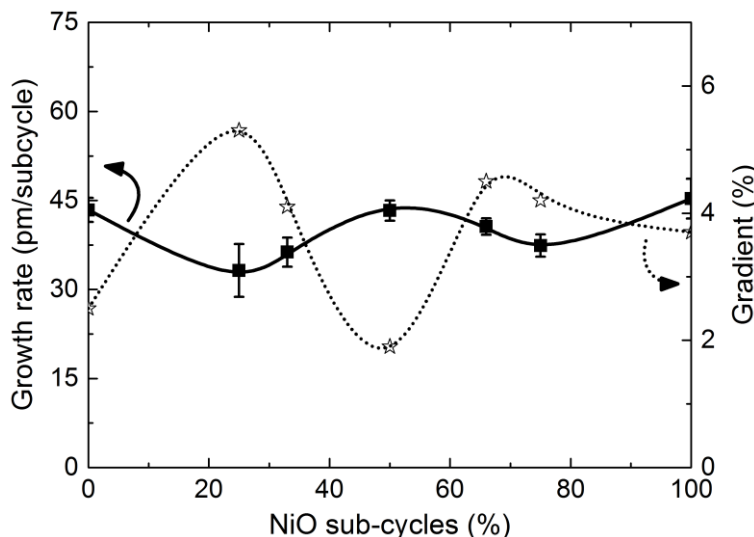
Figure 3.3: Growth rate (solid line with filled squares) and gradient along flow direction (dotted line with open stars) *versus* fraction of Ni pulses (in terms of NiO sub-cycles) in the $Ni_xTi_{1-x}O_3$ system. All depositions were made at 250 °C on Si(100) substrates.

As mentioned above, the GPC of a process, and hence the thickness control, is mostly affected by the size of the ligand. This is also true for growth of complex oxides, but in addition, the pulsed ratio of the binary processes to achieve the correct stoichiometry comes into play. If the pulsing ratio needed to achieve a certain composition is very large it might affect the ability to deposit ultrathin films, or complicate homogeneous doping. The latter can be compensated for by reducing the density of reactive sites by temporarily functionalizing the surface.[118] In addition, intimate mixing of the binary oxides is jeopardized, possibly leading to separate layers of the binary oxides. Even though the average chemical composition of the film is correct, annealing might be necessary to obtain a crystalline film with the desired

crystal structure, unless a layered structure is the goal. Usually, ALD grown films are deposited at a considerably lower temperature compared to other techniques. Still, although the deposition temperatures are low, usually in the range up to a few hundred degrees Celsius, it is not uncommon that crystalline, or partly crystalline, films are deposited directly.

The largest obstacle in the current project relates to difficulties with depositing reduced (oxide) phases by ALD. Today, most oxide processes consist of a metalorganic cation precursor in combination with O_3, O_2, or H_2O. To have a functioning precursor pair their reactivity towards each other needs to be sufficiently high. If the goal is to maintain a lower oxidation state, an obvious choice is to use H_2O as the co-reactant, due to its availability, ease of handling and lack of oxidizing power. However, this requires sufficient reactivity with H_2O, which is not always the case. Using O_3 instead results in full oxidation of the metal precursor, and the resulting films can furthermore be prone to carbon incorporation (usually as carbonate). Apart from some examples with the use of H_2O_2, little work has been done to explore other oxygen sources, e.g. alcohols or acids. Effort is rather put into designing more reactive metal organic precursors. One example is the selective deposition of Fe_2O_3 or Fe_3O_4 from bis(2,4-methylpentadienyl)iron ($Fe(2,4-C_7H_{11})_2$), and O_3 or H_2O_2, respectively.[83]

4 Techniques and characterization

4.1 Atomic layer deposition

Thin films were deposited using a commercial F-120 Sat continuous flow reactor from ASM Microchemistry. All depositions included single crystal Si(100) substrates for thickness measurements, while selected depositions included various other single crystal oxide substrates for structural and magnetic characterization. N_2 was used as carrier and purging gas for all depositions, and was separated from air in a nitrogen generator (Schmidlin UHPN3001 N_2 purifier, >99.999% N_2+ Ar purity). This gas was additionally dried by passing it through P_2O_5 and remains of O_2 were removed by means of a Mykrolis gas purifier. The reactor pressure was around 3 mbar during depositions. O_3 was produced by feeding O_2 (99.6%, AGA) into a BMT 803 N ozone generator (BMT Messtechnik GMBH), with a claimed O_3 concentration of 8%. For processes utilizing H_2O as co-reactant, de-ionized water (type 2) was used. Other precursors are presented in chapter 5.

4.2 Techniques utilizing X-rays

4.2.1 X-ray diffraction

X-ray diffraction (XRD) measurements in $\theta/2\theta$ geometry were performed with a Bruker AXS D8 Discover diffractometer. The instrument was equipped with a Ge(111) monochromator to provide Cu Kα_1 radiation, and a LynxEye detector. There are two important aspects to keep in mind when examining thin films with XRD in a $\theta/2\theta$ setup: firstly, the intensities of substrate reflections are usually several orders of magnitude larger than the intensities of film reflections. This is because the penetration depth of Cu Kα radiation for most substances is in the range of 0.1–10 μm[119], while the thickness of the film is usually much less. As a result, the amount of deposited material interacting with the beam is rather small (compared to the substrate). Actually, the intensity from film reflections can be so small that they hardly can be distinguished from the background/noise. Secondly, thin films can have a high degree of preferred orientation. Since the incident and exiting angles of the X-ray beam is coupled in a $\theta/2\theta$ scan (symmetric scan), only information about crystal lattice spacing along the substrate normal (specular reflections) is obtained, assuming that the sample has been properly aligned with the instrument reference frame. In the case of thin films with a high degree of tilt, the data can be somewhat obscured and might not be representative for the actual state of the sample. To at least average out potential misalignment, the sample was rotated around the substrate normal (φ rotation) during the measurement. Conventional $\theta/2\theta$ scans are most suitable for powder samples, but can also provide good and lucid data for thin films. All the presented diffractograms in this thesis have been analyzed using substrate reflections as an internal standard.

To lengthen the path travelled by the X-rays in the thin film, grazing incidence X-ray diffraction (GIXRD) may be employed. For this type of scan, the incoming (ω) and exiting angles (2θ) of the beam are not coupled. Instead, the incident beam is fixed at a low (grazing or glancing) angle, with respect to the sample surface, while only the exiting angle (detector) is moved along the 2θ circle. The advantage of using this configuration is that the X-rays travel a longer distance within the film and a better signal-to-noise ratio is achieved. A consequence of the GIXRD geometry compared to a symmetric scan is that the scattering vectors will not coincide with the surface normal (except for $2\theta = \omega$), but deviate exponentially from it. This results in the absence of reflections from a single crystal substrate, as they are "points" in reciprocal space. However, the same goes for a single crystal films, or films with a strongly preferred orientation. GIXRD is therefore only useful for polycrystalline films with little or no preferred orientation.

All GIXRD measurements presented here were collected with a PANalytical Empyrean diffractometer, equipped with a Cu Kα source powered at 45 kV/40 mA, a parallel beam X-ray mirror and a proportional point detector (PW 3011/20). The same instrument, but fitted with a PixCel 3D detector instead, was used to collect reciprocal space maps (RSM) and φ-scans.

4.2.2   X-ray reflectivity

As with $\theta/2\theta$ scans, the incident and exiting angles are coupled when performing X-ray reflectivity (XRR). Measurements were performed for low incident angles, usually below 4° (Cu Kα radiation). In this angular range, X-rays are reflected rather than diffracted, and hence, the sample can equally well be non-crystalline. However, the intensity obtained from a scan needs to be fitted to a model. At angles close to 0° the beam is totally reflected from the sample surface. The recorded intensity in this range is very high, but the intensity drops as the X-rays start to enter the sample. The angle where this drop occurs is determined by the density of the film. When the angle is increased even more, X-rays reflected from the sample surface and from interfaces within the sample (both film–substrate and multilayer interfaces) start to interfere, giving rise to oscillations known as Kiessing fringes. The number and periodicity of these oscillations contain information of the sample thickness and the thickness of internal layers (in the case of multilayered samples). The recorded intensity decreases with increasing angle, to a point where the oscillations eventually disappear. A rough sample surface will result in the loss of oscillations at a lower angle than a smoother sample surface.

XRR was used to determine the densities of films, in addition to providing an accurate thickness for single layered films when necessary. Measurements were done on the same instrument, and with the same settings as for GIXRD

measurements. The data was fitted either with the X'Pert Reflectivity software provided by PANalytical, or the GenX software.[120]

4.2.3 X-ray fluorescence

X-ray fluorescence (XRF) was used to determine the cation ratio. Measurements were performed with a Philips PW2400 spectrometer and the data was analyzed with the UniQuant analysis software[121].

4.2.4 X-ray photoelectron spectroscopy

X-ray photoelectron spectroscopy (XPS) data was acquired with a Thermo Scientific Theta Probe MKII. This instrument was equipped with a standard Al Kα source (hν = 1486.6 eV), while the total pressure was kept lower than 10^{-8} mbar. For survey scans, a pass energy value of 200 eV was used, while detailed scans were performed with 50 eV. A Shirley-type background subtraction was employed, before raw XPS spectra were fitted to Gaussian-Lorentzian peak shapes using a non-linear least-squares deconvolution program. The C1s line of adventitious carbon was assigned to an energy of 284.8 eV to correct for charging effects.

4.3   Other techniques and equipment

4.3.1   Spectroscopic ellipsometry

Spectroscopic ellipsometry was used for routine measurements of thicknesses and refractive indices (at λ = 632.8 nm). Data was obtained with a J. A. Woollam α-SE spectroscopic ellipsometer in the 390–900 nm range. The native oxide layer on Si substrates was measured prior to deposition and added to the model when fitting the data with the CompleteEASE software package.[122] For films transparent in the measured wavelength range a Cauchy function was used for modelling. For other films a Tauc-Lorentz model was developed, based on optical properties from transparent regions of the measurement interval.

4.3.2   Spectroscopy

To investigate the band gaps of NiTiO$_3$ films deposited on soda lime glass, optical spectroscopy was performed in the wavelength range 200–1700 nm. The Shimadzu UV3600 instrument used for this was equipped with a photomultiplier tube detector, covering the interval from 200 to 900 nm, while the 900–1700 nm range was covered by an InGaAs photodiode. Band gap values were determined by linear fits to the absorption edge of the Tauc plots of resulting spectra, as described by Tauc et al.[123] FTIR measurements on films containing Fe(II) were carried out using a Nicolet iS 50 FT-IR

Continuum Spectrometer in Attenuated Total Reflectance (ATR) mode. To clarify the data, the signal from a blank Si substrate was subtracted from each spectrum before baseline correction.

4.3.3 Atomic force microscopy

Surface topology was examined by atomic force microscopy (AFM), using a Park Instruments XE-70 in contact mode with a PPP-CONTSCR tip from Park systems. Resulting images were analyzing with the Gwyddion free software package.[124]

4.3.4 Magnetic measurements (PPMS)

Magnetic data was recorded with a Quantum Design Model 6000 Physical Properties Measurement System (PPMS) in DC mode. All measurements were performed for films deposited on $Al_2O_3(001)$ substrates, which were cut after deposition to fit lengthwise into a straw serving as the sample holder. The measuring field was applied parallel to the film surface (longitudinal). For measurement with field perpendicular to the substrate surface (transverse), the same sample was cut into three squares and stacked on top of each other before fitted into a straw. The sample area was estimated by measuring the cut substrates with a caliper, while XRR was used to obtain the thickness and density. For temperature dependent magnetization curves, M(T), a measuring field of 80 kA/m (80 000 A/m) was employed unless otherwise stated. No correction of the data was performed with respect to signals from the substrate, as measurements of an empty substrate revealed values 4–5 orders of magnitude lower than the sample signal (Figure 5.15). Field dependent magnetization loops, M(H), were measured up to the maximum field of the instrument (7000 kA/m). For samples with weak magnetization, this resulted in a negative linear slope of the signal at high fields, originating from the diamagnetism of the substrate (mainly). This background was subtracted from the data to achieve a saturation value for the magnetic moment at high fields.

4.3.5 Rapid thermal annealing

All post-deposition annealing was done in vacuum by rapid thermal processing (RTP) in an MTI Corporation OTF-1200X furnace. The heating program consisted of a 20 min ramp from room temperature to 650 °C, followed by a dwell time of 15 min, and subsequent cooling in the furnace to room temperature.

5 Results and discussion

5.1 Thin film growth and structural characterization

Given the nature of a traditional ALD process for oxides, often with the use of highly oxidizing precursors like ozone, it is easy to see that depositing films with cations of lower oxidation states is difficult. Therefore, alternatives to ALD growth of $FeTiO_3$ were considered in our endeavors towards mimicking the lamellae of mineralogical samples. Given the magnetic structures of related materials (as presented in chapter 2.3), $NiTiO_3$ and $CoTiO_3$ are the only real alternatives. Since only films with a mixture of Co(II)/Co(III) (Co_3O_4) have successfully been deposited by ALD as of now, the present work rather aimed at developing a process for ALD of $NiTiO_3$.

5.1.1 NiO and TiO₂ background and new results

There are several well-known processes for ALD of TiO_2 films. A commonly chosen precursor pair is titanium tetrachloride ($TiCl_4$) and H_2O. However, there is a risk of Cl residue in the resulting films, with reports of values between 0.3 and 7.2 at.%, depending on deposition temperature.[125-128] With the concern of Cl contamination, and considering that the process involves corrosive byproducts, $TiCl_4$ was discarded as precursor. Instead, a different much-used precursor pair was chosen: titanium tetraisopropoxide (TTIP) and H_2O. In contrast to $TiCl_4$, the major concern with TTIP is its lower decomposition temperature, rather than undesired precursor residues. With some degree of decomposition starting at 250 °C,[129] the potential ALD window is considerably smaller. However, the process seems to be unaffected by precursor stability up to 275 °C, and carbon residue is below 0.5 at.% up to 300 °C.[130, 131] In the present work, an ALD window was observed between 125 and 250 °C (Figure 5.1).
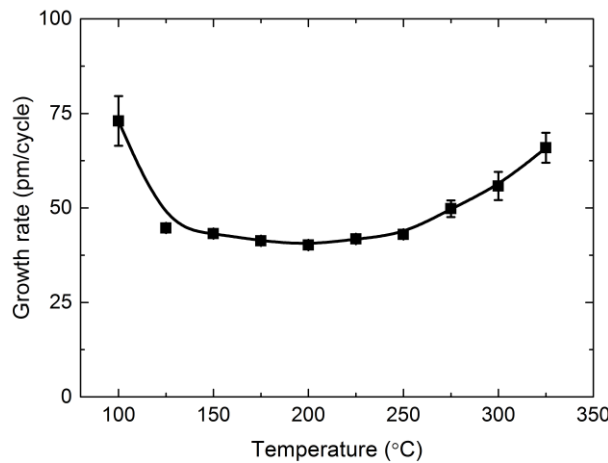
Figure 5.1: Growth rate of TiO₂ films as a function of deposition temperature. An ALD window is observed in the range 125−250 °C.

Choosing a precursor for deposition of NiO was more challenging. Ni containing films deposited by ALD was first reported in 1997,[74] using Ni(thd)$_2$ and O$_3$ to deposit LaNiO$_3$. However, data for the binary processes were not presented. Since then, a range of different precursor combinations have been explored, but they either have narrow ALD windows at low temperatures or simply no ALD window at all.[132-134] The latter is the case for Ni(thd)$_2$ as later work has shown.[135] The most promising process seemed to be Ni(acac)$_2$ combined with O$_3$, as reported by Utriainen et al. in 1998.[136] No data on the effect of deposition temperature were presented in the study, but onset of decomposition was at 280 °C. Thus, a first step was to reproduce the results of Utriainen et al. to see how the process could indeed become compatible with the TTIP/H$_2$O process.

As shown in Figure 5.2, the growth rate of NiO remained unchanged at 45 pm/cycle between 200 and 250 °C. This growth rate is comparable to what was reported by Utriainen et al., with approximately the same O$_3$ dose.
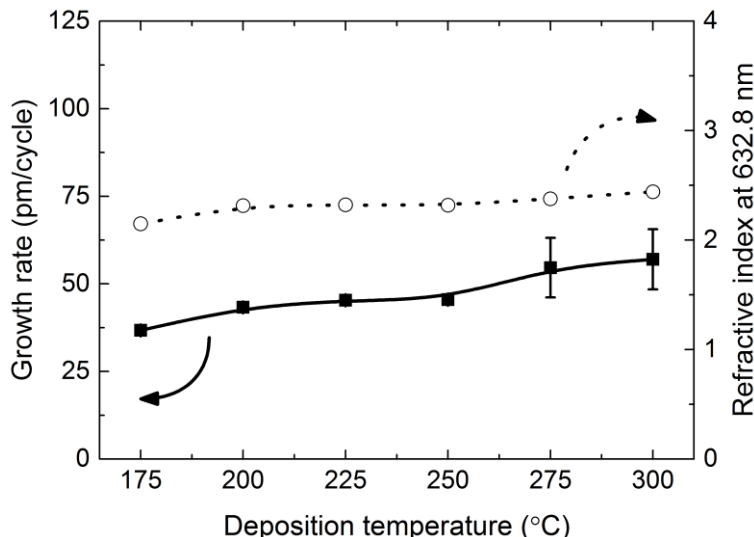
Figure 5.2: Growth rate (solid line with filled squares) and refractive index (dotted line with open circles) of NiO films as a function of deposition temperature. An ALD window exists in the range 200–250 °C.

The deposited films were studied by $\theta/2\theta$ X-ray diffraction (XRD). All NiO reflections were detected for all chosen deposition temperatures upon careful inspection. NiO (200), however, was by far the most dominant (Figure 5.3).
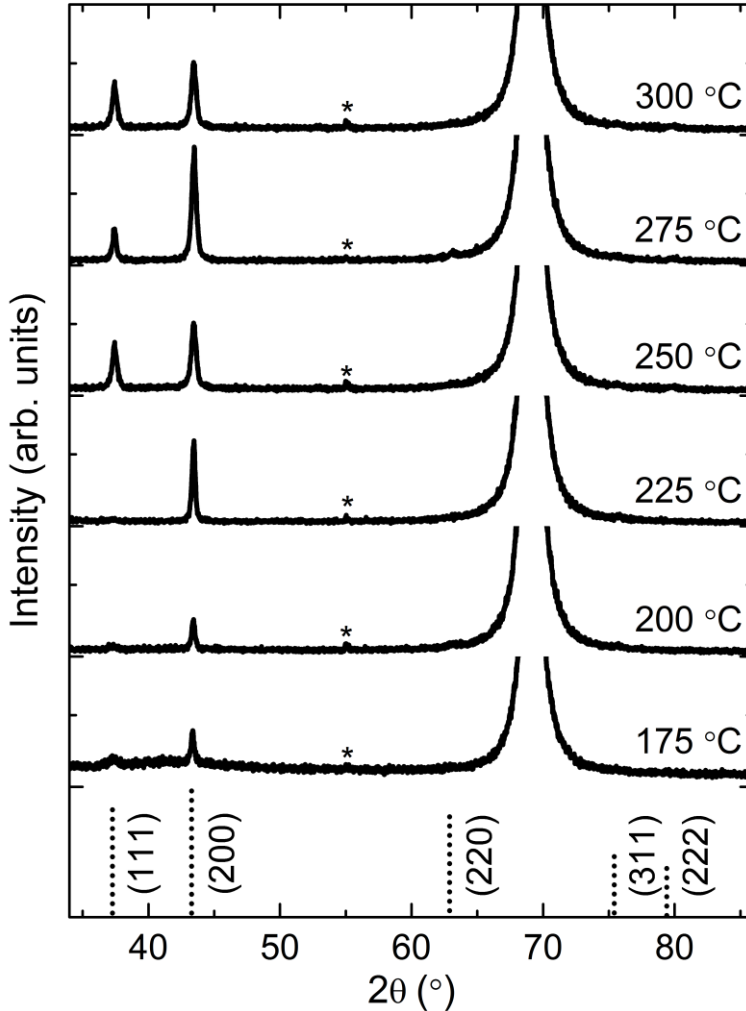
Figure 5.3: $\theta/2\theta$ diffractograms of NiO films deposited on Si(100) at different deposition temperatures as given in the figure. Dotted lines at the bottom indicate positions of allowed reflections from NiO (PDF #04-011-8441). The minor bump at * is an instrumental artefact, while the Si (400) substrate reflection appears at $2\theta = 69°$.

In conclusion, the ALD window of the NiO/O_3 process overlaps well with that of the TTIP/H_2O process, and a combined process seems possible.

5.1.2   Deposition of NiTiO$_3$

Binary processes for NiO and TiO$_2$ were combined at a deposition temperature of 250 °C, and a 1:1 Ni:Ti content was found for a 1:1 subcycle ratio (Figure 5.4). Other subcycle ratios indicated that the ratio of subcycles was directly mirrored in the composition of the film, resulting in a linear relationship between number of NiO subcycles and composition.
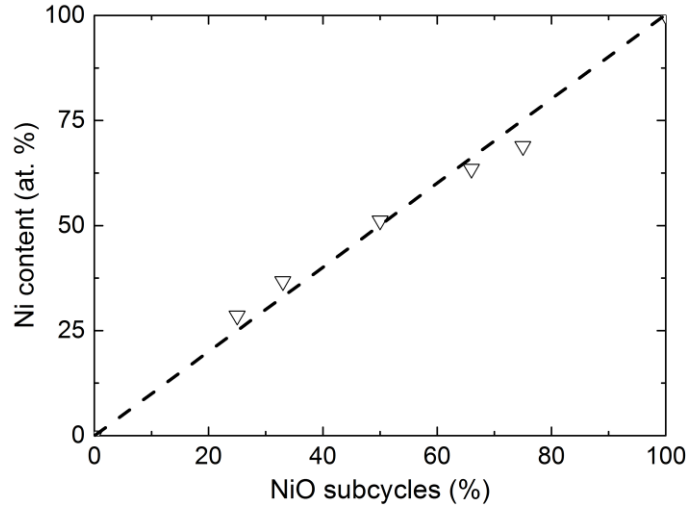
Figure 5.4: Ni content (as measured by XRF) in Ni$_x$Ti$_{1-x}$O3 films *versus* fraction of Ni pulses (in terms of NiO subcycles). All depositions were made at 250 °C on Si(100) substrates. Error bars are within the size of data points.

Further investigations showed an inverse relationship between growth rate and thickness gradients as a function of composition (Figure 5.5). The highest growth rates and smallest gradients were found for the end-members and the 1:1 composition.
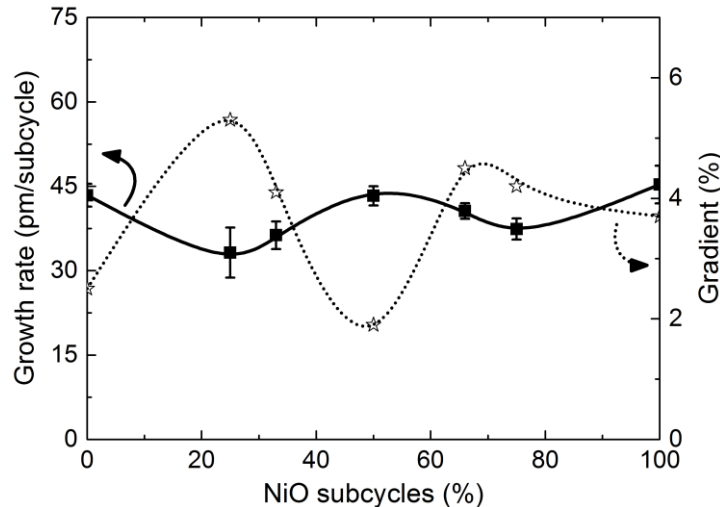
Figure 5.5: Growth rate (solid line with filled squares) and gradient along flow direction (dotted line with open stars) *versus* fraction of Ni pulses (in terms of NiO subcycles). All depositions were made at 250 °C on Si (100) substrates. Error bars not visible are within data points.

Studies on the effect of the deposition temperature revealed an ALD window in the range 175–275 °C, within which the changes in growth rate and film composition were negligible (Figure 5.6). The linear relationship between thickness and number of (super) cycles for films deposited at 250 °C supported the ALD nature of the process (inset in Figure 5.6).
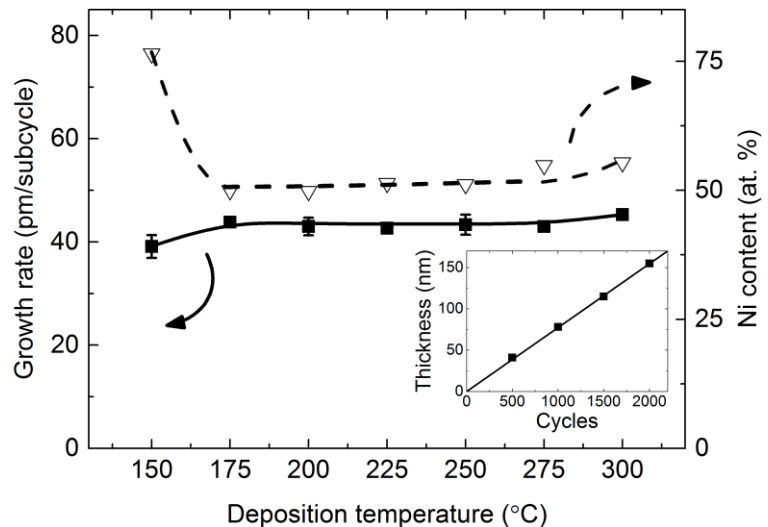
Figure 5.6: Composition (dashed line with open triangles) and growth rate (solid line with filled squares) *versus* **deposition temperature for films made with a 1:1 NiO:TiO₂ pulsing ratio. Thickness** *versus* **number of deposition cycles for films deposited at 250 °C is shown in inset.**

XRD revealed a preferred [00l] direction of growth for $NiTiO_3$ at all deposition temperatures (Figure 5.7). For all the as deposited samples the (006) reflection in the diffraction patterns was shifted slightly towards lower 2θ angles, compared to literature values (PDF# 01-075-3757). This could be interpreted as tensile strain along the c axis. The film relaxed upon annealing, as the (006) was shifted to within 0.05° 2θ of the value reported in literature for all investigated samples.
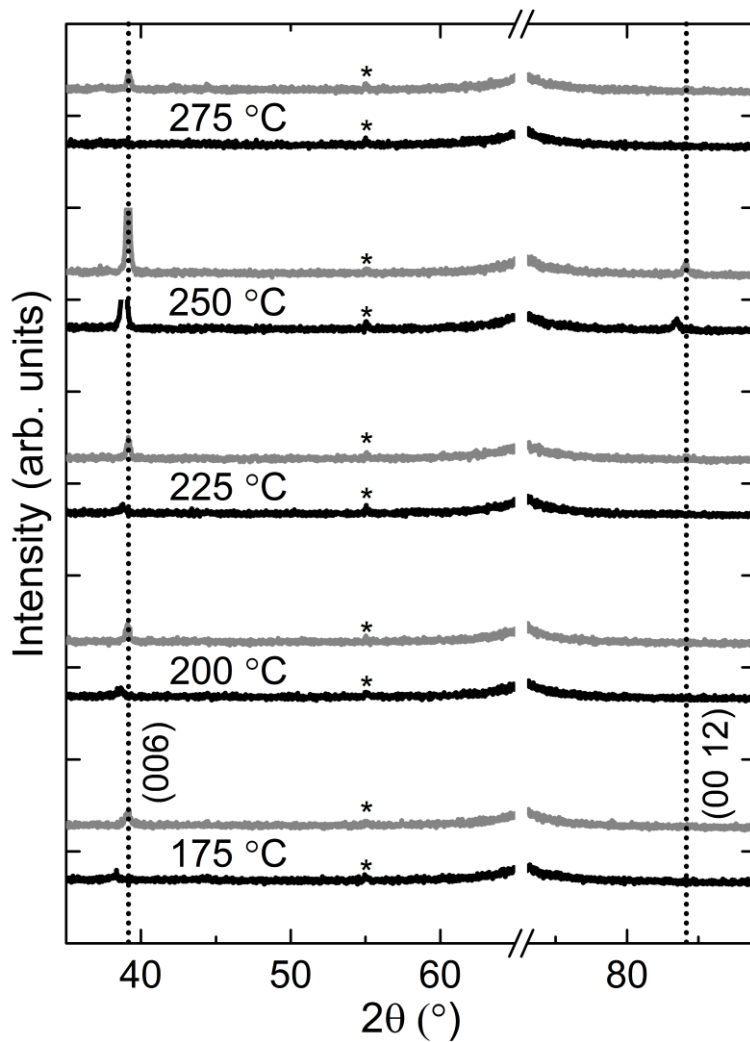
Figure 5.7: $\theta/2\theta$ **diffractograms of NiTiO$_3$ films before (black) and after annealing (grey) at 650 °C for 15 min, with accompanying deposition temperatures indicated in between. All depositions were made with 500 supercycles, apart from the film deposited at 250 °C (1500 supercycles). Positions for NiTiO$_3$ (006) and (00 12) from literature are given as dotted lines (PDF# 01-075-3757). Si (400) at 69° is removed for clarity, while * represents an instrumental artefact.**

5.1.3 Growth of NiTiO₃ on oxide single crystal substrates

The (001) preferred orientation of as deposited $NiTiO_3$ (NTO) films, even on Si substrates with a native oxide layer,[a] is advantageous with respect to characterization of possible magnetic properties of the targeted multilayered structures. However, $NiTiO_3$ is quite interesting in itself, as slight variations in the symmetry of the crystal structure has drastic effects on the properties.

Above 1292 °C, the Ni and Ti atoms are randomly distributed in bulk $NiTiO_3$. This disordered arrangement is the same as for hematite (Fe_2O_3) and α-Al_2O_3 (henceforth only referred to as Al_2O_3), the corundum type structure, with space group symmetry $R{-}3c$ (Figure 5.8, left). Upon cooling, the atoms arrange in alternating layers perpendicular to the c axis, just as for $FeTiO_3$ (ilmenite). With this arrangement the c glide plane is lost, and the symmetry is $R{-}3$ (Figure 5.8, middle). The oxygen sublattice is actually also similar to that of the $LiNbO_3$ structure ($R3c$). However, for the latter, different types of cations alternate both along and perpendicular to the c axis (Figure 5.8, right), inversion symmetry is thereby lost, and interesting electrical and optical properties emerge.


$R{-}3c$ $R{-}3$ $R3c$
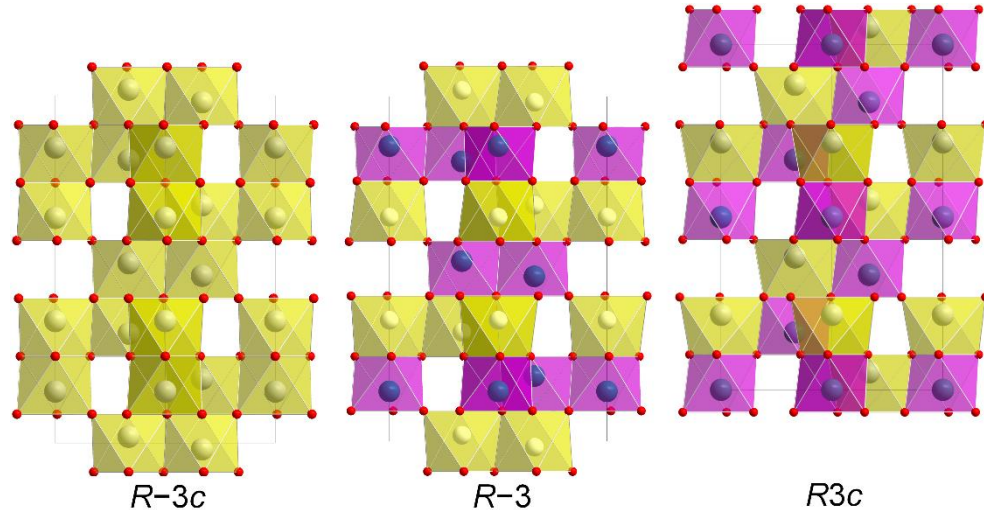
Figure 5.8: Cartoon of various $NiTiO_3$ related structures. In the (disordered) corundum structure (left), cations are randomly distributed, and the symmetry is $R{-}3c$. The (ordered) ilmenite structure (middle) has alternating layers of different cations along the c axis, which changes the symmetry to $R{-}3$. Closely related is the $LiNbO_3$ structure (right), where the cations are alternating both perpendicular and along the c axis, resulting in $R3c$ symmetry.

Although $FeTiO_3$ has been synthesized with the $LiNbO_3$ structure at high pressure,[137, 138] this polymorph has not been unambiguously observed for $NiTiO_3$.[139-141] Determining if the symmetry is $R{-}3c$ or $R3c$ is hard with X-ray diffraction alone. The difference in unit cell parameters between such polymorphs is small and effects from strain and off-stoichiometry is likely to

---

[a] If not removed, the native SiO_2 layer on Si inhibits epitaxial growth.

be larger. However, to investigate the possibility for different polymorphic products, depositions of $NiTiO_3$ on $Al_2O_3(001)$, $LaAlO_3(100)$ (LAO), $SrTiO_3(100)$ (STO) and $MgO(100)$ were performed.

To identify film orientations on the various substrates, $\theta/2\theta$ diffraction in Bragg-Brentano geometry was performed. As can be seen from Figure 5.9, all films showed some degree of crystallinity as deposited.
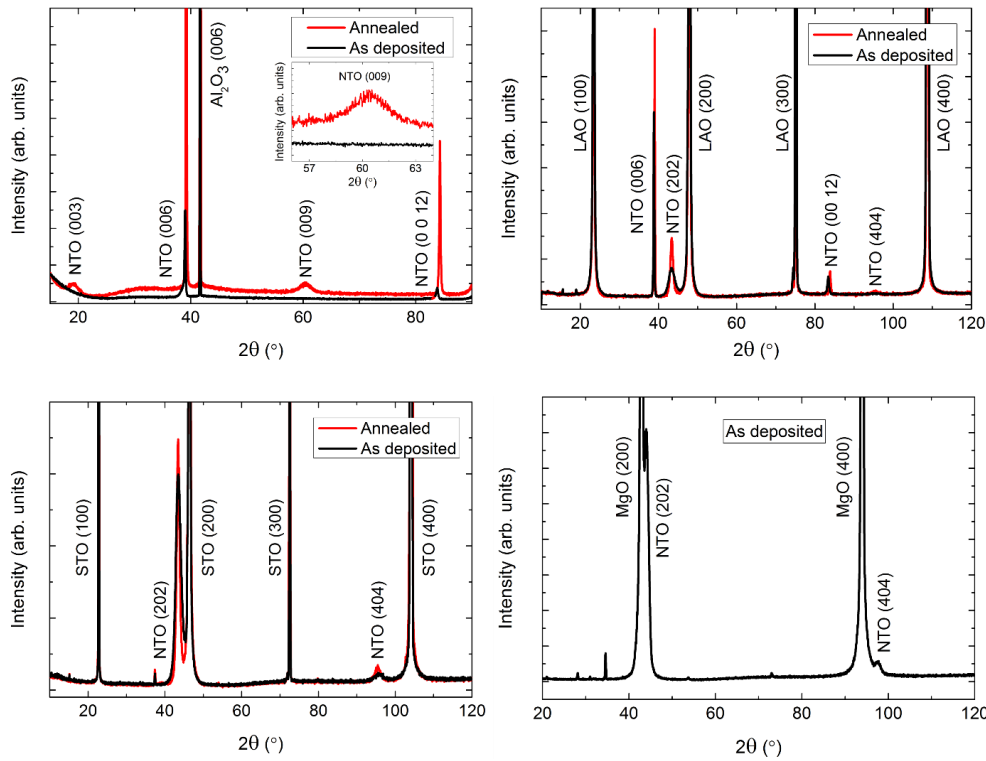

Figure 5.9: $\theta/2\theta$ diffraction of NTO films on various single crystal substrates. Diffractograms of as deposited films are represented by black lines, while annealed films are shown in red.

Films deposited on $Al_2O_3(001)$ were (00*l*) oriented. After annealing, two new, low intensity reflections appeared. The (003) and (009) are not allowed for the disordered $R-3c$ phase. Hence, the annealed film had undergone cation ordering. However, the weak intensity of the additional reflections indicated that only a smaller part of the X-ray illuminated film was ordered. The corundum type $R-3c$ phase of $NiTiO_3$ has previously never been achieved at a temperature as low as 250 °C, or retained at room temperature. The cations in bulk samples of $NiTiO_3$ usually order into layers (ilmenite type) as soon as the temperature is below 1292 °C.[142-144]

On $LaAlO_3(100)$, the deposited films had two orientations: (*h*0*h*) and (00*l*). Although the intensity of the reflections were higher after annealing, no signs of the $R-3$ (ilmenite type) polymorph was observed. If ordering had occurred for the (*h*0*h*) orientation, the (101) and (303) reflections should have been present at $2\theta = 21.4°$ and $67.6°$.

For films deposited on $SrTiO_3(100)$ and MgO(100) only the ($h0h$) orientation was observed. No signs of reflections related to the ordered ilmenite phase was observed (note: the film grown on MgO was not annealed).

To investigate the crystallinity of the films further, reciprocal space mapping (RSM) was performed on symmetrical and asymmetrical reflections as shown in Figure 5.10 and Figure 5.11. A summary of extracted values is given in Table 5.1 at the end of this chapter.

All symmetrical reflections were shifted to slightly larger q values along $q_\perp$ (corresponding to 2θ) upon annealing, indicating a smaller plane distance for the respective orientations. The symmetrical reflections were also used to calculate the length of the c axis for the unit cell of $NiTiO_3$ (See Table 5.1 for details). Annealing resulted in relaxation of the c axis length to within 0.5% of the literature value for all films. The values of the full-width-at-half-maximum (FWHM) along $q_\parallel$ (corresponding to ω, or a rocking curve) were similar for all films, except when grown on MgO, for which they were one order of magnitude smaller. The more pronounced broadening along $q_\perp$, as seen for $NiTiO_3$ on MgO, can be assigned to a strain gradient in the film. For the other films, the broadening along $q_\parallel$ is related to the crystallite size and defects, such as grain boundaries. A larger FWHM corresponds to smaller crystallites, and/or more defects.

Several attempts were made at collecting decent RSMs for $NiTiO_3$ (202) grown on $LaAlO_3$. However, even though the reflection could be identified qualitatively, the intensity was too low for any quantitative analysis.
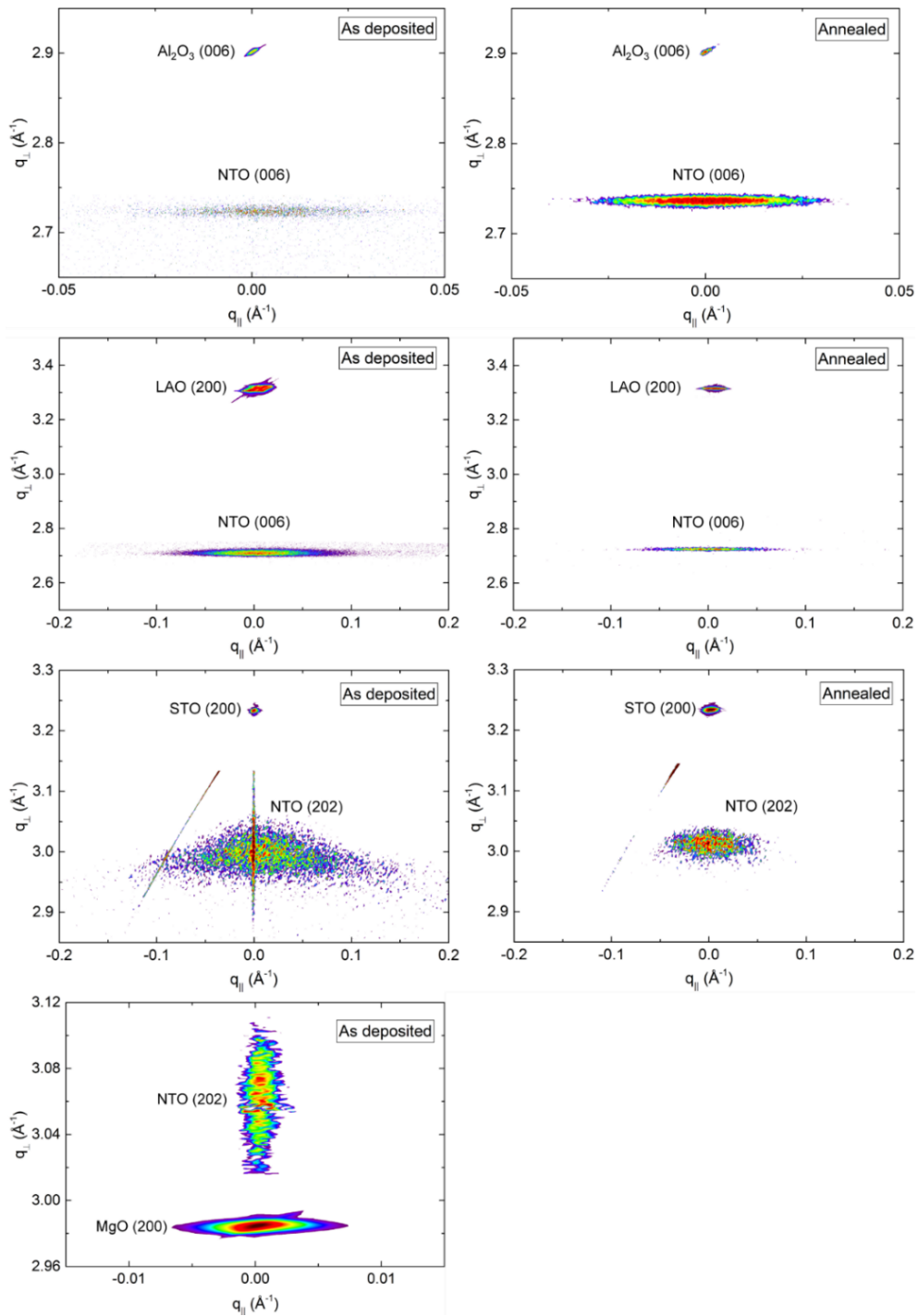
Figure 5.10: Reciprocal space maps of symmetrical reflections from NiTiO₃ films deposited on various single crystal substrates, before (left) and after (right) annealing.
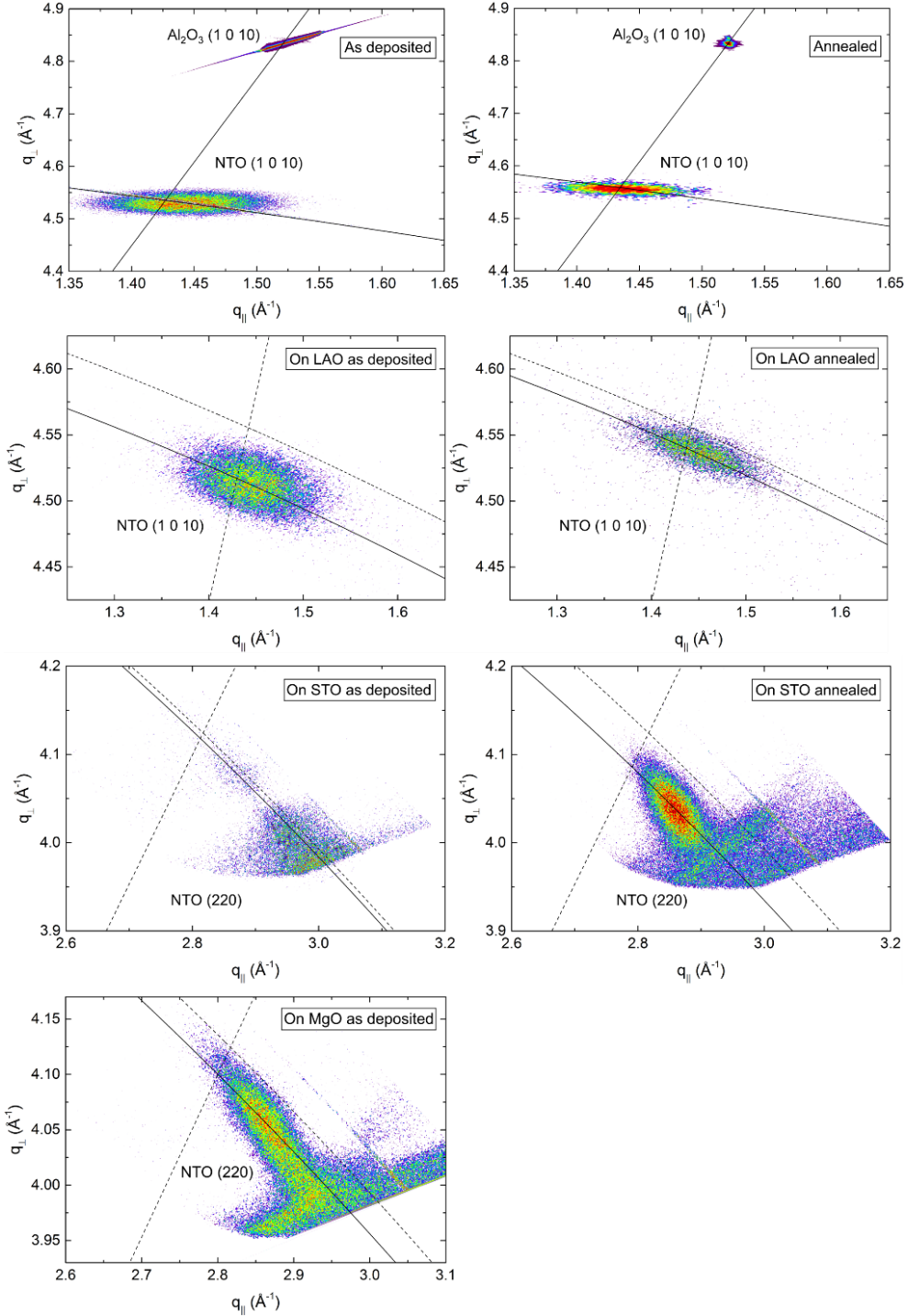
Figure 5.11: Reciprocal space maps of asymmetrical reflections from NiTiO$_3$ films deposited on various single crystal substrates, before (left) and after (right) annealing. The solid arced lines illustrate the intersection with the Ewald sphere. For films on Al$_2$O$_3$ the straight solid line is a guide to the eye that intersects the origin and the Al$_2$O$_3$ (1 0 10) reflection. The intersection of the dashed lines mark the theoretical position of the film reflections.

Asymmetrical scans were performed to gain information on strain, and calculate the length of the a axis of the NiTiO$_3$ unit cell (see Table 5.1 for details). A direct comparison of reflections from the film and the substrate was only possible for NiTiO$_3$ on Al$_2$O$_3$, since for other substrates there exists no direct symmetry relationship with the film.

On Al$_2$O$_3$, the as deposited NiTiO$_3$ film had a slightly longer c axis, and a slightly shorter a axis, compared to the literature value for bulk samples. This is reasonable, assuming the Poisson effect is valid for this system. The unit cell dimensions of Al$_2$O$_3$ are smaller (both the a and c axis) than for NiTiO$_3$. As the NiTiO$_3$ film tried to match the underlying substrate during deposition, the a axis experienced a compressive strain from the substrate. The compression in this direction led to an expansion of the perpendicular c axis. Though the as deposited film was only slightly strained, annealing relaxed the unit cell dimensions even closer to the literature values. The broadening of NiTiO$_3$ (1 0 10) along $q_\perp$ is probably related to defects in the film, such as grain boundaries creating smaller crystallites. Upon annealing, the crystallites grow, reducing the number of grain boundaries and in turn, reducing the FWHM of the Bragg reflection along the Ewald sphere.

Extensive efforts were made to map reflections related to the ($h0h$) orientation of the NiTiO$_3$ film on LaAlO$_3$, but as for the symmetrical (202) the intensity was too low to obtain meaningful data. For the (00l) orientation, the NiTiO$_3$ (1 0 10) reflection was mapped. Interestingly, the reflection was closer to the theoretical position along $q_\parallel$ prior to annealing, while the opposite situation was the case along $q_\perp$. However, the total scattering vector ($q_{tot} = q_\perp + q_\parallel$), was closer to the theoretical (bulk) value for the annealed film than for the as deposited film. Compared to the literature value, the calculated a axis was 0.3% and 0.45% shorter before and after annealing, respectively. From the symmetrical RSMs, the calculated c axis was 0.8% and 0.2% longer before and after annealing, respectively.

Mapping the NiTiO$_3$ (220) for the as deposited film on SrTiO$_3$ proved challenging, as the reflection was just within the geometrical limitations of the instrument. Still, it was possible to fit the position and calculate the a axis, which was 5% shorter than the literature bulk value. A low intensity reflection was visible close to the theoretical position of NiTiO$_3$ (220), indicating that some part of the film was relaxed as deposited. Annealing removed most of the strain, resulting in an a axis calculated to be 1.5% shorter than the literature value. Compared to the literature bulk value, the c axis was longer both before (0.8%) and after annealing (0.5%), complementing the shorter a axis, as described above for NiTiO$_3$ films on Al$_2$O$_3$.

On MgO, the NiTiO$_3$ (220) was close to the theoretical bulk position for the as deposited film. The calculated a axis was 1.2% shorter than the literature value, but contrary to NiTiO$_3$ on Al$_2$O$_3$ the c axis was also shorter (1. 2%).

To establish the epitaxial relationship between film and substrate, φ scans were performed on the asymmetrical reflections (Figure 5.12).
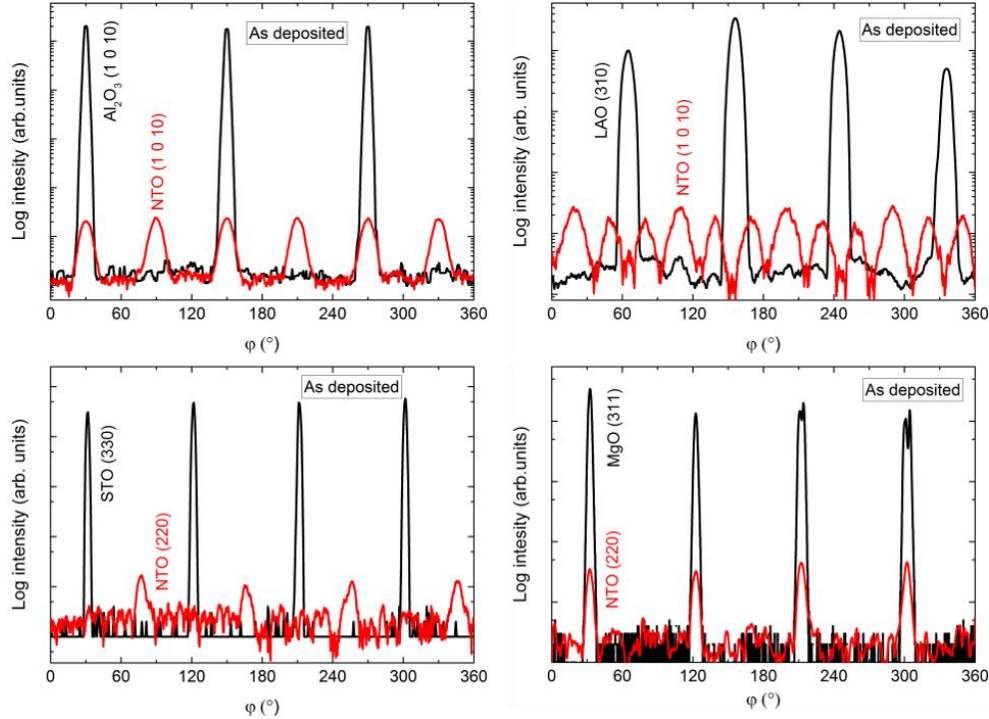

Figure 5.12: φ scans of NiTiO$_3$ films deposited on various substrates. Diffractograms from annealed films are not shown, as the only difference was an increase in intensity.

As Al$_2$O$_3$ and NiTiO$_3$ have the same space group symmetry, the same number of reflections in the φ scan was expected. However, an extra set of reflections were observed for NiTiO$_3$, shifted by 60°. This can be explained by atomic steps on the surface of the substrate. Considering the unit cell of Al$_2$O$_3$ in Figure 5.8 (left), the (001) surface corresponds to the top faces of the oxygen octahedrons. This layer of oxygen atoms has a three-fold symmetry. The oxygen layer making up the bottom faces of the same octahedrons also have a three-fold rotational symmetry, but shifted 60° with respect to the first. As the substrate is a single crystal, atomic steps matching one octahedron height (along the *c* axis) does not change the symmetry. The film on the other hand, can nucleate on both surfaces, yielding crystallites with the same symmetry, but shifted 60° with respect to each other. The epitaxial film||substrate relationship was thus established to be NTO(001)[100]||Al$_2$O$_3$(001)[100].

Without RSMs and φ scans from asymmetrical reflections related to the (*h0h*) orientation of the film on LaAlO$_3$, the exact nature of the two orientations were harder to untangle. There are three possible constellations: (a) a layer of NiTiO$_3$ (00*l*) terminating the film, with a layer of NiTiO$_3$(*h0h*) underneath, directly on top of the substrate; (b) the opposite of (a), with a layer of NiTiO$_3$(*h0h*) terminating the surface and a layer of NiTiO$_3$(00*l*) underneath; or (c) a mixture of both (*h0h*) and (00*l*) oriented crystallites from surface to substrate.

The number of reflections from $NiTiO_3$ on $SrTiO_3$ could be explained in a similar manner as for $NiTiO_3$ on Al_2O_3. A φ scan of single crystalline (*h*0*h*) oriented $NiTiO_3$ would yield only one reflection, but the $NiTiO_3$ film nucleated on different places on the substrate. Since the $SrTiO_3$(100) surface has a symmetry with four identical directions, the crystallites can grow epitaxially along all four, resulting in four reflections in the φ scan. The epitaxial relationship with the substrate was established to be NTO(101)[220]||STO(100)⟨010⟩. Details on the exact direction of the film orientation with respect to the substrate can be found in Paper II.

For $NiTiO_3$ on MgO, the explanation for the number of reflections in the φ scan is the same as with $NiTiO_3$ on $SrTiO_3$. The MgO(100) surface also has four identical directions. The epitaxial film||surface relationship was established to be NTO(101)[220]||MgO(100)⟨011⟩.

Table 5.1: Summary of diffraction results from NiTiO$_3$ films deposited on various single crystal substrates. AD represents ad deposited and Ann annealed. The values for *c* (%) and *a* (%) are relative to the literature values. The ω_{FWHM} values are extracted from symmetrical RSMs along $q_\parallel$, representing traditional rocking curves. Values for ES_{FWHM} are extracted from asymmetrical RSMs along the intersection with the Ewald sphere.

Substrate	Al₂O₃(001)		LAO(100)		STO(100)		MgO(100)
Film orientation	(00*l*)		(00*l*)		(*h*0*h*)		(*h*0*h*)
State	AD	Ann	AD	Ann	AD	Ann	AD
c (Å)	13.84	13.78	13.91	13.83	13.91	13.86	13.62
c (%)	0.36	−0.11	0.81	0.24	0.84	0.47	−1.22
ω_{FWHM} (°)	1.03	0.67	2.26	2.10	3.41	2.50	0.22
a (Å)	5.03	5.04	5.02	5.01	4.79	4.96	4.97
a (%)	−0.13	0.09	−0.29	−0.45	−5.01	−1.52	−1.20
ES_{FWHM} (°)	1.16	0.96	1.49	1.06	1.61	0.77	1.46
# of φ refl.	6		12		4		4

5.1.4 Multilayers of Fe_2O_3/$NiTiO_3$

With basis in the developed stable process for depositing $NiTiO_3$ films, multilayered samples of $NiTiO_3$/Fe_2O_3 were made. Both compounds have magnetic moments in the *ab* plane, and both grow (001) oriented on Al_2O_3(001).[85] Depositions were thus made on Al_2O_3(001) substrates, as this was thought to ease the analysis of the magnetic data.

Since deposition of Fe_2O_3 from $Fe(thd)_3$/O_3 is well-established within our research group, this process was chosen, benefiting furthermore from the possibility of direct deposition of crystalline (001) oriented films on Al_2O_3(001).[85] The only drawback is a low growth rate, at 13 pm/cycle, which proved to become a problem when depositing multilayered films. Due to the reactor design, the precursor reservoir has limited capacity for precursors that require heating. Thus, the multilayered samples were made in steps, breaking the vacuum to the reaction chamber several times to refill precursor. Multilayered samples of Fe_2O_3/$NiTiO_3$ with varying numbers of layers and different (individual) layer thicknesses were made. Unfortunately, only one of these samples was investigated with PPMS due to limited access to the instrument. The investigated sample was comprised of ten bilayers of Fe_2O_3/$NiTiO_3$, as shown in Figure 5.13.
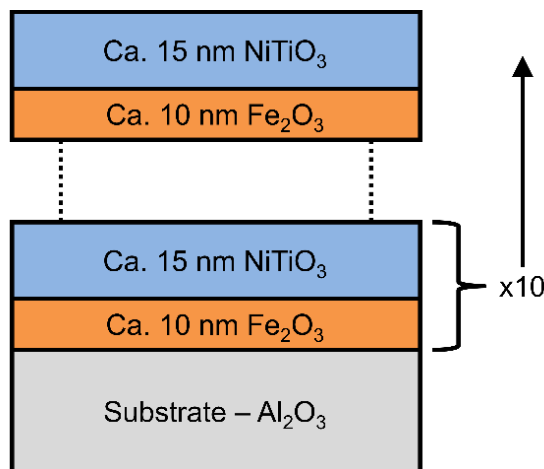
Figure 5.13: Cartoon of a multilayered sample consisting of 10x Fe_2O_3/$NiTiO_3$ bilayers. The thickness of the individual Fe_2O_3 and $NiTiO_3$ layers are estimated from growth rates derived for thicker, single layered films.

Characterizing the exact thickness of the layers was challenging. Whether there was caused by issues with the uniformity of the film due to the process itself,[136] or because the deposition was done in steps is unclear. From the growth rates of single layered films, the thicknesses of Fe_2O_3 and $NiTiO_3$ were estimated as 10 and 15 nm, respectively. However, the thickness of the individual layers as characterized by XRR, or even the total thickness calculated from ellipsometry data, was not determined exactly.

Attempts were made to fit a 20-layer model to the XRR data. Even though a good fit could not be obtained, the data hold clear signs of a multilayered structure (Figure 5.14, left). Estimates of the total thickness and density from ellipsometry and XRR were used to translate the units of the magnetic data. The presence of (001) oriented Fe_2O_3 and $NiTiO_3$ was confirmed by XRD (Figure 5.14, right).
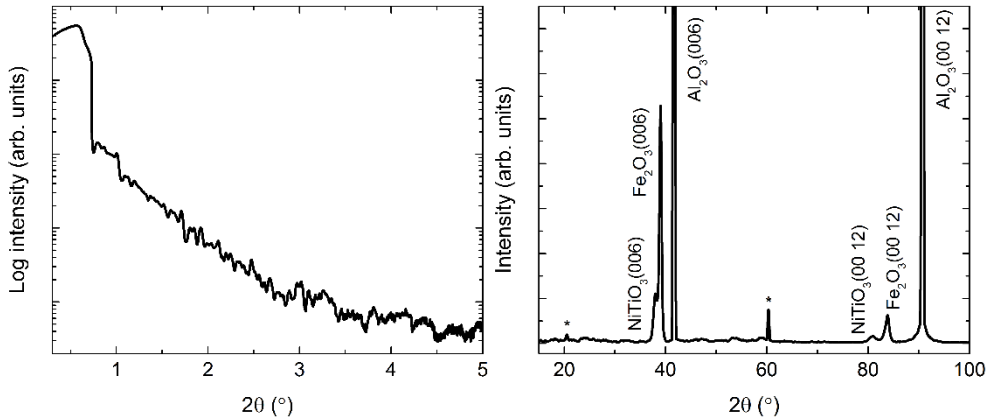

Figure 5.14: The left figure shows XRR data for a multilayered $Fe_2O_3/NiTiO_3$ film on $Al_2O_3(001)$. The right figure shows corresponding XRD data. The (003) and (009) from the substrate are visible at positions marked *.

5.2   Magnetic properties

In order to be able to ascribe certain specific magnetic features to the very nature of multilayered films or their interfaces, it is required to first have detailed insight into the magnetic properties of the separate thin film constituents. The studied single layered film samples were Fe_2O_3 (45 nm) as deposited and $NiTiO_3$ (165 nm) annealed, both (001) oriented on Al_2O_3(001).

5.2.1   Magnetic properties of binary and ternary oxides

For the temperature dependent magnetization, M(T), or susceptibility (χ), a slightly negative signal is expected for the diamagnetic substrate. As seen from the inset in Figure 5.15, the signal from a zero-field cooled (ZFC) measurement of the substrate is close to zero with very low susceptibility values, comparable to data from literature.[145, 146] A field cooled (FC) measurement was also performed (not shown), with values practically identical to the ones obtained from ZFC. Notice what seems to be an instrument or substrate artifact just above 250 K. Figure 5.15 also shows the ZFC susceptibility curve for the $NiTiO_3$ film in the range 5–275 K, with data acquired upon heating, while the Fe_2O_3 film was measured on cooling (effectively FC).
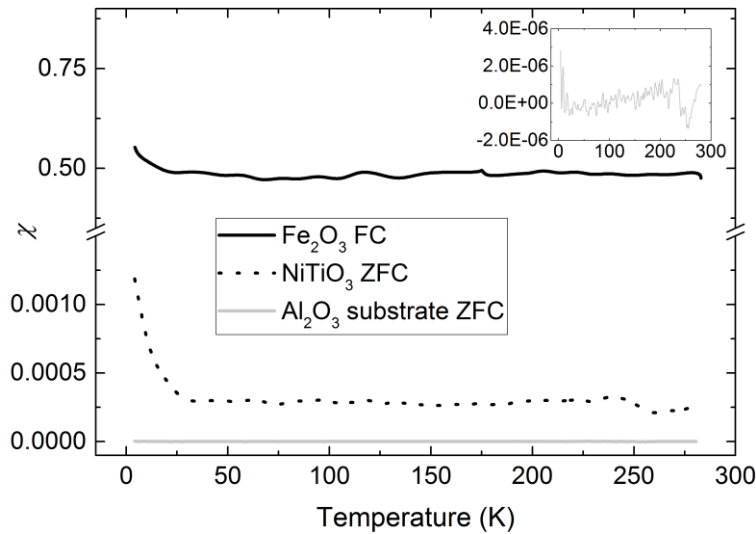
Figure 5.15: Temperature dependence of susceptibility for Al_2O_3 (001) substrate (inset), 45 nm Fe_2O_3 film (solid line), and 165 nm thick $NiTiO_3$ film (dotted line). The substrate and $NiTiO_3$ film were measured as ZFC, while the Fe_2O_3 film was effectively FC during measurement. All measurements were performed in an 80 kA/m field.

Apart from a steep increase in magnetization for temperatures below 30 K, and the artifact at 250 K (also seen for the substrate), no features were observed for the $NiTiO_3$ film. There were no signs of an anti-ferromagnetic transition, which for bulk samples is seen as a peak at 23–26 K. The small positive signal might be due to local paramagnetic contributions, originating from defects in the film.

The same large increase in magnetic response at low temperature was also observed for the Fe_2O_3 film, although starting at a lower temperature (20 K). As with the $NiTiO_3$ film, a small positive susceptibility was observed, again, possibly due to "parasitic" paramagnetism from defects. However, no Morin transition was observed, as might be expected for very small crystals.[101, 147] This indicates that the higher susceptibility value, compared to $NiTiO_3$, could come from the canted antiferromagnetism of Fe_2O_3. In addition, the sample was effectively FC rather than ZFC, which could yield a larger magnetic signal from paramagnetic defects.

Field dependent magnetization was investigated at selected temperatures between 5 and 300 K for Fe_2O_3 and $NiTiO_3$ films. Linear fits of the diamagnetic contribution from substrate and sample holder at high fields were subtracted from all recorded curves. A representative selection of curves for the 45 nm Fe_2O_3 film is shown in Figure 5.16, which also shows the difference between measurements done when orienting the magnetic field parallel (longitudinal) and perpendicular (transverse) to the substrate surface.
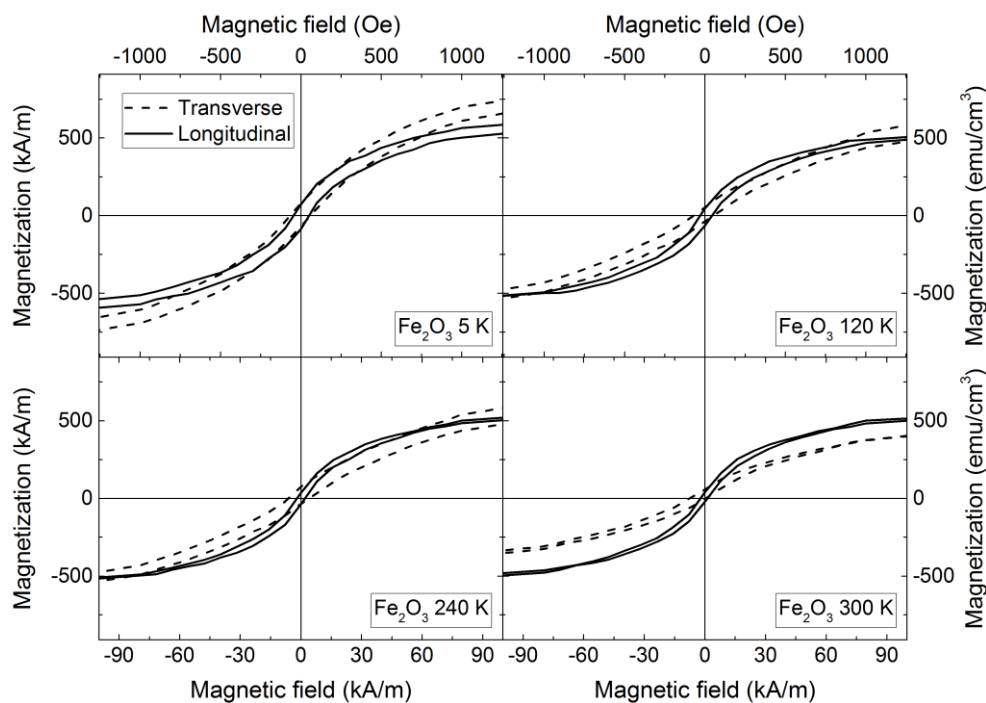
Figure 5.16: Comparison of Fe_2O_3 M(H) curves for transverse and longitudinal sample configurations at selected temperatures, starting at 5 K directly after acquisition of FC M(T) data. Measurements were performed in fields up to 7000 kA/m before heating to the next temperature. Only data up to 90 kA/m is shown for clarity.

A small opening in the hysteresis curve was visible at all temperatures. This was also the case for the data of $NiTiO_3$ below 120 K. Whether this is a real feature or not is debatable. Fe_2O_3 does have an intrinsic magnetic moment, due to the canted antiferromagnetism discussed in chapter 2.2.2. However, the value is closer to 2 kA/m (in a 2.1 kA/m field),[148, 149] much lower than

what is measured here (40–50 kA/m in a 2.1 kA/m field). Further, Höhne et al. points out that s-shaped loops can arise from "a non-central, vertical or lateral position of the sample inside the superconducting detection coils".[150] This artifact is usually observed in systems with a small total magnetic signal, one order of magnitude smaller than the signals recorded here. However, it should not be ruled out that the observed characteristics are not intrinsic properties of the measured materials. The hysteresis opening could also be explained by other artifacts observed when measuring magnetic properties of thin films. Salzer et al. investigated the effect of impurities in Al_2O_3 substrates.[145] They concluded that when investigating weak ferromagnetism in thin films bulk characterization techniques are not adequate. However, signals from the bare substrate they measured were larger than what we observe, indicating that the substrates we used had less magnetic impurities.

Comparison of the saturation magnetization (M_s) and coercivity (H_c) of hysteresis loops from the Fe_2O_3 and $NiTiO_3$ films revealed some interesting features (Figure 5.17). There were no hysteresis opening for the $NiTiO_3$ film above 120 K, but for lower temperatures, the coercivity was always larger than for the Fe_2O_3 film, even with the sudden drop at 5 K. The coercivity increased with lower temperature for both films, but increased more rapidly for $NiTiO_3$. Conversely, the saturation magnetization was higher for the Fe_2O_3 film at all temperatures, but the $NiTiO_3$ film had a much higher relative increase in M_s at 5 K. Disregarding the measurements at 5 and 15 K, the average M_s values were 730 and 45 kA/m for Fe_2O_3 and $NiTiO_3$, respectively.
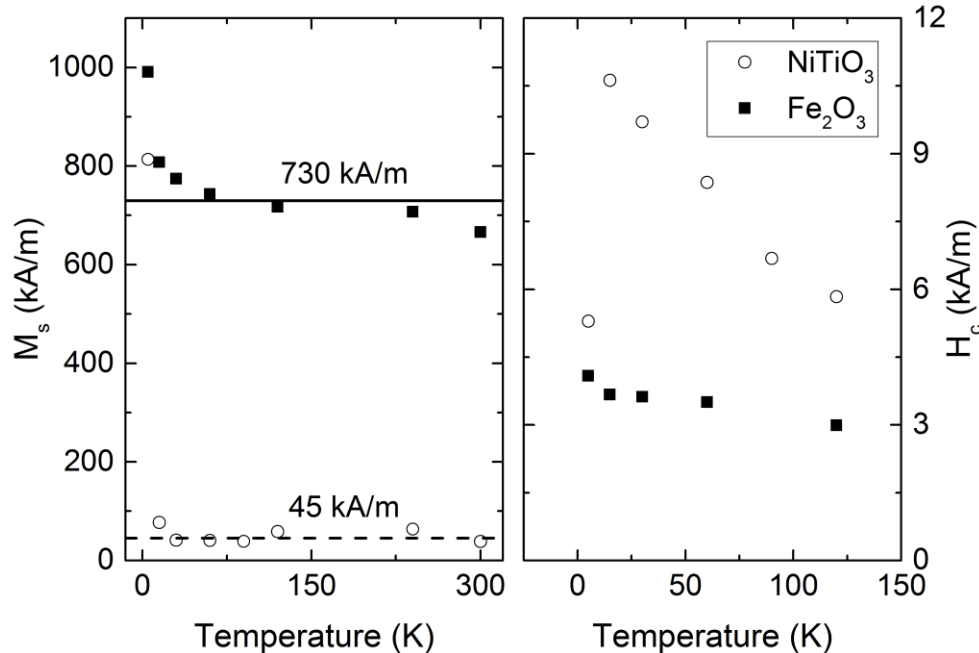

Figure 5.17: Comparison of saturation magnetization, M_s (left), and coercivity, H_c (right), as function of temperature for a Fe_2O_3 (solid squares) and $NiTiO_3$ film (open circles). Average M_s values, disregarding measurements at 5 and 15 K, are given as a solid line for Fe_2O_3 and a dashed line for $NiTiO_3$.

5.2.2 Magnetic properties of Fe_2O_3/$NiTiO_3$ multilayers

The previously described multilayered sample, consisting of 10x(10nm/15nm) Fe_2O_3/$NiTiO_3$ layers on Al_2O_3, was studied by means of PPMS. The as deposited sample was not annealed prior to investigation in order to maintain the layered (hetero) structure, and to avoid formation of $NiFe_2O_4$.[151] The M(T) curves (ZFC and FC, with 400 kA/m measuring and cooling field) revealed no features above ca. 55 K, apart from a slowly increasing (positive) magnetization with increasing temperature. A peak at 53 K, and possibly a second one at ca 30 K, was observed (Figure 5.18).
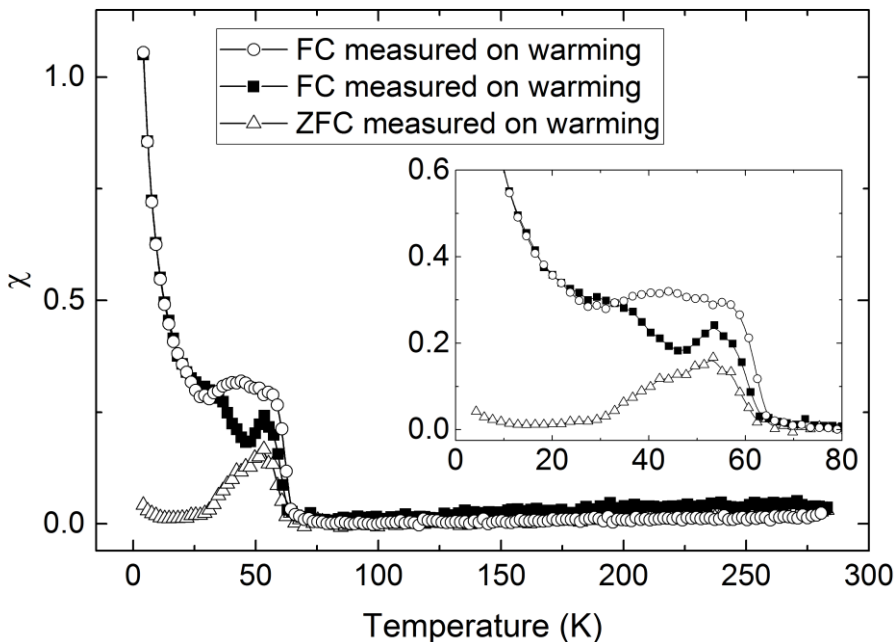
Figure 5.18: M(T) curves (400 kA/m measuring field) for a multilayered Fe_2O_3/$NiTiO_3$ sample. Data was obtained by first zero field cooling (ZFC) the sample to 5 K before measuring on heating (open triangles), then measuring while cooling down—effectively field cooling (FC) the sample (black squares), and finally measuring on heating up to 300 K again (open circles). The inset shows an enlargement of the data below 80 K.

M(T) measurements were first performed at the same measuring field as for the single layered samples (80 kA/m), but the observed features were more protruding in higher fields, as seen clearly in Figure 5.19, where a 800 kA/m measuring field was used.

The M(H) characteristics varied considerably with temperature. As shown in Figure 5.19, at temperatures above 120 K the M(H) curves were clearly s-shaped after correcting for the diamagnetic contribution from the substrate, reaching saturation at ca. 1600 kA/m. Closing in on the peak at 53 K the corresponding M(H) curve is almost linear. At lower temperatures, the M(H) curve becomes clearly s-shape, with superparamagnetic-like characteristics. All M(H) data below 120 K had a much higher signal than the diamagnetic background, and were thus not corrected for the diamagnetic contribution from the substrate.
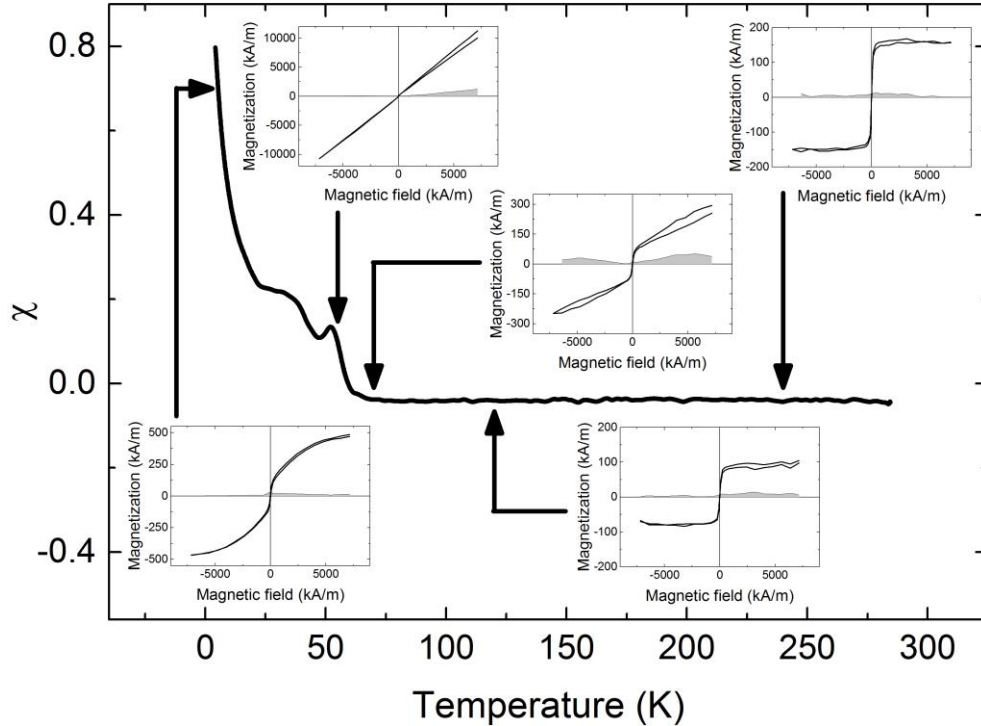
Figure 5.19: Susceptibility (FC) in an 800 kA/m measuring field with insets of M(H) curves at selected temperatures for a multilayered Fe$_2$O$_3$/NiTiO$_3$ film. Grey areas represent the difference between upper and lower part of the hysteresis loops. Only the 120 and 240 K data have been adjusted for the diamagnetic contribution from the substrate.

While there were some similarities with the measurements of the single layered films, there were also distinct differences. Firstly, as with the single layered films, no recognizable antiferromagnetic transition was observed in the M(T) curves and the signal increased dramatically at very low temperatures. In addition, the M(H) curves above 120 K were similar to those from the single layered films. However, the low temperature features in the M(T) curve, right before the steep increase in magnetization, must be a multilayer effect. The associated M(H) curves were also distinctly different. Figuring out the origin of the signals observed proved quite challenging. The peak at 53 K resembled that explained as originating from a spin glass phase by Ishikawa et al.,[44] in the closely related FeTiO$_3$/Fe$_2$O$_3$ system. However, in that system, the peak was depressed at higher measuring fields, a feature opposite of what is observed here. For thin films of Fe$_{1.5}$Ti$_{0.5}$O$_{3-\delta}$, Hamie et al. also observed a similar low temperature peak, and in addition a steep increase at even lower temperatures, just as observed here.[152] They explain the features as a superposition of different magnetic contributions. At high temperatures, the Fe$_{1.5}$Ti$_{0.5}$O$_{3-\delta}$ film had a small positive magnetization, which could be assigned to "a residual small ferrimagnetic contribution (...) with a Curie temperature higher than 300 K." For the multilayered sample we investigated, the magnetization in the same temperature region was slightly negative in an 800 kA/m measuring field, but slightly positive in an 80 kA/m field and approximately zero in a 400 kA/m field. Further, Hamie et al. claim that the low temperature peak they observed was related to a spin

glass state. In our sample, the blocking temperature of such a possible spin glass state would be 65 K. Finally, the steep increase from 20 to 5 K could be explained as paramagnetism associated with independent magnetic moments, just as in the samples investigated by Hamie et al. Whether this is a correct analysis of the observed effects or not, is unclear.

With these obvious issues surrounding the accuracy of the data, investigating the potential presence of exchange bias was difficult. The shaded grey areas of the insets in Figure 5.19 show the difference between the upper and lower part of the M(H) curves. For a symmetrical hysteresis loop—as is expected when exchange bias is not present—the difference between the upper and lower part of the loop should have a center of mass at zero field. A difference was observed for the samples measured here, but the values are varying and seem to be more related to issues described in chapter 5.2.1. The same issues might also be related to why some of the loops are not closed at high measuring fields. It is therefore questionable whether the observations actually represent a real vertical shift or not. A horizontal shift was present at all temperatures (Figure 5.20), but values were comparable to those observed for the single layered $NiTiO_3$ film, and might again come from measuring artifacts, like misalignment.
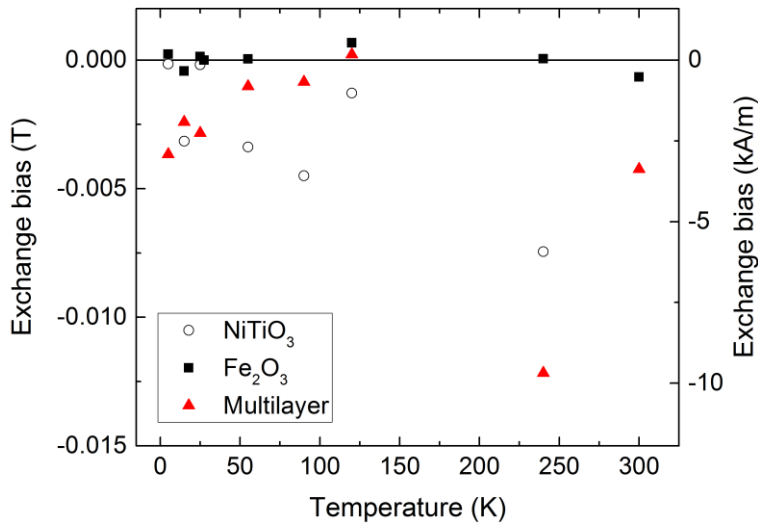

Figure 5.20: Exchange bias (horizontal shift) at zero magnetization for single layered films of $NiTiO_3$ (open black circles) and Fe_2O_3 (solid black squares) as well as a multilayered $Fe_2O_3/NiTiO_3$ sample (solid red triangles).

5.3 Exploring deposition of Fe(II) with a new precursor

At a late stage in the project, a precursor novel to ALD was made available through collaborations with the University of Padova, Italy. The precursor molecule, Fe(hfa)$_2$·TMEDA (hfa=1,1,1,5,5,5-hexafluoro-2,4-pentanedionate and TMEDA=*N,N,N',N'*-tetramethylethylenediamine), consists of a Fe(II) central atom, with two bidentate *β*-diketonate ligands in a *cis* configuration and a bidentate amine (Figure 5.21). Preliminary tests with H$_2$O and O$_3$ as co-reactants were performed, before a combination with oxalic acid was tried.
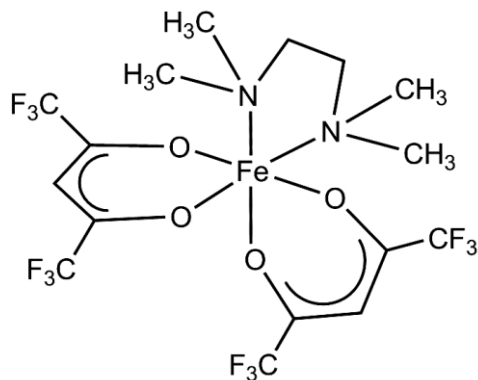
Figure 5.21: Molecular structure of the Fe(hfa)$_2$·TMEDA complex.

5.3.1 Preliminary tests with O$_3$

The precursor was first tested in combination with ozone. However, no ALD window was found within the range of deposition temperatures investigated (Figure 5.22). Instead, the growth per cycle (GPC) increased linearly with increasing temperature. The visual appearance of the films was quite promising with regards to conformality, but a more thorough analysis revealed a thickness gradient of 5–17% at higher temperatures. XPS and GIXRD analysis revealed Fe(III) species in the deposited film, and a crystal structure with random orientation matching that of Fe$_2$O$_3$ (Figure 5.22).
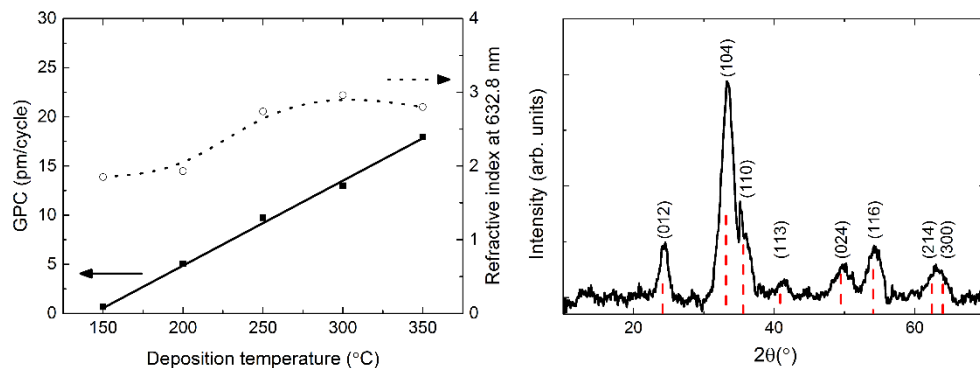

Figure 5.22: Films deposited with Fe(hfa)$_2$·TMEDA and O$_3$, with growth per cycle (GPC) and refractive index of as function of temperature (left) and GIXRD (right). All error bars are within data points. Dashed red lines represent position of reflections for Fe$_2$O$_3$ (PDF# 00-033-0664).

There are certainly ALD processes better suited to deposit Fe(III) containing films. The low growth rate observed here is probably due to the size of the precursor molecule, effectively shielding many possible reaction sites. However, this could be exploited in cases where diluted doping is desirable, and clustering of the dopant should be avoided.[153]

5.3.2   Combination with oxalic acid

With the aim of maintaining the oxidation state of iron, water and oxalic acid were tested as co-reactants. QCM investigations revealed very limited reactivity towards water, while self-limiting growth was observed in combination with oxalic acid, both at 130 and 200 °C. Further tests were performed with combinations of both water and oxalic acid, but the addition of water did little to the overall growth, regardless of position in the cycle.
Having established a self-limiting process with oxalic acid, depositions were performed at different temperatures. The growth rate decreased rapidly upon increasing deposition temperature, and only between 175–200 °C did the growth per cycle remain the same (Figure 5.23).
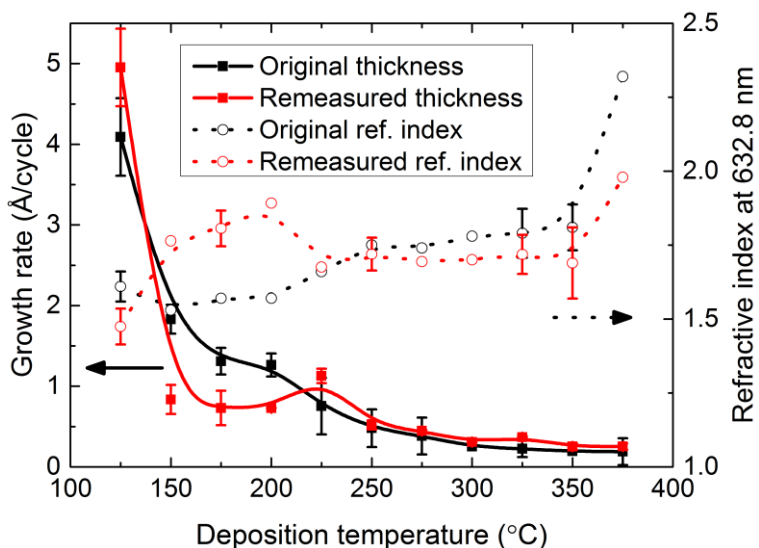

Figure 5.23: Growth rate (solid lines) and refractive index (dotted lines) as function of temperature for films grown from Fe(hfa)$_2$·TMEDA and oxalic acid. Black curves represent measurements done immediately after deposition while red curves are remeasurements of the same films 9 months later.

As the samples seemed stable, they were stored in ambient conditions. However, the thickness was re-measured seven months later, revealing a distinct drop for films deposited in the 150–200 °C temperature range. The refractive index also changed, further emphasizing that a reaction had occurred (Figure 5.23).

No reflections were visible from $\theta/2\theta$ diffraction, and apart from some reflections at low angles, no clear signs of crystallinity were discovered

through GIXRD investigations (Figure 5.24). For hybrid thin films, low angle reflections can originate from a layering of the film, rather than a traditional crystal structure. However, in the present case the observed reflections could not be identified to have any relationship with possible organic fractions from a deposition reaction resulting in a layered structure. Neither could they be linked to any known phases of iron oxalates, hydroxides, oxides or their hydrates. The origin of the reflections thus remains unknown.

FTIR analyses revealed bands related to −OH groups, as well as bands at wavenumbers matching those of the CH_2/CH_3 stretching modes for the TMEDA moiety in the precursor molecule. Despite the obvious incomplete deposition reaction, bands related to the carboxylate moiety and the metal center could also be identified. The positions of those bands were consistent with a bidentate interaction between the ligand and the metal center for all deposition temperatures.
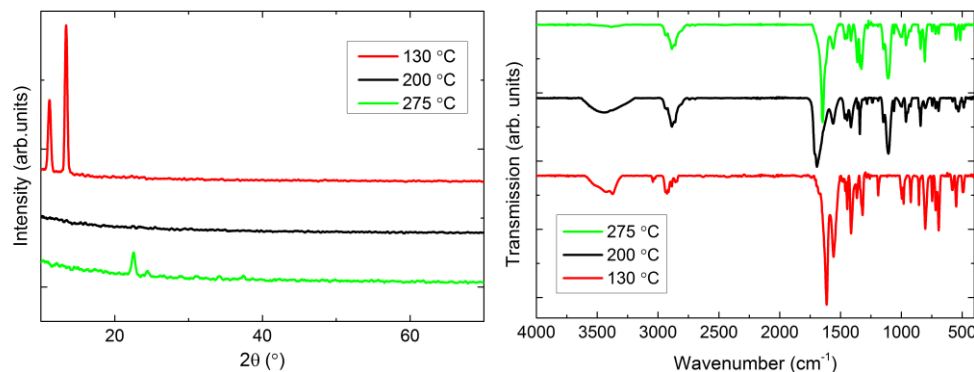

Figure 5.24: GIXRD (left) of films deposited from Fe(hfa)$_2$·TMEDA and oxalic acid at selected temperatures, and FTIR (right) of the same films.

5.3.3 XPS – proof of first Fe(II) single valence state with ALD

The main goal of investigating the precursor was to see if the oxidation state of iron could be maintained throughout the deposition. Films deposited with Fe(hfa)$_2$·TMEDA and oxalic acid were investigated with XPS. Many reports on Fe2p XPS only use the position of the Fe2$p_{3/2}$ peak to identify the oxidation state of iron. While the Fe2$p_{3/2}$ peak for FeO is usually expected to be within the 709.6–710.3 eV range, the value is slightly higher for Fe$_2$O$_3$ (710.4–711.6 eV).[154] For Fe$_3$O$_4$ the value is usually somewhere in between (708.1–711.4 eV). In other words, the exact position seems to vary. There are also reports of Fe2$p_{3/2}$ peaks in FeO occurring at binding energy values as high as 718.8 eV.[155] To determine the oxidation state it is necessary to look at the satellite peak related to Fe2$p_{3/2}$. For Fe$_3$O$_4$ there is no satellite, while for FeO the satellite is a shoulder at a binding energy 4.8–6.5 eV higher than the Fe2$p_{3/2}$ peak. For Fe$_2$O$_3$, the splitting is much larger (8.0–8.7 eV).[156, 157] The Fe2$p_{3/2}$ peak position for the samples we investigated was in the 711.9–712.1 eV range, even higher than expected for Fe(III) in Fe$_2$O$_3$. Still, the satellite peak was only at 4.1–4.3 eV higher binding energy, clearly showing

the presence of only Fe(II). This was the case for all the films investigated immediately after deposition, regardless of deposition temperature. Representative scans are shown in Figure 5.25 (left). Given the change in thickness and refractive index over time, aged samples were reinvestigated with XPS. As for the fresh samples, the Fe(II) oxidation state appeared to have been preserved, again, regardless of deposition temperature. The exception was films deposited at 175 and 200 °C where the peak-to-satellite splitting was 8.5 eV, proving that oxidation to Fe(III) had occurred (Figure 5.25, right).
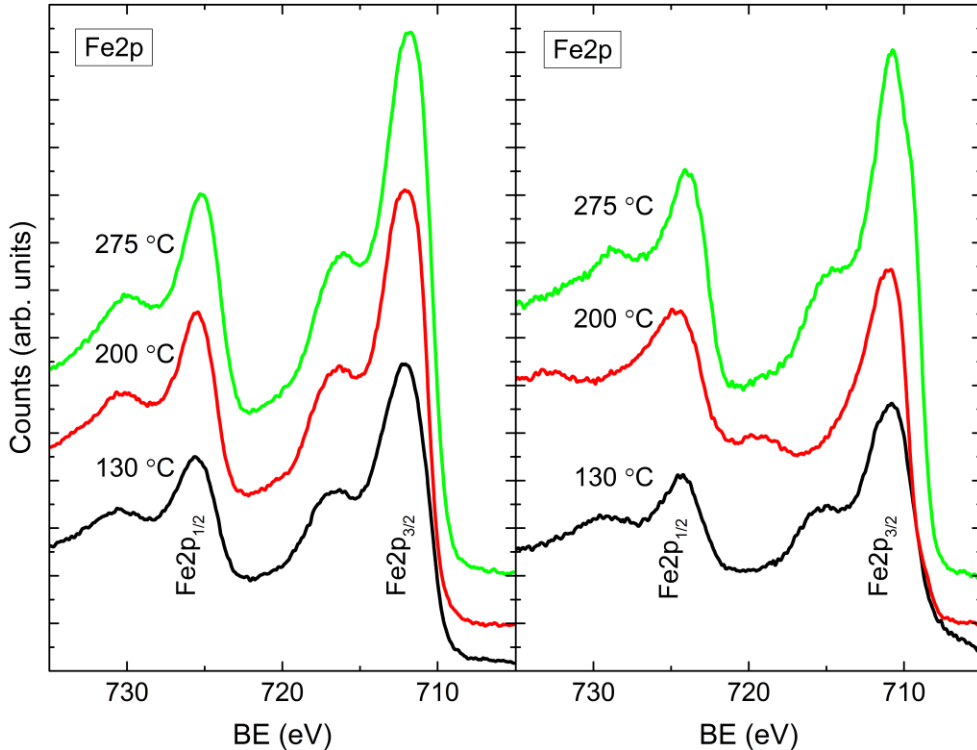
Figure 5.25: Fe2*p* surface XPS of samples at selected deposition temperatures. Measurements were performed immediately after deposition (left), as well as 9 months later (right).

From survey scans, it was apparent that the films also contained nitrogen. Scans of the C1s peak revealed components from both C=O, C–O and C–C bonds (the later most likely from adventitious carbon). Again, an indication of incomplete deposition reactions.

Even though no wide ALD window was found for the Fe(hfa)$_2$·TMEDA/oxalic acid system, the process was indeed shown to be self-limiting. However, the exact composition was hard to establish. Neither XRD nor GIXRD revealed any proper crystallinity. From XPS survey scans, it was clear that residual nitrogen was present in the films, and FTIR also showed species probably originating from the precursor. From an oxide point of view, this is obviously far from ideal, but it is still the first example of direct deposition of only Fe(II) with ALD.

5.4 Multilayers of Fe(II) and TiO₂

The original aim of this thesis was to make multilayers of Fe_2O_3 and $FeTiO_3$. Encouraged by the preservation of the Fe oxidation state in the Fe(hfa)$_2$·TMEDA/oxalic acid process ("FeOx"), a multilayered combination with TiO_2 was made, with hopes that $FeTiO_3$ would form after post-deposition annealing. Since the FeOx films were known to contain organic residue from the precursor, FeOx layers were intentionally thicker, estimated from the growth rates of the separate processes. Five double layers of FeOx/TiO₂, with nominal thickness 5x(18 nm/10 nm), were deposited on Al_2O_3(001) at 150 °C. The resulting film was annealed at 650 °C for 15 min after deposition, with the intention of decomposing and removing the organic constituents, as well as crystallizing the film to $FeTiO_3$. XRD did indeed reveal reflections that could be attributed to epitaxial $FeTiO_3$ (Figure 5.26), but also a number of other reflections that could not be accounted for in terms of expected phases.
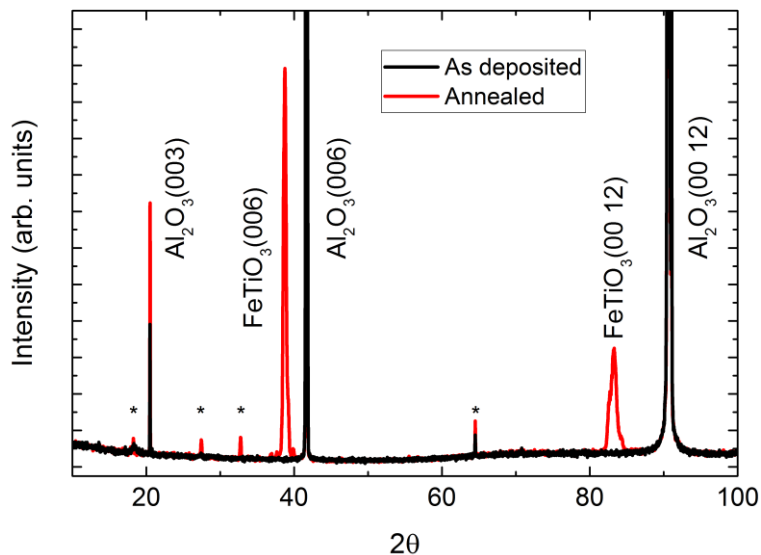

Figure 5.26: $\theta/2\theta$ diffraction of a multilayered mix of "FeOx" and TiO₂ on Al₂O₃ (001), as deposited (black line) and annealed at 650 °C for 15 min (red line). Asterisk indicates reflections from unknown phase(s).

XPS was performed on the annealed sample to determine the oxidation state of Fe. As can be seen in Figure 5.27, the position of the Fe$2p_{2/3}$ peak was located at 711 eV. Again, corresponding well with Fe_2O_3, However, the position was also in correspondence with reports on natural ilmenite.[158, 159] In addition, it was clear that the position of the satellite, at 4.8 eV higher than the Fe$2p_{2/3}$ peak, was in agreement with Fe(II).
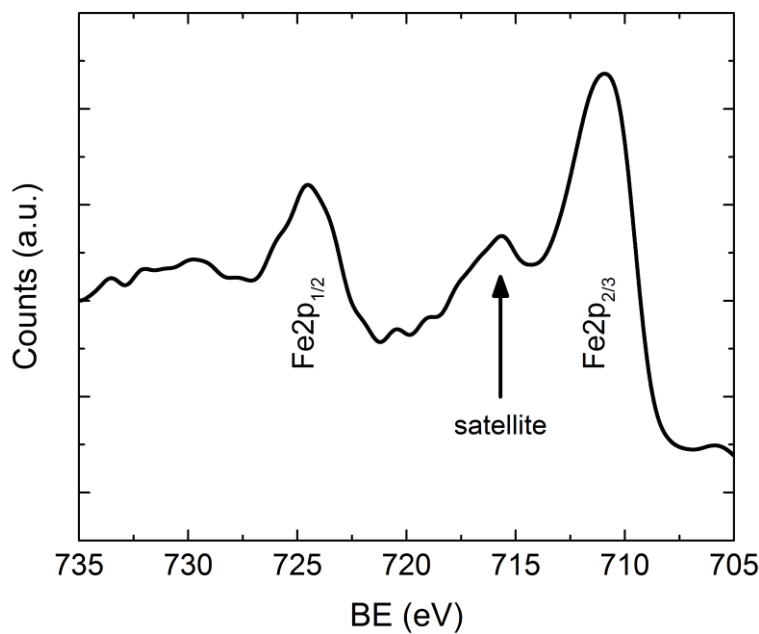
Figure 5.27: Fe2*p* surface XPS of a multilayered film consisting of five "FeOx"/TiO₂ bilayers, annealed at 650 °C for 15 min.

XPS survey scans again revealed the presence of nitrogen, even after annealing. Although no further efforts were made to optimize the process with respect to Fe:Ti composition or removal of precursor residues, this might still be feasible. The present case represent an alternative route to obtaining complex oxides by ALD, even though it might not be suitable for making multilayers with Fe_2O_3.

6   Perspectives

This thesis was aimed at making a model system for multilayered magnetic structures, by combining antiferromagnetic materials. Controlling the fabrication of these synthetic systems is difficult, but if successful, it could enable the realization of novel spintronics devices. Spintronics is an abstract concept for most people, as there is no macroscopic analogy for the spin-component of fundamental particles. However, with spin comes magnetism, and magnetic materials have intrigued humankind since ancient times. As the understanding of magnetism evolved, so did the use of magnets, from compasses to electric motors. By the early 1900's, scientists had begun developing theories for the known magnetic effects at the time, i.e. diamagnetism, paramagnetism and ferromagnetism. Louis Néel first described ferri- and antiferromagnetism in 1936, separating them from ferro- and diamagnetism. As ferromagnets (and ferrimagnets) have a permanent magnetic moment, their properties had been utilized for hundreds of years. Antiferromagnets on the other hand, were first presumed to be useless. Even Néel himself thought little of his own discovery, stating in his Nobel lecture of 1970: "They are extremely interesting from the theoretical standpoint, but do not appear to have any practical applications."[160]

We now know that the grim predictions of Néel was completely wrong: antiferromagnets became an essential part of the computer industry by the 2000's. Recently, antiferromagnetism has gained more attention, as unrealized ideas and future inventions seek to take advantage of the inherent properties of antiferromagnets. How did this type of material go from having no practical application, to being at the forefront of research?

The development of quantum mechanics revolutionized the understanding of magnetic materials, and together with better tools for characterization and fabrication, the 20th century saw a surge in the utilization of advanced magnetic properties. This is especially true within magnetic data storage. Still an important part of computers, magnetic data storage—like all data storage—involves writing and reading. The read/write heads are a particularly advanced technology, as discussed in chapter 1.2. While the role of antiferromagnets in the earlier read/write heads were rather passive, newer concepts have been proposed, utilizing antiferromagnetism in a more integrated way. One example is the "racetrack memory" concept, which stores digital data in magnetic domain walls of "synthetic antiferromagnets".[161-163] The interest in antiferromagnets for spintronics purposes has increased in recent years, as they possess advantageous properties, compared to ferro- and ferrimagnets.[164, 165] They are robust against perturbation, no stray fields are produced and they are capable of ultrafast spin dynamics. Learning how to manipulate the properties of antiferromagnets will undoubtedly result in a new paradigm for electronic devices.[166]

Today, the depth of knowledge within the field of magnetism is so advanced that some aspects seem more like fiction than reality. One example of this is skyrmions.[167] A quasiparticle, skyrmions are small domains in a magnetically ordered matrix, within which the direction of the magnetic moments swirl around until reversed relative to the matrix. These magnetic knots, or vortices, are essentially domain walls confined to areas as small as 1 nm. They are topologically stable and can be moved around in the matrix by e.g. low currents. This makes them prime candidates for use in racetrack memory devices. The concept of skyrmions were originally proposed as a theoretical model in subatomic physics,[168] and the first experimental observation of magnetic skyrmions were made in 2009, but only below 30 K.[169] Later, stable skyrmions have also been observed at room temperature.[170, 171] There are actually three different kinds of skyrmions found in ferromagnets: Bloch, Néel and antiskyrmions. Bloch and Néel skyrmions (Figure 6.1) suffer from the skyrmion Hall effect, making them diverge from a straight path when manipulated by currents. Antiskyrmions are not subject to this effect, and can thus be implemented in applications more easily. This is also true for a possible fourth type of skyrmion, being proposed to exist in antiferromagnets: the antiferromagnetic skyrmion.[172] Though only theoretically predicted, the antiferromagnetic skyrmion should behave like the antiskyrmions, but with the added benefits of being situated in an antiferromagnetic matrix.
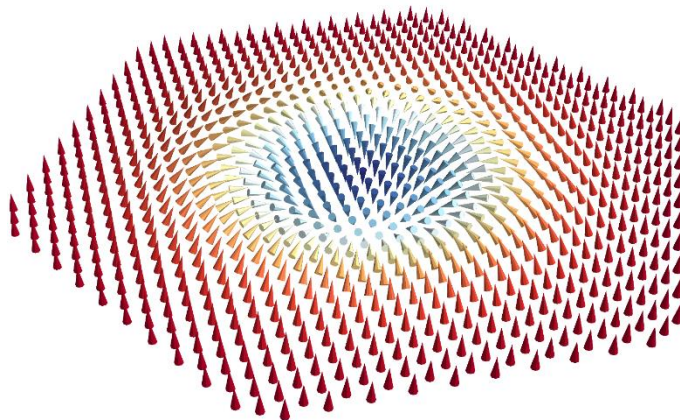

Figure 6.1: Illustration of a Néel type skyrmion. Adapted with permission from Nature Communications,[173] under a Creative Commons Attribution 4.0 international license.

Can ALD be of use to realize the structures needed to create these devices? Probably. ALD grown thin films have found use as electrically insulating layers in microelectronics, for instance in tunnel magnetoresistance (TMR) read heads,[174] and as high-κ dielectrics in transistors.[175] The implementation of ALD is usually limited to binary oxides, but with the complexity and range of elements and compositions that comprise the ALD toolbox today, it seems like ALD is under-exploited and under-appreciated as a thin film technique. This is especially true for complex oxides, as there is no theoretical limit to how many elements can be deposited, given the

existence of compatible processes. Complex oxide ALD is still an advancing field, and has an untapped potential. This is exemplified by recent reports demonstrating excellent phase control in thin films of layered cuprates, as well as the first ALD grown complex oxide superconductor.[176, 177] ALD has indeed also been proposed as a candidate for fabricating 3D racetrack memory devices, utilizing the unique ability of conformal coating of deep trenches.[161]

Admittedly, skyrmions were not considered when this project was begun. Our focus was on creation of artificial ferrimagnetic structures from antiferromagnets. It is exiting to learn that the once considered dull antiferromagnets are in the vanguard of research on functional materials, and have further areas of exciting applications. Antiferromagnets can be produced by numerous techniques, where ALD is one of them. Throughout this work, we have shown how ALD can be used to produce high quality interfaces towards matched substrates at low temperatures, as well as multilayered structures. These properties are advantageous when exploring new exotic magnetic properties. Whether the materials in this work will have a place in future applications is though highly uncertain.

66

7   Concluding remarks

Even though artificial Modum rocks were not obtained through the work presented here, other achievements have been made. Controlled deposition of $NiTiO_3$ by ALD has been shown for the first time. The observed ALD window should be compatible with a range of other processes, enabling more complex oxides or multilayers. On Si(100) substrates, the orientation of the films were (001), while epitaxial $NiTiO_3$(101) was obtained on various other single crystal substrates. In general, choice of right substrate is always important, whether it is to obtain a desired orientation or to match other parts of an industrial production process. For ALD, a careful selection of substrates has previously been shown to enable deposition of metastable phases or polymorphs. This was also shown here. On Al_2O_3(001), epitaxial $NiTiO_3$(001) was obtained as deposited. Curiously, the film revealed a disordered $R-3c$ symmetry, otherwise only encountered at temperatures above 1300 °C. After annealing at 650 °C for 15 min, parts of the film ordered into the $R-3$ symmetry. Improving the annealing parameters might result in ordering throughout the film.

With the good crystallinity and suitable orientation of the $NiTiO_3$ films, multilayers with Fe_2O_3 were produced for magnetic characterization. The idea was that $NiTiO_3$ could act as a substitute for $FeTiO_3$, creating a model system for better understanding of lamellar magnetism. The lack of experience in measuring thin films with PPMS soon became obvious. Samples had to be remeasured due to different measuring schemes (e.g. measuring on heating vs. on cooling and different field history for M(H) curves), and absent features well-known from bulk samples led to uncertainty when analyzing the data. A lot of work was put into the interpretation of the data, which also displayed puzzling features at low temperatures. In the end, irrefutable evidence for the presence of exchange bias could not be found. Some of the observed peculiarities might be linked to measuring effects, while others probably were superpositions of different magnetic contributions. To maintain the layered structure and avoid formation of undesirable phases, the samples were not annealed. This might have complicated the magnetic measurements, as $NiTiO_3$ was found to be disordered as deposited.

The precursor $Fe(hfa)_2 \cdot TMEDA$, new to ALD, was also tested. Self-limiting growth was obtained in combination with oxalic acid. The produced films were the first ever direct deposition of pure Fe(II) with ALD. However, undesired fragments from the precursor were transferred to the film, as shown by FTIR and XPS investigations. Further work is needed to obtain oxides with Fe(II), without contaminants. The process shown here serves as a good example that it is possible, and that such films are probably obtainable through careful selection of precursors and co-reactants. For instance, films of both Fe_2O_3 and Fe_3O_4 have already been deposited from the same Fe

precursor (bis(2,4-methylpentadienyl)iron, $Fe(2,4-C_7H_{11})_2$), simply by changing the co-reactant from O_3 to H_2O_2.[83] There are surely precursors that have not been utilized in ALD yet, and by continuing the search for new processes, some day we will perhaps see the direct deposition of FeO, and in turn $FeTiO_3$.

As an alternative route to obtain $FeTiO_3$, the hybrid Fe(II) films were deposited in a multilayered combination with TiO_2, and subsequently annealed to remove organic residues and crystallize the film. By no means perfect, the process was still partially successful: XPS confirmed that only Fe(II) was present and XRD seemed to show that epitaxial $FeTiO_3$ on $Al_2O_3(001)$ had formed.

The work in this thesis followed two paths towards investigating lamellar magnetism. Firstly, a process for deposition of $NiTiO_3$ by ALD was developed. This process was used to make multilayered samples together with Fe_2O_3, in an attempt to construct a model system to mimic nanolayered natural minerals of $FeTiO_3$ and Fe_2O_3. In addition, a process for deposition of Fe(II) containing films was also developed, and used to produce multilayered samples with TiO_2. When annealed, these multilayered structures led to the formation of $FeTiO_3$, one of the constituents in the natural minerals. A graphical overview of the processes in this thesis is given in Figure 7.1.
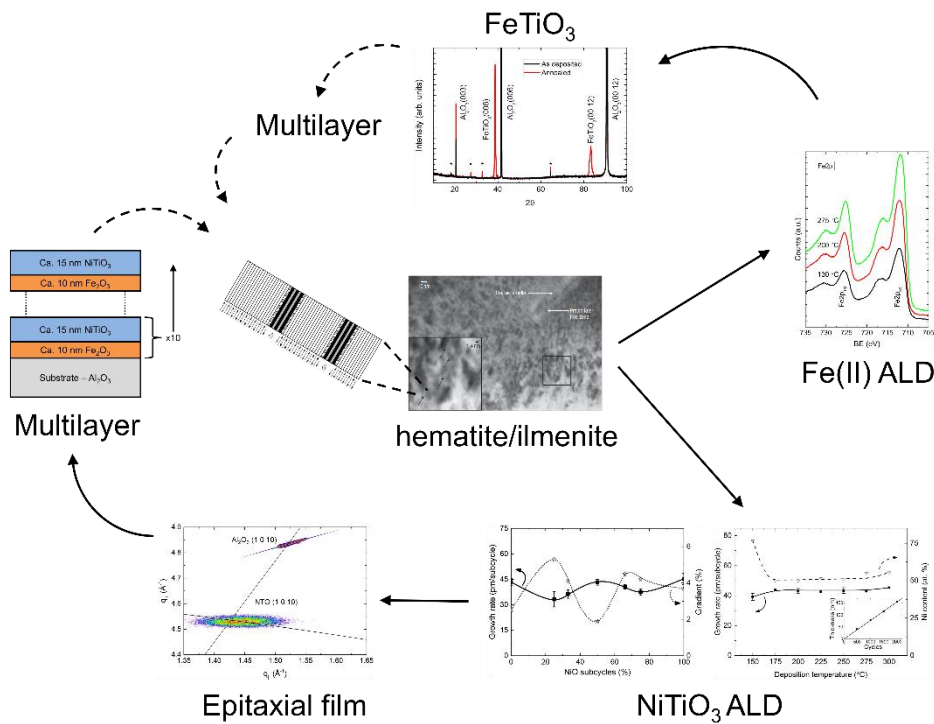

Figure 7.1: A graphical overview showing the processes in this thesis, starting with inspiration from the natural hematite/ilmenite minerals in the middle. The clockwise path explores the development of $NiTiO_3$ as a replacement for $FeTiO_3$. The counterclockwise path explores the direct deposition of Fe(II).

8 References

[1]   S. A. McEnroe, B. Carter-Stiglitz, R. J. Harrison, P. Robinson, K. Fabian and C. McCammon, *Magnetic exchange bias of more than 1 Tesla in a natural mineral intergrowth*, Nat. Nanotechnol., **2**, 10 (2007).

[2]   K. Fabian, S. A. McEnroe, P. Robinson and V. P. Shcherbakov, *Exchange bias identifies lamellar magnetism as the origin of the natural remanent magnetization in titanohematite with ilmenite exsolution from Modum, Norway*, Earth and Planetary Science Letters, **268**, 3-4 (2008).

[3]   P. Robinson, R. J. Harrison, S. A. McEnroe and R. B. Hargraves, *Lamellar magnetism in the haematite-ilmenite series as an explanation for strong remanent magnetization*, Nature, **418**, 6897 (2002).

[4]   T. Kasama, S. A. McEnroe, N. Ozaki, T. Kogure and A. Putnis, *Effects of nanoscale exsolution in hematite–ilmenite on the acquisition of stable natural remanent magnetization*, Earth and Planetary Science Letters, **224**, 3-4 (2004).

[5]   R. Harrison, S. McEnroe, P. Robinson, B. Carter-Stiglitz, E. Palin and T. Kasama, *Low-temperature exchange coupling between Fe_2O_3 and $FeTiO_3$: Insight into the mechanism of giant exchange bias in a natural nanoscale intergrowth*, Physical Review B, **76**, 17 (2007).

[6]   W. H. Meiklejohn and C. P. Bean, *New Magnetic Anisotropy*, Physical Review, **102**, 5 (1956).

[7]   W. H. Meiklejohn and C. P. Bean, *New Magnetic Anisotropy*, Physical Review, **105**, 3 (1957).

[8]   W. H. Meiklejohn, *Exchange Anisotropy—A Review*, Journal of Applied Physics, **33**, 3 (1962).

[9]   J. Nogues and I. K. Schuller, *Exchange bias*, Journal of Magnetism and Magnetic Materials, **192**, 2 (1999).

[10]   J. Nogués, J. Sort, V. Langlais, V. Skumryev, S. Suriñach, J. S. Muñoz and M. D. Baró, *Exchange bias in nanostructures*, Physics Reports, **422**, 3 (2005).

[11]   S. Giri, M. Patra and S. Majumdar, *Exchange bias effect in alloys and compounds*, J Phys Condens Matter, **23**, 7 (2011).

[12]   S. K. Giri and T. K. Nath, *Exchange Bias Effect in Nanostructured Magnetic Oxides*, Journal of Nanoscience and Nanotechnology, **14**, 2 (2014).

[13]   J. Sort, J. Nogués, X. Amils, S. Suriñach, J. S. Muñoz and M. D. Baró, *Room-temperature coercivity enhancement in mechanically alloyed antiferromagnetic-ferromagnetic powders*, Applied Physics Letters, **75**, 20 (1999).

[14]   J. Sort, J. Nogués, X. Amils, S. Suriñach, J. S. Muñoz and M. D. Baró, *Room temperature magnetic hardening in mechanically milled ferromagnetic–antiferromagnetic composites*, Journal of Magnetism and Magnetic Materials, **219**, 1 (2000).

[15]   J. Sort, S. Suriñach, J. S. Muñoz, M. D. Baró, J. Nogués, G. Chouteau, V. Skumryev and G. C. Hadjipanayis, *Improving the energy product of hard magnetic materials*, Physical Review B, **65**, 17 (2002).

[16]   V. Skumryev, S. Stoyanov, Y. Zhang, G. Hadjipanayis, D. Givord and J. Nogués, *Beating the superparamagnetic limit with exchange bias*, Nature, **423**, 6942 (2003).

[17]   J. Eisenmenger and I. K. Schuller, *Magnetic nanostructures: Overcoming thermal fluctuations*, Nature materials, **2**, 7 (2003).

[18]   R. Hunt, *A Magnetoresistive Readout Transducer*, IEEE Transactions on Magnetics, **7**, 1 (1971).

[19]   T. Lin, C. Tsang, R. E. Fontana and J. K. Howard, *Exchange-Coupled Ni-Fe/Fe-Mn, Ni-Fe/Ni-Mn and NiO/Ni-Fe Films for Stabilization of Magnetoresistive Sensors*, IEEE Transactions on Magnetics, **31**, 6 (1995).

[20]   T. Ching, L. Tsann, S. MacDonald, M. Pinarbasi, N. Robertson, H. Santini, M. Doerner, T. Reith, V. Lang, T. Diola and P. Arnett, *5 Gb/in² Recording Demonstration with Conventional AMR Dual Element Heads & Thin Film Disks*, IEEE Transactions on Magnetics, **33**, 5 (1997).

[21]   M. N. Baibich, J. M. Broto, A. Fert, F. Nguyen Van Dau, F. Petroff, P. Etienne, G. Creuzet, A. Friederich and J. Chazelas, *Giant Magnetoresistance of (001)Fe/(001)Cr Magnetic Superlattices*, Physical Review Letters, **61**, 21 (1988).

[22]   G. Binasch, P. Grünberg, F. Saurenbach and W. Zinn, *Enhanced magnetoresistance in layered magnetic structures with antiferromagnetic interlayer exchange*, Physical Review B, **39**, 7 (1989).

[23]   J. L. Leal, L. M. Rodrigues, A. T. Sousa and P. P. Freitas, *Narrow trackwidth TbCo-biased magnetoresistive spin-valve sensors*, Journal of Magnetism and Magnetic Materials, **140**, (1995).

[24]   R. W. Cross, Y. K. Kim, J. O. Oti and S. E. Russek, *Magnetostatic effects in giant magnetoresistive spin- valve devices*, Applied Physics Letters, **69**, 25 (1996).

[25]   B. Dieny, V. S. Speriosu, S. S. P. Parkin, B. A. Gurney, D. R. Wilhoit and D. Mauri, *Giant magnetoresistive in soft ferromagnetic multilayers*, Physical Review B, **43**, 1 (1991).

[26]   D. E. Heim, R. E. Fontana, C. Tsang, V. S. Speriosu, B. A. Gurney and M. L. Williams, *Design and operation of spin valve sensors*, IEEE Transactions on Magnetics, **30**, 2 (1994).

[27]   T. Lin, D. Mauri and Y. Luo, *A Ni-Mn spin valve for high density recording*, IEEE Transactions on Magnetics, **36**, 5 (2000).

[28]   H. C. Tong, X. Shi, F. Liu, C. Qian, Z. W. Dong, X. Yan, R. Barr, L. Miloslavsky, S. Zhou, J. Perlas, P. Prabhu, M. Mao, S. Funada, M. Gibbons, Q. Leng, J. G. Zhu and S. Dey, *Greater Than 14 Gb/in² Spin Valve Heads*, IEEE Transactions on Magnetics, **35**, 5 (1999).

[29]   Z. Zhengyong, F. Yong Chang, T. Clinton, G. Badran, Y. Nan-Hsiung, G. Tarnopolsky, E. Girt, M. Munteanu, S. Harkness, H. Richter, T. Nolan, R. Ranjan, S. Hwang, G. Rauch, M. Ghaly, D. Larson, E. Singleton, V. Vas'ko, J. Ho, F. Stageberg, K. Vee, K. Duxstad and S. Slade, *Magnetic Recording Demonstration Over 100 Gb/in²*, IEEE Transactions on Magnetics, **38**, 5 (2002).

[30]   K. Stoev, F. Liu, Y. Chen, X. Dang, P. Luo, J. Chen, J. Wang, K. Kung, M. Lederman, M. Re, G. Choe, J. N. Zhou and M. Yu, *Demonstration and characterization of 130 Gb/in² magnetic recording systems*, Journal of Applied Physics, **93**, 10 (2003).

[31]   L. Varga, A. Tanaka, K. Nagasaka and R. Kondo, *High frequency permeability of patterned spin valve type thin films*, Journal of Applied Physics, **85**, 8 (1999).

[32]   M. Julliere, *Tunneling between ferromagnetic films*, Physics Letters A, **54**, 3 (1975).

[33]   T. Miyazaki and N. Tezuka, *Giant magnetic tunneling effect in Fe/Al₂O₃/Fe junction*, Journal of Magnetism and Magnetic Materials, **139**, 3 (1995).

[34]   J. S. Moodera, L. R. Kinder, T. M. Wong and R. Meservey, *Large Magnetoresistance at Room Temperature in Ferromagnetic Thin Film Tunnel Junctions*, Physical Review Letters, **74**, 16 (1995).

[35]   Y. Liu, Z. Zhang, Z. Zhang, P. P. Freitas and J. L. Martins, *Micromagnetic simulation for tunnel junctions with synthetic antiferromagnetic pinned layers annealed at different external fields*, Journal of Applied Physics, **91**, 10 (2002).

[36]   S. S. P. Parkin, K. P. Roche, M. G. Samant, P. M. Rice, R. B. Beyers, R. E. Scheuerlein, E. J. O'Sullivan, S. L. Brown, J. Bucchigano, D. W. Abraham, Y. Lu, M. Rooks, P. L. Trouilloud, R. A. Wanner and W. J. Gallagher, *Exchange-biased magnetic tunnel junctions and application to nonvolatile magnetic random access memory (invited)*, Journal of Applied Physics, **85**, 8 (1999).

[37]   S. Parkin, J. Xin, C. Kaiser, A. Panchula, K. Roche and M. Samant, *Magnetically Engineered Spintronic Sensors and Memory*, Proceedings of the IEEE, **91**, 5 (2003).

[38]   S. Tehrani, J. M. Slaughter, M. Deherrera, B. N. Engel, N. D. Rizzo, J. Salter, M. Durlam, R. W. Dave, J. Janesky, B. Butcher, K. Smith and G. Grynkewich, *Magnetoresistive Random Access Memory Using Magnetic Tunnel Junctions*, Proceedings of the IEEE, **91**, 5 (2003).

[39]   J.-G. Zhu and C. Park, *Magnetic tunnel junctions*, Materials Today, **9**, 11 (2006).

[40]   A. Makarov, T. Windbacher, V. Sverdlov and S. Selberherr, *CMOS-compatible spintronic devices: a review*, Semiconductor Science and Technology, **31**, 11 (2016).

[41]   Y. Ishikawa and S.-i. Akimoto, *Magnetic Properties of the FeTiO₃-Fe₂O₃ Solid Solution Series*, Journal of The Physical Society of Japan, **12**, (1957).

[42] Y. Ishikawa and S.-i. Akimoto, *Magnetic Property and Crystal Chemistry of Ilmenite (MeTiO$_3$) and Hematite (αFe$_2$O$_3$) System II. Magnetic Property*, Journal of The Physical Society of Japan, **13**, (1958).

[43] Y. Ishikawa and Y. Shono, *Order-Disorder Transformation and Reverse Thermo-Remanent Magnetism in the FeTiO$_3$-Fe$_2$O$_3$ System*, J. Phys. Chem. Solids, **24**, (1963).

[44] Y. Ishikawa, N. Saito, M. Arai, Y. Watanabe and H. Takei, *A New Oxide Spin Glass System of (1–x)FeTiO$_3$–xFe$_2$O$_3$. I. Magnetic Properties*, Journal of the Physical Society of Japan, **54**, 1 (1985).

[45] C. A. Lawson, G. L. Nord, Jr. and D. E. Champion, *Fe-Ti oxide mineralogy and the origin of normal and reverse remanent magnetization in dacitic pumice blocks from Mt. Shasta, California*, Phys. Earth Planet. Inter., **46**, 1–3 (1987).

[46] G. L. Nord, Jr. and C. A. Lawson, *Order-disorder transition-induced twin domains and magnetic properties in ilmenite-hematite*, Am. Mineral., **74**, 1-2 (1989).

[47] G. L. Nord, Jr. and C. A. Lawson, *Magnetic Properties of Ilmenite$_{70}$-Hematite$_{30}$: Effect of Transformation-Induced Twin Boundaries*, Journal of Geophysical Research, **97**, B7 (1992).

[48] K. Fabian, N. Miyajima, P. Robinson, S. A. McEnroe, T. B. Ballaran and B. P. Burton, *Chemical and magnetic properties of rapidly cooled metastable ferri-ilmenite solid solutions: implications for magnetic self-reversal and exchange bias—I. Fe-Ti order transition in quenched synthetic ilmenite 61*, Geophysical Journal International, **186**, 3 (2011).

[49] P. Robinson, R. J. Harrison, N. Miyajima, S. A. McEnroe and K. Fabian, *Chemical and magnetic properties of rapidly cooled metastable ferri-ilmenite solid solutions: implications for magnetic self-reversal and exchange bias—II. Chemical changes during quench and annealing*, Geophysical Journal International, **188**, 2 (2012).

[50] P. Robinson, R. J. Harrison, K. Fabian and S. A. McEnroe, *Chemical and magnetic properties of rapidly cooled metastable ferri-ilmenite solid solutions: implications for magnetic self-reversal and exchange bias—III. Magnetic interactions in samples produced by Fe-Ti ordering*, Geophysical Journal International, **191**, 3 (2012).

[51] P. Robinson, S. A. McEnroe, K. Fabian, R. J. Harrison, C. I. Thomas and H. Mukai, *Chemical and magnetic properties of rapidly cooled metastable ferri-ilmenite solid solutions – IV: the fine structure of self-reversed thermoremanent magnetization*, Geophysical Journal International, **196**, 3 (2014).

[52] F. Zhou, S. Kotru and R. K. Pandey, *Pulsed laser-deposited ilmenite–hematite films for application in high-temperature electronics*, Thin Solid Films, **408**, 1 (2002).

[53] P. Kale, P. Padmini, J. Dou, L. Navarrete, M. Shamsuzzoha, R. Schad and R. K. Pandey, *Growth and Characterization of Pulsed-Laser-Deposited Ilmenite–Hematite Thin Films*, Journal of Electronic Materials, **36**, 9 (2007).

[54] J. Dou, L. Navarrete, R. Schad, P. Padmini, R. K. Pandey, H. Guo and A. Gupta, *Magnetic properties of ilmenite-hematite films and bulk samples*, Journal of Applied Physics, **103**, 7 (2008).

[55] K. Rode, R. D. Gunning, R. G. S. Sofin, M. Venkatesan, J. G. Lunney, J. M. D. Coey and I. V. Shvets, *Magnetic anisotropy in ilmenite–hematite solid solution thin films grown by pulsed laser ablation*, Journal of Magnetism and Magnetic Materials, **320**, 23 (2008).

[56] L. Bocher, E. Popova, M. Nolan, A. Gloter, E. Chikoidze, K. March, B. Warot-Fonrose, B. Berini, O. Stéphan, N. Keller and Y. Dumont, *Direct Evidence of Fe^{2+}-Fe^{3+} Charge Ordering in the Ferrimagnetic Hematite-Ilmenite $Fe_{1.35}Ti_{0.65}O_{3-\delta}$ Thin Films*, Physical Review Letters, **111**, 16 (2013).

[57] H. Hojo, K. Fujita, H. Ikeno, T. Matoba, T. Mizoguchi, I. Tanaka, T. Nakamura, Y. Takeda, T. Okane and K. Tanaka, *Magnetic structures of $FeTiO_3$-Fe_2O_3 solid solution thin films studied by soft X-ray magnetic circular dichroism and ab initio multiplet calculations*, Applied Physics Letters, **104**, 11 (2014).

[58] Y. Takada, M. Nakanishi, T. Fujii and J. Takada, *Preparation and characterization of (001)- and (110)-oriented $0.6FeTiO_3 \cdot 0.4Fe_2O_3$ films for room temperature magnetic semiconductors*, Applied Physics Letters, **92**, 25 (2008).

[59] G. Subramanyam, M. W. Cole, N. X. Sun, T. S. Kalkur, N. M. Sbrockey, G. S. Tompa, X. Guo, C. Chen, S. P. Alpay, G. A. Rossetti, K. Dayal, L.-Q. Chen and D. G. Schlom, *Challenges and opportunities for multi-functional oxide thin films for voltage tunable radio frequency/microwave components*, Journal of Applied Physics, **114**, 19 (2013).

[60] P. Kuppusami and V. S. Raghunathan, *Status of pulsed laser deposition: challenges and opportunities*, Surface Engineering, **22**, 2 (2013).

[61] R. F. C. Farrow, ed., *Molecular Beam Epitaxy: Applications to Key Materials*, Noyes Publications, Park Ridge, New Jersey, USA, 1995.

[62] K. Kukli, J. Ihanus, M. Ritala and M. Leskelä, *Tailoring the dielectric properties of HfO_2–Ta_2O_5 nanolaminates*, Applied Physics Letters, **68**, 26 (1996).

[63] A. A. Chaaya, R. Viter, I. Baleviciute, M. Bechelany, A. Ramanavicius, Z. Gertnere, D. Erts, V. Smyntyna and P. Miele, *Tuning Optical Properties of Al_2O_3/ZnO Nanolaminates Synthesized by Atomic Layer Deposition*, The Journal of Physical Chemistry C, **118**, 7 (2014).

[64] J. W. Elam, Z. A. Sechrist and S. M. George, *ZnO/Al_2O_3 nanolaminates fabricated by atomic layer deposition: growth*

and surface roughness measurements, Thin Solid Films, **414**, 1 (2002).

[65] O. M. E. Ylivaara, L. Kilpi, X. Liu, S. Sintonen, S. Ali, M. Laitinen, J. Julin, E. Haimi, T. Sajavaara, H. Lipsanen, S.-P. Hannula, H. Ronkainen and R. L. Puurunen, *Aluminum oxide/titanium dioxide nanolaminates grown by atomic layer deposition: Growth and mechanical properties*, Journal of Vacuum Science & Technology A: Vacuum, Surfaces, and Films, **35**, 1 (2017).

[66] L. H. Kim, K. Kim, S. Park, Y. J. Jeong, H. Kim, D. S. Chung, S. H. Kim and C. E. Park, *Al_2O_3/TiO2 Nanolaminate Thin Film Encapsulation for Organic Thin Film Transistors via Plasma-Enhanced Atomic Layer Deposition*, ACS applied materials & interfaces, **6**, 9 (2014).

[67] S. Zhao, Z. Gao, C. Chen, G. Wang, B. Zhang, Y. Chen, J. Zhang, X. Li and Y. Qin, *Alternate nonmagnetic and magnetic multilayer nanofilms deposited on carbon nanocoils by atomic layer deposition to tune microwave absorption property*, Carbon, **98**, (2016).

[68] P.-A. Hansen, H. Fjellvåg, T. G. Finstad and O. Nilsen, *Luminescent Properties of Multilayered Eu_2O_3 and TiO_2 Grown by Atomic Layer Deposition*, Chemical Vapor Deposition, **20**, 7-8-9 (2014).

[69] J. López, H. A. Borbón-Nuñez, E. G. Lizarraga-Medina, E. Murillo, R. Machorro, N. Nedev, H. Marquez, M. H. Farías, H. Tiznado and G. Soto, *Al_2O_3-Y_2O_3 ultrathin multilayer stacks grown by atomic layer deposition as perspective for optical waveguides applications*, Optical Materials, **72**, (2017).

[70] S. Zarubin, E. Suvorova, M. Spiridonov, D. Negrov, A. Chernikova, A. Markeev and A. Zenkevich, *Fully ALD-grown TiN/$Hf_{0.5}Zr_{0.5}O_2$/TiN stacks: Ferroelectric and structural properties*, Applied Physics Letters, **109**, 19 (2016).

[71] A. Ohtomo and H. Y. Hwang, *A high-mobility electron gas at the $LaAlO_3$/$SrTiO_3$ heterointerface*, Nature, **427**, 6973 (2004).

[72] N. Reyren, S. Thiel, A. D. Caviglia, L. F. Kourkoutis, G. Hammerl, C. Richter, C. W. Schneider, T. Kopp, A.-S. Rüetschi, D. Jaccard, M. Gabay, D. A. Muller, J.-M. Triscone and J. Mannhart, *Superconducting Interfaces Between Insulating Oxides*, Science, **317**, 5842 (2007).

[73] D. F. Li, Y. Wang and J. Y. Dai, *Tunable electronic transport properties of $DyScO_3$/$SrTiO_3$ polar heterointerface*, Applied Physics Letters, **98**, 12 (2011).

[74] H. Seim, H. Mölsä, M. Nieminen, H. Fjellvåg and L. Niinistö, *Deposition of $LaNiO_3$ thin films in an atomic layer epitaxy reactor*, Journal of Materials Chemistry, **7**, 3 (1997).

[75] M. Vehkamäki, T. Hatanpää, T. Hänninen, M. Ritala and M. Leskelä, *Growth of $SrTiO_3$ and $BaTiO_3$ Thin Films by Atomic Layer Deposition*, Electrochemical and Solid-State Letters, **2**, 10 (1999).

[76]   A. R. Akbashev, G. Chen and J. E. Spanier, *A facile route for producing single-crystalline epitaxial perovskite oxide thin films*, Nano Lett, **14**, 1 (2014).

[77]   M. de Ridder, P. C. van de Ven, R. G. van Welzenis, H. H. Brongersma, S. Helfensteyn, C. Creemers, P. Van Der Voort, M. Baltes, M. Mathieu and E. F. Vansant, *Growth of iron oxide on yttria-stabilized zirconia by atomic layer deposition*, J. Phys. Chem. B, **106**, 51 (2002).

[78]   J. Bachmann, J. Jing, M. Knez, S. Barth, H. Shen, S. Mathur, U. Gösele and K. Nielsch, *Ordered iron oxide nanotube arrays of controlled geometry and tunable magnetism by atomic layer deposition*, J. Am. Chem. Soc., **129**, 31 (2007).

[79]   M. Aronniemi, J. Saino and J. Lahtinen, *Characterization and gas-sensing behavior of an iron oxide thin film prepared by atomic layer deposition*, Thin Solid Films, **516**, 18 (2008).

[80]   M. Rooth, A. Johansson, K. Kukli, J. Aarik, M. Boman and A. Hårsta, *Atomic Layer Deposition of Iron Oxide Thin Films and Nanotubes using Ferrocene and Oxygen as Precursors*, Chemical Vapor Deposition, **14**, 3-4 (2008).

[81]   B. M. Klahr, A. B. Martinson and T. W. Hamann, *Photoelectrochemical investigation of ultrathin film iron oxide solar cells prepared by atomic layer deposition*, Langmuir : the ACS journal of surfaces and colloids, **27**, 1 (2011).

[82]   K. Kukli, M. C. Dimri, A. Tamm, M. Kemell, T. Käämbre, M. Vehkamäki, M. Puttaswamy, R. Stern, I. Kuusik, A. Kikas, M. Tallarida, D. Schmeisser, M. Ritala and M. Leskelä, *Structural and Magnetic Studies on Iron Oxide and Iron-Magnesium Oxide Thin Films Deposited Using Ferrocene and (Dimethylaminomethyl)ferrocene Precursors*, ECS Journal of Solid State Science and Technology, **2**, 3 (2013).

[83]   S. C. Riha, J. M. Racowski, M. P. Lanci, J. A. Klug, A. S. Hock and A. B. Martinson, *Phase discrimination through oxidant selection in low-temperature atomic layer deposition of crystalline iron oxides*, Langmuir : the ACS journal of surfaces and colloids, **29**, 10 (2013).

[84]   O. Nilsen, M. Lie, S. Foss, H. Fjellvåg and A. Kjekshus, *Effect of magnetic field on the growth of α-Fe$_2$O$_3$ thin films by atomic layer deposition*, Applied Surface Science, **227**, 1-4 (2004).

[85]   M. Lie, H. Fjellvåg and A. Kjekshus, *Growth of Fe$_2$O$_3$ thin films by atomic layer deposition*, Thin Solid Films, **488**, 1-2 (2005).

[86]   O. Nilsen, H. Fjellvåg and A. Kjekshus, *Growth of manganese oxide thin films by atomic layer deposition*, Thin Solid Films, **444**, 1-2 (2003).

[87]   A. Tamm, M. C. Dimri, J. Kozlova, A. Aidla, T. Tätte, T. Arroval, U. Mäeorg, H. Mändar, R. Stern and K. Kukli, *Atomic layer deposition of ferromagnetic iron oxide films on three-dimensional substrates with tin oxide nanoparticles*, Journal of Crystal Growth, **343**, 1 (2012).

[88]   Y. Zhang, M. Liu, Y. Zhang, X. Chen, W. Ren and Z.-G. Ye, *Atomic layer deposition of superparamagnetic and*

ferrimagnetic magnetite thin films, Journal of Applied Physics, **117**, 17 (2015).

[89] Y. Zhang, M. Liu, L. Zhang, Z. Zhou, B. Peng, C. Wang, Q. Lin, Z.-D. Jiang, W. Ren and Z.-G. Ye, *Multiferroic heterostructures of Fe$_3$O$_4$/PMN-PT prepared by atomic layer deposition for enhanced interfacial magnetoelectric couplings*, Applied Physics Letters, **110**, 8 (2017).

[90] G. Carraro, D. Peeters, A. Gasparotto, C. Maccato, E. Bontempi and D. Barreca, *Fe$_2$O$_3$ nanostructures on SrTiO$_3$(1 1 1) by chemical vapor deposition: Growth and characterization*, Materials Letters, **136**, (2014).

[91] G. Carraro, C. Maccato, A. Gasparotto, T. Montini, S. Turner, O. I. Lebedev, V. Gombac, G. Adami, G. Van Tendeloo, D. Barreca and P. Fornasiero, *Enhanced Hydrogen Production by Photoreforming of Renewable Oxygenates Through Nanostructured Fe$_2$O$_3$ Polymorphs*, Advanced Functional Materials, **24**, 3 (2014).

[92] G. Carraro, D. Barreca, C. Maccato, E. Bontempi, L. E. Depero, C. de Julián Fernández and A. Caneschi, *Supported ε and β iron oxide nanomaterials by chemical vapor deposition: structure, morphology and magnetic properties*, CrystEngComm, **15**, 6 (2013).

[93] G. Carraro, A. Gasparotto, C. Maccato, E. Bontempi, O. I. Lebedev, S. Turner, C. Sada, L. E. Depero, G. Van Tendeloo and D. Barreca, *Fluorine doped Fe$_2$O$_3$ nanostructures by a one-pot plasma-assisted strategy*, RSC Advances, **3**, 45 (2013).

[94] G. Carraro, C. Maccato, E. Bontempi, A. Gasparotto, O. I. Lebedev, S. Turner, L. E. Depero, G. Van Tendeloo and D. Barreca, *Insights on Growth and Nanoscopic Investigation of Uncommon Iron Oxide Polymorphs*, European Journal of Inorganic Chemistry, **2013**, 31 (2013).

[95] D. Barreca, G. Carraro, A. Gasparotto, C. Maccato, R. Seraglia and G. Tabacchi, *An iron(II) diamine diketonate molecular complex: Synthesis, characterization and application in the CVD of Fe$_2$O$_3$ thin films*, Inorganica Chimica Acta, **380**, (2012).

[96] D. Barreca, G. Carraro, A. Devi, E. Fois, A. Gasparotto, R. Seraglia, C. Maccato, C. Sada, G. Tabacchi, E. Tondello, A. Venzo and M. Winter, *β-Fe$_2$O$_3$ nanomaterials from an iron(II) diketonate-diamine complex: a study from molecular precursor to growth process*, Dalton Trans., **41**, 1 (2012).

[97] V. Miikkulainen, M. Leskelä, M. Ritala and R. L. Puurunen, *Crystallinity of inorganic films grown by atomic layer deposition: Overview and general trends*, Journal of Applied Physics, **113**, 2 (2013).

[98] J. E. Bratvold, H. Fjellvåg and O. Nilsen, *Atomic Layer Deposition of oriented nickel titanate (NiTiO$_3$)*, Applied Surface Science, **311**, (2014).

[99] J. E. Greedon, "Magnetic oxides", in *Encyclopedia of inorganic chemistry*, Vol. 4, ed. R. B. King, John Wiley & Sons Ltd., Chichester, West Sussex, England, 1994.

[100] F. J. Morin, *Magnetic Susceptibility of αFe₂O₃ and αFe₂O₃ with Added Titanium*, Physical Review, **78**, 6 (1950).

[101] Ö. Özdemir, D. J. Dunlop and T. S. Berquó, *Morin transition in hematite: Size dependence and thermal hysteresis*, Geochemistry, Geophysics, Geosystems, **9**, 10 (2008).

[102] G. S. Heller, J. J. Stickler, S. Kern and A. Wold, *Antiferromagnetism in NiTiO₃*, Journal of Applied Physics, **34**, 4 (1963).

[103] S. Klemme, W. Hermes, M. Eul, C. H. Wijbrans, A. Rohrbach and R. Pottgen, *New thermodynamic data for CoTiO₃, NiTiO₃ and CoCO₃ based on low-temperature calorimetric measurements*, Chemistry Central journal, **5**, (2011).

[104] G. Shirane, S. J. Pickart and Y. Ishikawa, *Neutron Diffraction Study of Antiferromagnetic MnTiO₃ and NiTiO₃*, Journal of the Physical Society of Japan, **14**, 10 (1959).

[105] Y. Ishikawa and S.-i. Akimoto, *Magnetic Property and Crystal Chemistry of Ilmenite (MeTiO₃) and Hematite (αFe₂O₃) System I. Crystal Chemistry*, Journal of The Physical Society of Japan, **13**, 10 (1958).

[106] G. F. Dionne, *Magnetic Oxides*, Springer, New York, USA, 2009.

[107] S. A. McEnroe, R. J. Harrison, P. Robinson and F. Langenhorst, *Nanoscale hematite-ilmenite lamellae in massive ilmenite rock: an example of 'lamellar magnetism' with implications for planetary magnetic anomalies*, Geophys. J. Int., **151**, 3 (2002).

[108] S. A. McEnroe, R. J. Harrison, P. Robinson, U. Golla and M. J. Jercinovic, *Effect of fine-scale microstructures in titanohematite on the acquisition and stability of natural remanent magnetization in granulite facies metamorphic rocks, southwest Sweden: Implications for crustal magnetism*, Journal of Geophysical Research, **106**, B12 (2001).

[109] P. Robinson, R. J. Harrison, S. A. McEnroe and R. B. Hargraves, *Nature and origin of lamellar magnetism in the hematite-ilmenite series*, Am. Mineral., **89**, 5-6 (2004).

[110] M. Kiwi, *Exchange bias theory*, Journal of Magnetism and Magnetic Materials, **234**, 3 (2001).

[111] K. Chen, D. Lott, F. Radu, F. Choueikani, E. Otero and P. Ohresser, *Observation of an atomic exchange bias effect in DyCo₄ film*, Sci Rep, **5**, (2015).

[112] T. Suntola, in *Handbook of Crystal Growth*, ed. D. T. J. Hurle, Elsevier Science, Amsterdam, Netherlands, 1994, pp. 604-663.

[113] M. Ylilammi, *Monolayer thickness in atomic layer deposition*, Thin Solid Films, **279**, 1–2 (1996).

[114] M. Lie, O. Nilsen, H. Fjellvåg and A. Kjekshus, *Growth of La₁₋ₓSrₓFeO₃ thin films by atomic layer deposition*, Dalton Trans., 3 (2009).

[115] H. H. Sønsteby, O. Nilsen and H. Fjellvåg, *Atomic layer deposition of (K,Na)(Nb,Ta)O₃ thin films*, Journal of Vacuum Science & Technology A: Vacuum, Surfaces, and Films, **34**, 4 (2016).

[116] M. Lie, K. Barnholt Klepper, O. Nilsen, H. Fjellvåg and A. Kjekshus, *Growth of iron cobalt oxides by atomic layer deposition*, Dalton Trans., 2 (2008).

[117] O. Nilsen, E. Rauwel, H. Fjellvåg and A. Kjekshus, *Growth of $La_{1-x}Ca_xMnO_3$ thin films by atomic layer deposition*, Journal of Materials Chemistry, **17**, 15 (2007).

[118] A. Yanguas-Gil, K. E. Peterson and J. W. Elam, *Controlled Dopant Distribution and Higher Doping Efficiencies by Surface-Functionalized Atomic Layer Deposition*, Chemistry of Materials, **23**, 19 (2011).

[119] M. Birkholz, *Thin Film Analysis by X-Ray Scattering*, Wiley-VCH, Weinheim, Germany, 2006.

[120] M. Björck and G. Andersson, *GenX: an extensible X-ray reflectivity refinement program utilizing differential evolution*, Journal of Applied Crystallography, **40**, 6 (2007).

[121] *UniQuant Version 2 User Manual*, Omega Data Systems, Veldhoven, The Netherlands, 1994.

[122] *CompleteEASE Version 4.41*, J. A. Woollam Co. Inc., Lincoln, Nebraska, USA, 2009.

[123] J. Tauc, R. Grigorovici and A. Vancu, *Optical Properties and Electronic Structure of Amorphous Germanium*, Phys. Status Solidi B, **15**, 2 (1966).

[124] D. Nečas and P. Klapetek, *Gwyddion: an open-source software for SPM data analysis*, Open Physics, **10**, 1 (2012).

[125] V. Sammelselg, A. Rosental, A. Tarre, L. Niinistö, K. Heiskanen, K. Ilmonen, L. S. Johansson and T. Uustare, *TiO_2 thin films by atomic layer deposition: a case of uneven growth at low temperature*, Applied Surface Science, **134**, 1–4 (1998).

[126] M. Ritala, M. Leskelä, E. Nykänen, P. Soininen and L. Niinistö, *Growth of titanium dioxide thin films by atomic layer epitaxy*, Thin Solid Films, **225**, 1–2 (1993).

[127] J. Aarik, J. Karlis, H. Mandar, T. Uustare and V. Sammelselg, *Influence of structure development on atomic layer deposition of TiO_2 thin films*, Appl. Surf. Sci., **181**, 3-4 (2001).

[128] A. Tarre, A. Rosental, V. Sammelselg and T. Uustare, *Comparative study of low-temperature chloride atomic-layer chemical vapor deposition of TiO_2 and SnO_2*, Applied Surface Science, **175–176**, (2001).

[129] A. Rahtu and M. Ritala, *Reaction mechanism studies on titanium isopropoxide-water atomic layer deposition process*, Chem. Vap. Deposition, **8**, Copyright (C) 2012 American Chemical Society (ACS). All Rights Reserved. (2002).

[130] J. Aarik, A. Aidla, T. Uustare, M. Ritala and M. Leskelä, *Titanium isopropoxide as a precursor for atomic layer deposition. Characterization of titanium dioxide growth process*, Appl. Surf. Sci., **161**, 3-4 (2000).

[131] R. Matero, A. Rahtu, M. Ritala, M. Leskelä and T. Sajavaara, *Effect of water dose on the atomic layer deposition rate of oxide thin films*, Thin Solid Films, **368**, 1 (2000).

[132] T. S. Yang, W. Cho, M. Kim, K.-S. An, T.-M. Chung, C. G. Kim and Y. Kim, *Atomic layer deposition of nickel oxide films using Ni(dmamp)$_2$ and water*, Journal of Vacuum Science & Technology A: Vacuum, Surfaces, and Films, **23**, 4 (2005).

[133] H. L. Lu, G. Scarel, C. Wiemer, M. Perego, S. Spiga, M. Fanciulli and G. Pavia, *Atomic Layer Deposition of NiO Films on Si(100) Using Cyclopentadienyl-Type Compounds and Ozone as Precursors*, Journal of The Electrochemical Society, **155**, 10 (2008).

[134] P. A. Premkumar, M. Toeller, C. Adelmann, J. Meersschaut, A. Franquet, O. Richard, H. Tielens, B. Brijs, A. Moussa, T. Conard, H. Bender, M. Schaekers, J. A. Kittl, M. Jurczak and S. Van Elshocht, *NiO Thin Films Synthesized by Atomic Layer Deposition using Ni(dmamb)$_2$ and Ozone as Precursors*, Chemical Vapor Deposition, **18**, 1-3 (2012).

[135] E. Lindahl, M. Ottosson and J.-O. Carlsson, *Atomic Layer Deposition of NiO by the Ni(thd)$_2$/H$_2$O Precursor Combination*, Chemical Vapor Deposition, **15**, 7-9 (2009).

[136] M. Utriainen, M. Kröger-Laukkanen and L. Niinistö, *Studies of NiO thin film formation by atomic layer epitaxy*, Mater. Sci. Eng., B, **B54**, 1,2 (1998).

[137] A. Mehta, K. Leinenweber, A. Navrotsky and M. Akaogi, *Calorimetric Study of High Pressure Polymorphism in FeTiO$_3$: Stability of the Perovskite Phase*, Phys. Chem. Miner., **21**, 4 (1994).

[138] L. C. Ming, Y.-H. Kim, T. Uchida, Y. Wang and M. Rivers, *In situ X-ray diffraction study of phase transitions of FeTiO$_3$ at high pressures and temperatures using a large-volume press and synchrotron radiation*, American Mineralogist, **91**, 1 (2006).

[139] T. Varga, T. C. Droubay, M. E. Bowden, P. Nachimuthu, V. Shutthanandan, T. B. Bolin, W. A. Shelton and S. A. Chambers, *Epitaxial growth of NiTiO$_3$ with a distorted ilmenite structure*, Thin Solid Films, **520**, 17 (2012).

[140] T. Varga, T. C. Droubay, M. E. Bowden, R. J. Colby, S. Manandhar, V. Shutthanandan, D. Hu, B. C. Kabius, E. Apra, W. A. Shelton and S. A. Chambers, *Coexistence of weak ferromagnetism and polar lattice distortion in epitaxial NiTiO$_3$ thin films of the LiNbO$_3$-type structure*, Journal of Vacuum Science & Technology B: Microelectronics and Nanometer Structures, **31**, 3 (2013).

[141] T. Varga, T. C. Droubay, M. E. Bowden, S. A. Stephens, S. Manandhar, V. Shutthanandan, R. J. Colby, D. Hu, W. A. Shelton and S. A. Chambers, *Strain-dependence of the structure and ferroic properties of epitaxial Ni$_{1-x}$Ti$_{1-y}$O$_3$ thin films grown on sapphire substrates*, Thin Solid Films, **578**, (2015).

[142] M. Lerch, H. Boysen, R. Neder, F. Frey and W. Laqua, *Neutron scattering investigation of the high temperature phase transition in nickel titanium oxide (NiTiO$_3$)*, J. Phys. Chem. Solids, **53**, 9 (1992).

[143] H. Boysen, F. Frey, M. Lerch and T. Vogt, *A neutron powder investigation of the high-temperature phase transition in NiTiO₃*, Z. Kristallogr., **210**, 5 (1995).

[144] K. T. Jacob, V. S. Saji and S. N. S. Reddy, *Thermodynamic evidence for order–disorder transition in NiTiO₃*, The Journal of Chemical Thermodynamics, **39**, 2 (2007).

[145] R. Salzer, D. Spemann, P. Esquinazi, R. Höhne, A. Setzer, K. Schindler, H. Schmidt and T. Butz, *Possible pitfalls in search of magnetic order in thin films deposited on single crystalline sapphire substrates*, Journal of Magnetism and Magnetic Materials, **317**, 1-2 (2007).

[146] X. Wu, Z. Zhang, Y. Yu and J. Meng, *Background signal from substrates in characterizations of magnetic thin films*, Journal of Magnetism and Magnetic Materials, **346**, (2013).

[147] A. H. Hill, F. Jiao, P. G. Bruce, A. Harrison, W. Kockelmann and C. Ritter, *Neutron diffraction study of mesoporous and bulk hematite, α-Fe₂O₃*, Chem. Mater., **20**, 15 (2008).

[148] I. Dzyaloshinsky, *A Thermodynamic Theory of "Weak" Ferromagnetism of Antiferromagnetics*, Journal of Physics and Chemistry of Solids, **4**, 4 (1958).

[149] P. Robinson, F. Heidelbach, A. M. Hirt, S. A. McEnroe and L. L. Brown, *Crystallographic-magnetic correlations in single-crystal haemo-ilmenite: new evidence for lamellar magnetism*, Geophysical Journal International, **165**, 1 (2006).

[150] R. Höhne, P. Esquinazi, V. Heera and H. Weishart, *Magnetic properties of ion-implanted diamond*, Diamond and Related Materials, **16**, 8 (2007).

[151] N. Keller, M. Guyot, A. Das, M. Porte and R. Krishnan, *Study of the interdiffusion at the interfaces of NiO/αFe₂O₃ multilayers prepared by pulsed laser deposition*, Solid State Communications, **105**, 5 (1998).

[152] A. Hamie, Y. Dumont, E. Popova, J. Scola, A. Fouchet, B. Berini and N. Keller, *Structural, optical, and magnetic properties of the ferromagnetic semiconductor hematite-ilmenite Fe₂₋ₓTiₓO₃₋δ thin films on SrTiO₃(001) prepared by pulsed laser deposition*, Journal of Applied Physics, **108**, 9 (2010).

[153] S. B. Ogale, *Dilute doping, defects, and ferromagnetism in metal oxide systems*, Advanced Materials, **22**, 29 (2010).

[154] NIST X-ray Photoelectron Spectroscopy Database, Version 4.1, National Institute of Standards and Technology, Gaithersburg, (2012), http://srdata.nist.gov/xps/

[155] A. N. Mansour and R. A. Brizzolara, *Characterization of the Surface of FeO Powder by XPS*, Surface Science Spectra, **4**, 4 (1996).

[156] A. P. Grosvenor, B. A. Kobe, M. C. Biesinger and N. S. McIntyre, *Investigation of multiplet splitting of Fe 2p XPS spectra and bonding in iron compounds*, Surface and Interface Analysis, **36**, 12 (2004).

[157] T. Yamashita and P. Hayes, *Analysis of XPS spectra of Fe^{2+} and Fe^{3+} ions in oxide materials*, Applied Surface Science, **254**, 8 (2008).

[158] M. Irannajad, A. Mehdilo and O. Salmani Nuri, *Influence of microwave irradiation on ilmenite flotation behavior in the presence of different gangue minerals*, Separation and Purification Technology, **132**, (2014).

[159] A. Mehdilo, M. Irannajad and B. Rezai, *Chemical and mineralogical composition of ilmenite: Effects on physical and surface properties*, Minerals Engineering, **70**, (2015).

[160] L. Néel, *Magnetism and Local Molecular Field*, Science, **174**, 4013 (1971).

[161] S. Parkin and S.-H. Yang, *Memory on the racetrack*, Nature nanotechnology, **10**, 3 (2015).

[162] S.-H. Yang, K.-S. Ryu and S. Parkin, *Domain-wall velocities of up to 750 m s^{-1} driven by exchange-coupling torque in synthetic antiferromagnets*, Nature nanotechnology, **10**, 3 (2015).

[163] Z. Yu, Y. Zhang, Z. Zhang, M. Cheng, Z. Lu, X. Yang, J. Shi and R. Xiong, *Domain-wall motion at an ultrahigh speed driven by spin-orbit torque in synthetic antiferromagnets*, Nanotechnology, **29**, 17 (2018).

[164] T. Jungwirth, X. Marti, P. Wadley and J. Wunderlich, *Antiferromagnetic spintronics*, Nature nanotechnology, **11**, 3 (2016).

[165] O. Gomonay, T. Jungwirth and J. Sinova, *Concepts of antiferromagnetic spintronics*, Physica Status Solidi RRL, **11**, 4 (2017).

[166] C. Song, Y. You, X. Chen, X. Zhou, Y. Wang and F. Pan, *How to manipulate magnetic states of antiferromagnets*, Nanotechnology, **29**, 11 (2018).

[167] A. Fert, V. Cros and J. Sampaio, *Skyrmions on the track*, Nature nanotechnology, **8**, 3 (2013).

[168] T. H. R. Skyrme, *A Non-Linear Theory of Strong Interactions*, Proceedings of the Royal Society of London. Series A. Mathematical, Physical & Engineering Sciences, **247**, 1249 (1958).

[169] S. Mühlbauer, B. Binz, F. Jonietz, C. Pfleiderer, A. Rosch, A. Neubauer, R. Georgii and P. Böni, *Skyrmion Lattice in a Chiral Magnet*, Science, **323**, 5916 (2009).

[170] X. Zhang, M. Ezawa and Y. Zhou, *Thermally stable magnetic skyrmions in multilayer synthetic antiferromagnetic racetracks*, Physical Review B, **94**, 6 (2016).

[171] A. K. Nayak, V. Kumar, T. Ma, P. Werner, E. Pippel, R. Sahoo, F. Damay, U. K. Rossler, C. Felser and S. S. P. Parkin, *Magnetic antiskyrmions above room temperature in tetragonal Heusler materials*, Nature, **548**, 7669 (2017).

[172] X. Zhang, Y. Zhou and M. Ezawa, *Antiferromagnetic Skyrmion: Stability, Creation and Manipulation*, Scientific Reports, **6**, (2016).

[173] M. dos Santos Dias, J. Bouaziz, M. Bouhassoune, S. Blügel and S. Lounis, *Chirality-driven orbital magnetic moments as a new probe for topological magnetic structures*, Nature Communications, **7**, (2016).

[174] M. C. Kautzky, A. V. Demtchouk, Y. Chen, K. M. Brown, S. E. McKinlay and J. Xue, *Atomic Layer Deposition Al_2O_3 Films for Permanent Magnet Isolation in TMR Read Heads*, IEEE Transactions on Magnetics, **44**, 11 (2008).

[175] K. Mistry, C. Allen, C. Auth, B. Beattie, D. Bergstrom, M. Bost, M. Brazier, M. Buehler, A. Cappellani, R. Chau, C.-H. Choi, G. Ding, K. Fischer, T. Ghani, R. Grover, W. Han, D. Hanken, M. Hattendorf, J. He, J. Hicks, R. Huessner, D. Ingerly, P. Jain, R. James, L. Jong, S. Joshi, C. Kenyon, K. Kuhn, K. Lee, H. Liu, J. Maiz, B. McIntyre, P. Moon, J. Neirynck, S. Pae, C. Parker, D. Parsons, C. Prasad, L. Pipes, M. Prince, P. Ranade, T. Reynolds, J. Sandford, L. Shifren, J. Sebastian, J. Seiple, D. Simon, S. Sivakumar, P. Smith, C. Thomas, T. Troeger, P. Vandervoorn, S. Williams and K. Zawadzki, in *2007 IEEE International Electron Devices Meeting*, 2007, pp. 247-250.

[176] H. H. Sønsteby, J. E. Bratvold, K. Weibye, H. Fjellvåg and O. Nilsen, *Phase Control in Thin Films of Layered Cuprates*, Chemistry of Materials, (2018).

[177] H. H. Sønsteby, T. Aarholt, Ø. Prytz, H. Fjellvåg and O. Nilsen, *First complex oxide superconductor by atomic layer deposition*, Chemival Communications, **54**, 59 (2018).

9 List of papers

Paper I:
"Atomic Layer Deposition of oriented nickel titanate (NiTiO$_3$)"
Jon E. Bratvold, Helmer Fjellvåg, Ola Nilsen, *Applied Surface Science,* **311**, 478–483 (2014).

Paper II:
"**Phase and orientation control of NiTiO$_3$ thin films**"
Jon E. Bratvold, Helmer Fjellvåg, Ola Nilsen, *manuscript for submission to Journal of Crystal Growth* (2019).

Paper III:
"**An iron(II) diketonate-diamine complex as precursor for thin film fabrication by atomic layer deposition**"
Jon E. Bratvold, Giorgio Carraro, Davide Barreca, Ola Nilsen, *Applied Surface Science,* **347**, 861–867 (2015).

Paper I

Atomic Layer Deposition of oriented nickel titanate (NiTiO$_3$)

Jon E. Bratvold, Helmer Fjellvåg and Ola Nilsen

Atomic Layer Deposition of oriented nickel titanate ($NiTiO_3$)

Jon E. Bratvold [*], Helmer Fjellvåg, Ola Nilsen

Centre for Materials Science and Nanotechnology (SMN), Department of Chemistry, University of Oslo, P.O. Box 1033 Blindern, N-0315 Oslo, Norway

ARTICLE INFO

ABSTRACT

The combination of the two well behaved binary oxide ALD processes, NiO ($Ni(acac)_2 + O_3$) and (TiO_2 ($TiO^iPr)_4 + H_2O$), provide excellent means for depositing thin films of $Ni_xTi_{1-x}O_y$ with highly controllable stoichiometry. In particular, stoichiometric $NiTiO_3$ was obtained for a 1:1 molar pulsing ratio of $NiO:TiO_2$. An ALD window was observed between 175 and 275 °C for this composition, within which the growth rate remained unchanged at ~43 pm/subcycle. The measured refractive index was 2.42 and a direct band gap of 2.27 eV was found. The described process yielded smooth (0.4–0.9 nm RMS roughness), crystalline films of $NiTiO_3$ as-deposited on Si (1 0 0) substrates, with a strained (0 0 1) orientation. Annealing at 650 °C for 15 min relaxed the strain and improved the crystallinity.

© 2014 Elsevier B.V. All rights reserved.

1. Introduction

Nickel titanate, $NiTiO_3$, belongs to the ilmenite family of materials with general formula $MTiO_3$ (M = Mg, Mn, Fe, Co, Ni, Zn). In the ilmenite type structure the Ti- and M-atoms are ordered into alternating layers along the hexagonal c-axis (space group 167, R-3). If the Ti- and M-atoms are randomly distributed this structure becomes isostructural to the corundum structure (space group 148, R-3c). The cations can also be "perfectly dispersed" with every Ti-atom surrounded by M-atoms and *vice versa*, yielding the $LiNbO_3$-type structure (space group 161, $R3c$). The different cation distributions may introduce magnetic ordering (R-3) [1] or multiferroism ($R3c$) [2–4]. Ilmenite materials are further suggested used as microwave dielectrics [5], gas sensors [6], and catalysts [7]. When chemically mixed with other materials, even more exotic properties may emerge. For instance, solid solutions of Fe_2O_3–$FeTiO_3$ show self-reversed thermoremanent magnetization [8] and significant exchange bias [9]. Additionally, nickel titanate exhibits photocatalytic properties [10], and is a potential high-κ dielectric material [11]. Nickel titanates have previously also been grown as thin films by techniques such as sol–gel processes [11,12], aerosol-assisted chemical vapor deposition [10], pulsed laser deposition [4] and radio frequency magnetron sputtering [13].

In the current work, we use the Atomic Layer Deposition (ALD) technique to grow nickel titanate thin films. The technique has many advantages [14], one of which is the possibility to grow conformal films with excellent control of composition at relatively low temperatures. The film is grown by cycles of sequential pulses of the different precursors, separated by purges of inert gas. In well behaved systems each pulse represents self-limiting reactions between the gas phase and the surface. The cycle is repeated until the desired thickness is achieved. Ternary materials are deposited by sequential combination of the processes for deposition of the binary materials. The deposited stoichiometry is tuned by varying the ratio of the binary processes.

Binary nickel oxide has previously been demonstrated by ALD using various types of precursors: $Ni(apo)_2$ [15], $Ni(acac)_2$ [15], $Ni(dmg)_2$ [15], $Ni(cp)_2$ [16,17], $Ni(MeCp)_2$ [18], $Ni(EtCp)_2$ [19], $Ni(thd)_2$ [20], $Ni(dmamp)_2$ [21] and $Ni(dmamb)_2$ [22]. The range of precursors explored for deposition of titanium is wide, as described in a recent review [23]. Here, we have chosen nickel acetylacetonate with ozone and titanium tetraisopropoxide with water as precursors due to their ease of handling, well documented processes, and low remains of residue in the deposited films.

Motivated by the exotic magnetic properties of nanolamellae in Fe_2O_3–$FeTiO_3$ solid solutions of geological origin [24,25], the current work focuses on ALD growth of $NiTiO_3$ as an interesting member of the ilmenite class of materials. In this respect, $NiTiO_3$ represents the first step towards synthetic Fe_2O_3–$NiTiO_3$ analogous solid solutions for detailed exploration. We present a robust ALD route towards $NiTiO_3$ thin films, along with structural and physical characterization of the achieved samples.

2. Experimental

The films were grown in an F-120 Sat reactor (ASM Microchemistry Ltd.) using $Ni(acac)_2$ (nickel acetylacetonate, 95%, Aldrich) with O_3 and $Ti(O^iPr)_4$ (titanium tetraisopropoxide, Ti-tip, 97%,

* Corresponding author. Tel.: +47 97668855.
  E-mail address: j.e.bratvold@kjemi.uio.no (J.E. Bratvold).

Aldrich) with de-ionized H_2O as precursors. For all experiments dried purified N_2 was used as a carrier and purging gas, supplied at a total flow of 500 cm^3/min. Nitrogen was produced with a Schmidlin UHPN3001 N_2 purifier, giving a mixture of >99.999% (N_2+Ar). This gas mixture was additionally dried by passing it through P_2O_5 and purified for remains of O_2 by means of a Mykrolis gas purifier, before being used as carrier gas. During depositions the reactor pressure was around 3 mbar.

Ni(acac)$_2$ was re-sublimated at 175 °C in-house before use to remove synthesis residues and water. It was kept at 175 °C inside the reactor to achieve sufficient vapor pressure during deposition. The O_3 was produced by feeding O_2 (99.6%, AGA) into a BMT 803 N ozone generator (BMT Messtechnik GMBH), with a claimed O_3 concentration of 8%. Ti-tip and de-ionized H_2O were kept in containers outside the reactor. Instead of heating the Ti-tip as is usually done [26], the container was equipped with an additional carrier gas of nitrogen to achieve sufficient dosages.

The films were deposited on soda-lime glass and polished 3.5 cm × 3.5 cm single crystal surfaces of Si (1 0 0). The soda-lime glass substrates were cleaned using ethanol, whereas the Si (1 0 0) substrates were blown free of dust with pressurized air and otherwise used as delivered.

Post-deposition annealing was performed by rapid thermal processing (RTP) in an MTI Corporation OTF-1200X furnace. The heating programme consisted of a 20 min ramp from room temperature to 650 °C, followed by a dwell time of 15 min, and subsequent cooling in the furnace to room temperature. The film thicknesses and refractive indices were measured by spectroscopic ellipsometry using a Woollam alpha-SE ellipsometer. The recorded data was fitted to a Cauchy model using the CompleteEASE software [27]. The metal (cationic) relative composition was determined by X-ray fluorescence (XRF) using a Philips PW2400 spectrometer and the UniQuant analysis software [28]. X-ray diffraction (XRD) was performed with a Bruker AXS D8 powder diffractometer equipped with a Ge (1 1 1) monochromator, providing Cu-Kα_1 radiation and using a LynxEye detector. Rocking curves were obtained on a PANalytical Empyrean diffractometer, using a proportional detector. Atomic force microscopy (AFM) was performed with a Park Instruments XE-70 to study the surface topography. The data was analyzed using the XEI software package. Optical absorption measurements were performed on a Shimadzu UV3600 photospectrometer.

3. Results and discussion

3.1. Deposition of binary oxides

The growth conditions for the binary oxides NiO and TiO_2 were selected on the basis of previous work [15,29] combined with own optimizations. The adopted pulsing and purging parameters for the NiO process were: 2 s Ni(acac)$_2$ pulse, 1.5 s purge, 3 s O_3 pulse, 3 s purge. An ALD window between 200 and 250 °C, where the change in both growth rate and refractive index were negligible, was revealed by varying the deposition temperature (Fig. 1). Both lower and higher deposition temperatures resulted in large thickness gradients. At 200 °C, the growth rate was ~45 pm/cycle which is lower than the previously reported growth rate of 62 pm/cycle by Utriainen et al. [15].

Due to its hygroscopic nature, the Ni-precursor is easily obtained as the hydrated species, Ni(acac)$_2$(H_2O)$_2$ [30]. In anhydrous state it forms a trimer, [Ni(acac)$_2$]$_3$ [31]. Upon prolonged exposure to moisture the evaporation rate of the precursor decreases, possibly owing to slow transformation into hydrated species [15]. At present it remains unknown how this change in chemistry affects the reactivity of the precursor and reaction mechanisms at the surface.
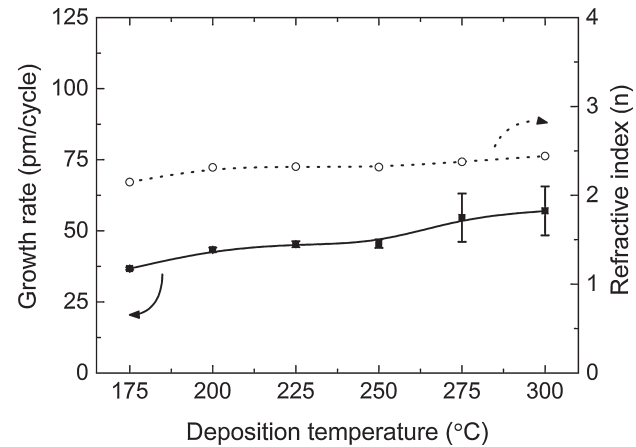

Fig. 1. Growth rate (solid line with filled squares) and refractive index (dotted line with open circles, error bars within data points) of NiO films as a function of deposition temperature. An ALD window exists in the range 200–250 °C.

XRD analysis was performed on NiO films deposited between 175 and 300 °C (Fig. 2). A preferred NiO (1 0 0) orientation was observed, and the (2 0 0) reflection is visible independent on the chosen deposition temperature. For depositions performed above 250 °C the NiO (1 1 1) reflection also appears clearly. Other allowed NiO Bragg reflections were observed at all temperatures, but with negligible intensities.

Deposition of TiO_2 from Ti-tip and water with ALD has been extensively studied during the last 20 years [32]. Different decomposition temperatures for Ti-tip are reported [29,33], and 250 °C appears to be the upper boundary for self-limiting growth [26]. The reports are somewhat inconclusive concerning the ALD window,
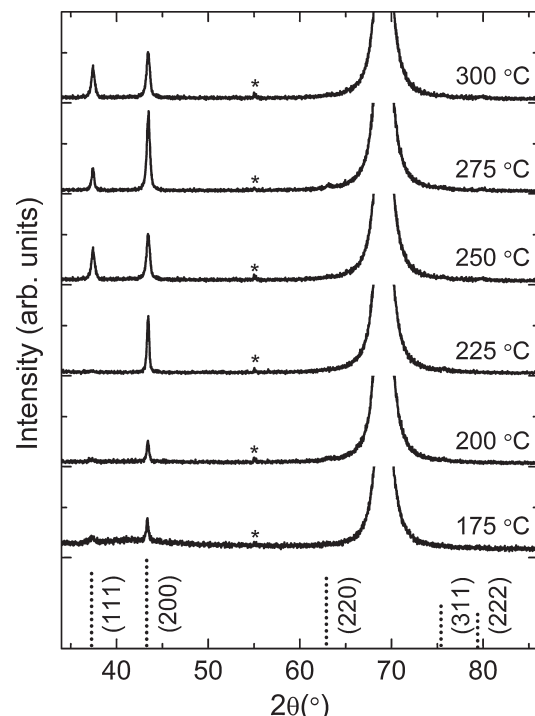

Fig. 2. XRD patterns of nickel oxide films deposited at different deposition temperatures as given on the figure. Positions of allowed reflections from NiO (space group 225, *Fm-3m*) are indicated by dotted lines at the bottom (PDF # 04-011-8441). The minor bump * is an instrumental artefact, while the Si (4 0 0) substrate reflection appears at $2\theta = 69°$; Cu Kα_1 radiation.
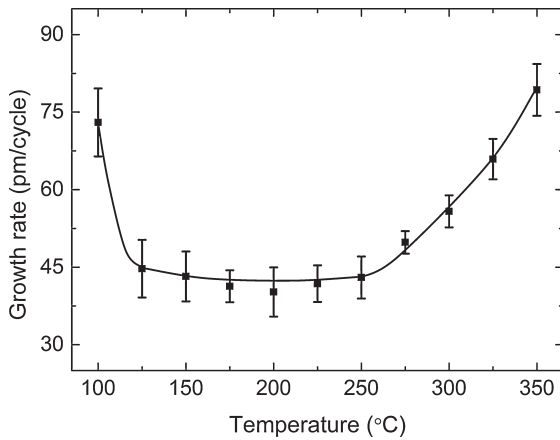
Fig. 3. Variation in growth rate of TiO$_2$ films as a function of deposition temperature. An ALD window is observed in the range 125–250 °C.

e.g. Aarik et al. [29] claim a lower limit of 150 °C due to insufficient reactivity of water at these temperatures. Our experiments are consistent with previous work [34], however, we observe a slightly extended ALD window covering 125 to 250 °C [26]. The observed growth rate within this temperature range was ~43 pm/cycle (Fig. 3). Optimized pulsing and purging parameters used were: 1 s Ti-tip pulse, 1 s purge, 2 s H$_2$O pulse, 2 s purge.

3.2. Growth of Ni–Ti–O films

Based on the findings for the binary oxides, an initial deposition temperature of 250 °C was chosen for the ternary Ni–Ti–O system. In order to determine an optimal pulsing ratio of NiO: TiO$_2$ for achieving NiTiO$_3$ stoichiometry, a series of Ni–Ti–O films were made with different pulsing ratios between NiO and TiO$_2$ (Fig. 4).

The pulsed composition was almost directly transferred to the growing film, where a 1:1 stoichiometry between Ni and Ti was observed for a 1:1 NiO:TiO$_2$ pulsing ratio.

To compare growth rates of the Ni–Ti–O series with binary oxide films one supercycle was defined as (xNiO + yTiO$_2$), and the growth rates were then normalized with respect to the number of binary oxide subcycles: growth rate (supercycle)/($x+y$) = growth rate (subcycle). For a 1:1 pulsing ratio a growth rate of ~43 pm/subcycle (~86 pm/supercycle) was observed, comparable with the growth rates for both of the end member oxides. A slightly lower growth rate was found for some intermediate compositions (Fig. 5).
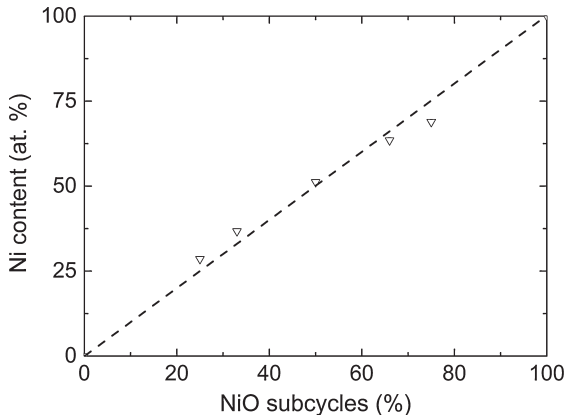
Fig. 4. Ni content (as measured by XRF) in Ni–Ti–O films *versus* fraction of Ni pulses (in terms of NiO subcycles). All depositions were made at 250 °C on Si (1 0 0) substrates. Error bars are within data points.
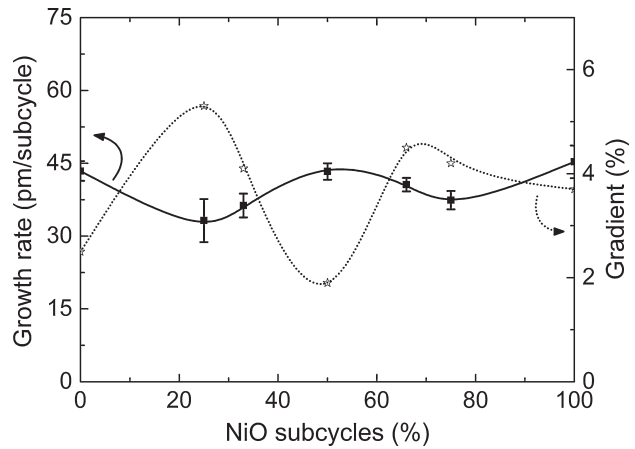
Fig. 5. Growth rate (solid line with filled squares) and gradient along flow direction (dotted line with open stars, error bars within data points) *versus* fraction of Ni pulses (in terms of NiO subcycles). All depositions were made at 250 °C on Si (1 0 0) substrates.

Within this system, the thickness gradient along the flow direction showed a reversed relationship with the growth rate: a high growth rate was accompanied by a small gradient, and *vice versa* (Fig. 5).

This gradient appearance may indicate that the growth is hindered and possibly less controlled when the film grow in its two-phase regions (see phase diagram in ref. [35]). Both end members (NiO and TiO$_2$) as well as the 1:1 composition (NiTiO$_3$) are well known phases, while other known phases in the intermediate ranges exist only at elevated temperatures [35]. Thus, films with intermediate compositions comprise of the mentioned phases, probably as well as some amorphous material.

Depositions were made with a 1:1 pulsing ratio in the temperature range 150–300 °C (Fig. 6). The growth rate and the composition of the deposited films remained virtually unchanged between 175 and 275 °C. This represents an extension of the ALD window compared to those of the binary oxides, apart from the lower temperature end of the TiO$_2$-process (Figs. 1 and 3). A similar stabilization of a ternary system has previously been observed for ALD growth of manganites [36].
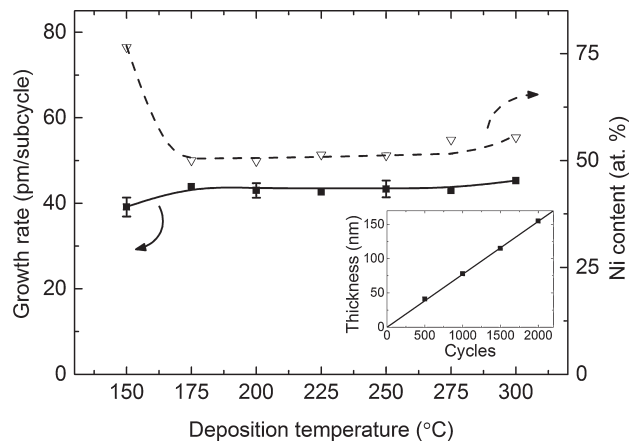

Fig. 6. Composition (dashed line with open triangles, error bars within data points) and growth rate (solid line with filled squares) *versus* deposition temperature for films made with a 1:1 NiO:TiO$_2$ pulsing ratio. An ALD window is observed between 175 and 275 °C, within which the variations in growth rate and composition were negligible. The thickness is linearly dependent on the number of deposition cycles (inset) for films deposited at 250 °C.
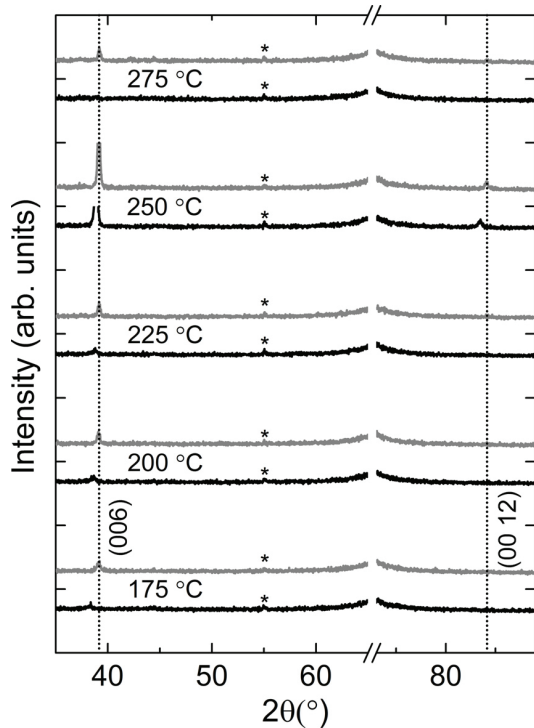
Fig. 7. XRD patterns of nickel titanate films before (black) and after annealing (grey) at 650 °C for 15 min with accompanying deposition temperatures indicated in between. All depositions were made with 500 supercycles, apart from the film deposited at 250 °C where 1500 supercycles was used. Bragg positions for NiTiO$_3$ (0 0 6) and (0 0 12) are given as dotted lines (PDF # 04-12-0745). The small bump * represent an instrument artefact, and the Si (4 0 0) reflection at $2\theta = 69°$ is removed for clarity; Cu Kα_1 radiation.

Fig. 8. Rocking curves around NiTiO$_3$ (0 0 6) for films deposited at 250 °C on Si (1 0 0) before (black) and after (grey) annealing at 650 °C for 15 min. The FWHM values are 14.8° for the as-deposited film and 10.7° for the annealed film.

3.3. Crystallinity – NiTiO$_3$ films

The crystallinity of films deposited within the ALD-window was examined by x-ray diffraction (XRD). These films were made during 500 supercycles, yielding a thickness of ~43 nm. In addition, one film was deposited at 250 °C during 1500 supercycles, yielding a thickness of ~130 nm. The diffractograms revealed a (0 0 1) orientation of the as-deposited films, as the only visible reflections were NiTiO$_3$ (0 0 6) and NiTiO$_3$ (0 0 12), the latter being much more prominent in the thicker film deposited at 250 °C (Fig. 7). For as-deposited films, all reflections were slightly shifted towards smaller angles (using the Si (4 0 0) reflection as reference), compared to tabulated values (PDF # 04-012-0745). This shift can be interpreted as strain along the [0 0 1] direction, giving a longer c-axis than expected from bulk.

Annealing at 650 °C for 15 min improved the crystallinity, and also caused relaxation of the lattice, visible by the reflections shifting to positions identical to theoretical values. Untreated films had a c-axis of 13.90 Å, while the c-axis of annealed films was identical to the bulk value of 13.79 Å (PDF # 04-12-0745). If Poisson's effect can be assumed for this system, the as-deposited films should have a shorter a-/b-axis and a longer c-axis, compared to bulk. Relaxing the strain upon annealing would cause the c-axis to shrink, along with a linked expansion of the basal plane. However, further investigations are needed to conclude on the nature of the basal plane.

To examine the change in crystallinity upon heating, rocking curves were performed around the NiTiO$_3$ (0 0 6) reflection for untreated and annealed films, both deposited at 250 °C. In the as-deposited state the (0 0 6) reflection was very broad with a full-width-at-half-maximum (FWHM) of 14.8°. Annealing clearly improved the crystallinity and lead to a decrease in FWHM to 10.7° (Fig. 8).
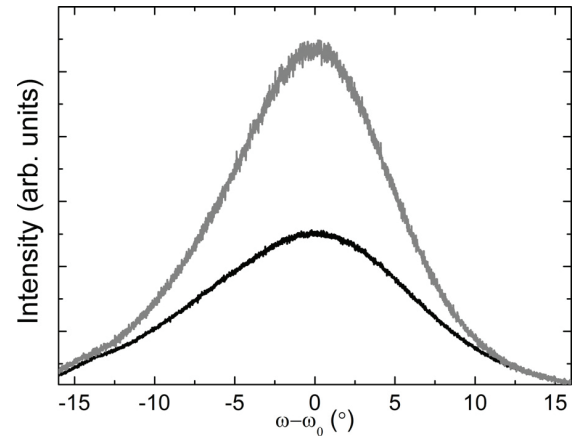
3.4. Topography and crystallite size – NiTiO$_3$ films

Atomic force microscopy (AFM) was performed on the same set of samples as for the XRD investigations. A representative example is given in Fig. 9, showing an untreated film grown at 225 °C.

All the films were smooth with root-mean-square (rms) roughness values ranging from 0.4 nm to 0.9 nm, roughness increasing with deposition temperature (Fig. 10). Annealing lowered the roughness compared to the as-deposited films. The crystallite size increased with deposition temperature for both the as-deposited (20–43 nm) and annealed (34–47 nm) series, and also increased with annealing (Fig. 10).

3.5. Optical properties – NiTiO$_3$ films

Refractive index data were obtained from ellipsometry, at a wavelength of 632.8 nm, for films deposited between 150 and 300 °C. A slight decrease in refractive index was observed for films deposited outside the ALD window, while between 175 and 275 °C
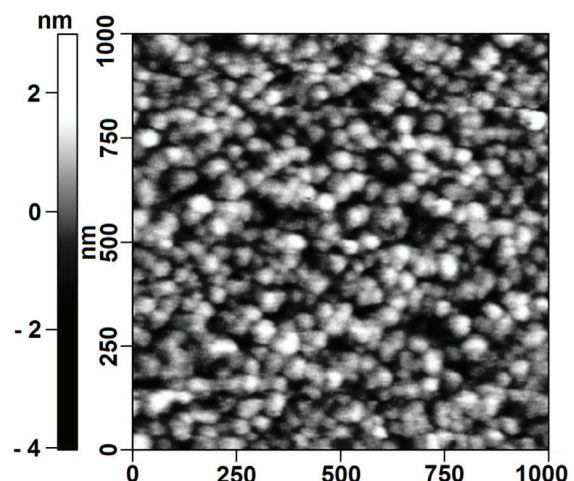

Fig. 9. AFM image of a NiTiO$_3$ film as-deposited at 225 °C, with a root-mean-square (rms) roughness of 0.65 nm and an average crystallite size of 37 nm.
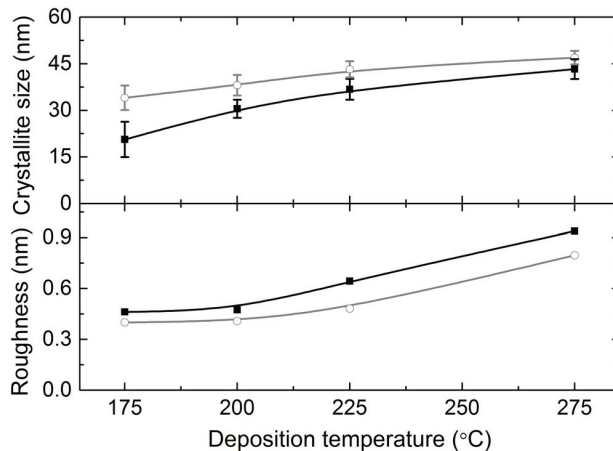
Fig. 10. Deposition temperature dependence on root-mean-square (rms) roughness (bottom) and crystallite size (top) of NiTiO$_3$ films as measured by AFM. Black lines with filled squares: as-deposited films. Grey lines with open circles: annealed films.

the variation was negligible around the value of 2.42 (inset in Fig. 11).

Optical absorption measurements were performed on a film deposited at 250 °C on soda-lime glass. The accompanying Tauc plot [37] revealed a direct band gap of 2.27 eV (Fig. 11), correlating well with the yellowish colour of the film. Previous reports on the band gap of NiTiO$_3$ vary greatly from values around 2.12 eV to 3.43 eV [38–44]. Different ways of determining the band gap (absorption spectra, theoretical calculations, XAS/XES *etc.*) and different states of the material (bulk, nanoparticles *etc.*) could possibly explain these large variations. In correspondence with the observed band gap, NiTiO$_3$ has been shown as a useful material for water purification by irradiation of UV light [45].

The current successful deposition of crystalline NiTiO$_3$ thin films by ALD opens up for future studies of the complex solid solutions between Fe$_2$O$_3$ and NiTiO$_3$. We consider these solid solutions as highly relevant model systems for investigating phenomena related to the unique exchange bias properties in Fe$_2$O$_3$–FeTiO$_3$ nanostructures of mineralogical origin. In antiferromagnetic NiTiO$_3$ the magnetic moments are reported as ferromagnetically ordered in the basal plane within each cation layer, however, with layers ordered antiparallel along the *c*-axis [1]. Our films deposited with
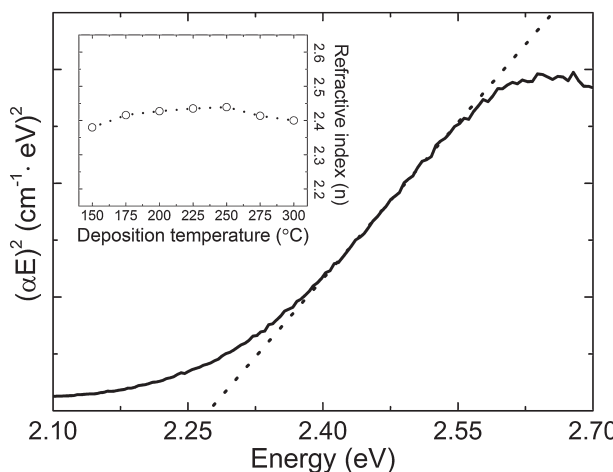
ALD have a preferred orientation along the *c*-axis. This feature, along with the technique used, should make them perfect for coupling with other materials to induce specific magnetic properties like exchange bias [46] at interfaces.

4. Conclusions

Thin films in the Ni–Ti–O system were deposited by Atomic Layer Deposition. The composition was linearly dependent on pulsing ratio from TiO$_2$ to NiO. Special attention was given to the NiTiO$_3$ stoichiometry, obtainable by a 1:1 pulsing ratio of NiO:TiO$_2$. An ALD window was observed in the temperature interval 175–275 °C, within which neither the growth rate nor composition changed significantly. Films deposited at these temperatures had a refractive index of 2.42 and a direct band gap of 2.27 eV. The films were crystalline as-deposited, with a (0 0 1) orientation. An elongated *c*-axis, compared to bulk, was attributed to strain. Annealing of the films improved the crystallinity and relaxed the strain. Both root-mean-square roughness and crystallite size increased with increasing deposition temperature, while annealing decreased the roughness and increased the crystallite size.

Acknowledgement

References

[1] G. Shirane, S.J. Pickart, R. Nathans, Y. Ishikawa, Neutron-diffraction study of antiferromagnetic FeTiO$_3$ and its solid solutions with α-Fe$_2$O$_3$, J. Phys. Chem. Solids 10 (1959) 35–43.
[2] X. Deng, W. Lu, H. Wang, H. Huang, J. Dai, Electronic, magnetic and dielectric properties of multiferroic MnTiO$_3$, J. Mater. Res. 27 (2012) 1421–1429.
[3] T. Varga, T.C. Droubay, M.E. Bowden, R.J. Colby, S. Manandhar, V. Shutthanandan, D. Hu, B.C. Kabius, E. Apra, W.A. Shelton, S.A. Chambers, Coexistence of weak ferromagnetism and polar lattice distortion in epitaxial NiTiO$_3$ thin films of the LiNbO$_3$-type structure, J. Vac. Sci. Technol. B: Microelectron. Nanometer Struct. 31 (2013) 030603.
[4] T. Varga, T.C. Droubay, M.E. Bowden, P. Nachimuthu, V. Shutthanandan, T.B. Bolin, W.A. Shelton, S.A. Chambers, Epitaxial growth of NiTiO$_3$ with a distorted ilmenite structure, Thin Solid Films 520 (2012) 5534–5541.
[5] Y.-C. Wu, S.-F. Wang, L.-G. Teng, Microstructures and dielectric properties of MgTiO$_3$ thick film prepared using aerosol deposition method, Ferroelectrics 435 (2012) 137–147.
[6] X. Chu, X. Liu, G. Wang, G. Meng, Preparation and gas-sensing properties of nano-CoTiO$_3$, Mater. Res. Bull. 34 (1999) 1789–1795.
[7] Y.-W. Wang, P.-H. Yuan, C.-M. Fan, Y. Wang, G.-Y. Ding, Y.-F. Wang, Preparation of zinc titanate nanoparticles and their photocatalytic behaviors in the photodegradation of humic acid in water, Ceram. Int. 38 (2012) 4173–4180.
[8] G.L. Nord Jr., C.A. Lawson, Order-disorder transition-induced twin domains and magnetic properties in ilmenite–hematite, Am. Mineral. 74 (1989) 160–176.
[9] S.A. McEnroe, B. Carter-Stiglitz, R.J. Harrison, P. Robinson, K. Fabian, C. McCammon, Magnetic exchange bias of more than 1 Tesla in a natural mineral intergrowth, Nat. Nanotechnol. 2 (2007) 631–634.
[10] A.A. Tahir, M. Mazhar, M. Hamid, K.G. Wijayantha, K.C. Molloy, Photooxidation of water by NiTiO$_3$ deposited from single source precursor [Ni$_2$Ti$_2$(OEt)$_2$(μ-OEt)$_6$(acac)$_4$] by AACVD, Dalton Trans. (2009) 3674–3680.
[11] S.-H. Chuang, M.-L. Hsieh, S.-C. Wu, H.-C. Lin, T.-S. Chao, T.-H. Hou, Fabrication and characterization of high-k dielectric nickel titanate thin films using a modified sol–gel method, J. Am. Ceram. Soc. 94 (2011) 250–254.
[12] M.R. Mohammadi, D.J. Fray, Mesoporous and nanocrystalline sol–gel derived NiTiO$_3$ at the low temperature: controlling the structure, size and surface area by Ni:Ti molar ratio, Solid State Sci. 12 (2010) 1629–1640.
[13] A.I. Inamdar, J. Kim, B. Jang, D. Kim, H. Im, W. Jung, H. Kim, Memory conductance switching in a Ni–Ti–O compound thin film, Jpn. J. Appl. Phys. 51 (2012) 104102.
[14] S.M. George, Atomic layer deposition: an overview, Chem. Rev. (Washington, DC, US) 110 (2010) 111–131.
[15] M. Utriainen, M. Kroger-Laukkanen, L. Niinisto, Studies of NiO thin film formation by atomic layer epitaxy, Mater. Sci. Eng. B B54 (1998) 98–103.
[16] H.L. Lu, G. Scarel, C. Wiemer, M. Perego, S. Spiga, M. Fanciulli, G. Pavia, Atomic layer deposition of NiO films on Si(1 0 0) using cyclopentadienyl-type compounds and ozone as precursors, J. Electrochem. Soc. 155 (2008) H807.
[17] J. Bachmann, A. Zolotaryov, O. Albrecht, S. Goetze, A. Berger, D. Hesse, D. Novikov, K. Nielsch, Stoichiometry of nickel oxide films prepared by ALD, Chem. Vap. Depos. 17 (2011) 177–180.

Fig. 11. Tauc plot for a NiTiO$_3$ film deposited at 250 °C. A direct band gap was found at 2.27 eV. Inset: Refractive indices for NiTiO$_3$ samples as function of deposition temperature. Error bars are within data points.

[18] S.J. Song, S.W. Lee, G.H. Kim, J.Y. Seok, K.J. Yoon, J.H. Yoon, C.S. Hwang, J. Gatineau, C. Ko, Substrate dependent growth behaviors of plasma-enhanced atomic layer deposited nickel oxide films for resistive switching application, Chem. Mater. 24 (2012) 4675–4685.

[19] H.L. Lu, G. Scarel, X.L. Li, M. Fanciulli, Thin MnO and NiO films grown using atomic layer deposition from ethylcyclopentadienyl type of precursors, J. Cryst. Growth 310 (2008) 5464–5468.

[20] E. Lindahl, M. Ottosson, J.-O. Carlsson, Atomic layer deposition of NiO by the Ni(thd)$_2$/H$_2$O precursor combination, Chem. Vap. Depos. 15 (2009) 186–191.

[21] T.S. Yang, W. Cho, M. Kim, K.-S. An, T.-M. Chung, C.G. Kim, Y. Kim, Atomic layer deposition of nickel oxide films using Ni(dmamp)$_2$ and water, J. Vac. Sci. Technol. A: Vac. Surf. Films 23 (2005) 1238.

[22] P. Antony Premkumar, M. Toeller, C. Adelmann, J. Meersschaut, A. Franquet, O. Richard, H. Tielens, B. Brijs, A. Moussa, T. Conard, H. Bender, M. Schaekers, J.A. Kittl, M. Jurczak, S. Van Elshocht, NiO thin films synthesized by atomic layer deposition using Ni(dmamb)$_2$ and ozone as precursors, Chem. Vap. Depos. 18 (2012) 61–69.

[23] V. Miikkulainen, M. Leskelä, M. Ritala, R.L. Puurunen, Crystallinity of inorganic films grown by atomic layer deposition: overview and general trends, J. Appl. Phys. 113 (2013) 021301.

[24] P. Robinson, R.J. Harrison, S.A. McEnroe, R.B. Hargraves, Lamellar magnetism in the haematite-ilmenite series as an explanation for strong remanent magnetization, Nature (London, UK) 418 (2002) 517–520.

[25] P. Robinson, R.J. Harrison, S.A. McEnroe, R.B. Hargraves, Nature and origin of lamellar magnetism in the hematite–ilmenite series, Am. Mineral. 89 (2004) 725–747.

[26] A. Rahtu, M. Ritala, Reaction mechanism studies on titanium isopropoxide-water atomic layer deposition process, Chem. Vap. Depos. 8 (2002) 21–28.

[27] CompleteEASE Version 4.41, J.A. Woollam Co. Inc., Lincoln, NE, USA, 2009.

[28] UniQuant Version 2 User Manual, Omega Data Systems, Veldhoven, The Netherlands, 1994.

[29] J. Aarik, A. Aidla, T. Uustare, M. Ritala, M. Leskelä, Titanium isopropoxide as a precursor for atomic layer deposition. Characterization of titanium dioxide growth process, Appl. Surf. Sci. 161 (2000) 385–395.

[30] M. Kudrat-E-Zahan, Y. Nishida, H. Sakiyama, Identification of cis/trans isomers of bis(acetylacetonato)nickel(II) complexes in solution based on electronic spectra, Inorg. Chim. Acta 363 (2010) 168–172.

[31] G.J. Bullen, R. Mason, P. Pauling, The crystal and molecular structure of bis(acetylacetonato)-nickel(II), Inorg. Chem. 4 (1965) 456–462.

[32] M. Ritala, M. Leskelä, L. Niinisto, P. Haussalo, Titanium isopropoxide as a precursor in atomic layer epitaxy of titanium dioxide thin films, Chem. Mater. 5 (1993) 1174–1181.

[33] A. Kosola, M. Putkonen, L.-S. Johansson, L. Niinistö, Effect of annealing in processing of strontium titanate thin films by ALD, Appl. Surf. Sci. 211 (2003) 102–112.

[34] R. Matero, A. Rahtu, M. Ritala, M. Leskelä, T. Sajavaara, Effect of water dose on the atomic layer deposition rate of oxide thin films, Thin Solid Films 368 (2000) 1–7.

[35] A. Muan, Equilibrium relations in the system nickel(II) oxide-titania in the temperature range 1300° to 1750°C, J. Am. Ceram. Soc. 75 (1992) 1357–1360.

[36] O. Nilsen, E. Rauwel, H. Fjellvåg, A. Kjekshus, Growth of La$_{1-x}$Ca$_x$MnO$_3$ thin films by atomic layer deposition, J. Mater. Chem. 17 (2007) 1466.

[37] J. Tauc, R. Grigorovici, A. Vancu, Optical properties and electronic structure of amorphous germanium, Phys. Status Solidi 15 (1966) 627–637.

[38] R.S. Singh, T.H. Ansari, R.A. Singh, B.M. Wanklyn, Electrical conduction in NiTiO$_3$ single crystals, Mater. Chem. Phys. 40 (1995) 173–177.

[39] Y. Xu, M.A.A. Schoonen, The absolute energy positions of conduction and valence bands of selected semiconducting minerals, Am. Mineral. 85 (2000) 543–556.

[40] A. Agui, M. Mizumaki, Intermetallic charge transfer and band gap of MTiO$_3$ (M = Mn, Fe, Co, and Ni) studied by O 1s-edge X-ray emission spectroscopy, J. Electron Spectrosc. Relat. Phenom. 184 (2011) 463–467.

[41] Y.-J. Lin, Y.-H. Chang, W.-D. Yang, B.-S. Tsai, Synthesis and characterization of ilmenite NiTiO$_3$ and CoTiO$_3$ prepared by a modified Pechini method, J. Non-Cryst. Solids 352 (2006) 789–794.

[42] K.S. Beenakumari, Synthesis and characterisation of nano-sized nickel titanate photocatalyst, J. Exp. Nanosci. 8 (2013) 203–209.

[43] P.H.M. de Korte, G. Blasse, Water photoelectrolysis using nickel titanate and niobate as photoanodes, J. Solid State Chem. 44 (1982) 150–155.

[44] R. Vijayalakshmi, V. Rajendran, Effect of reaction temperature on size and optical properties of NiTiO$_3$ nanoparticles, J. Chem. 9 (2012) 282–288.

[45] P.-h. Yuan, C.-m. Fan, G.-y. Ding, Y.-f. Wang, X.-c. Zhang, Preparation and photocatalytic properties of ilmenite NiTiO$_3$ powders for degradation of humic acid in water, Int. J. Miner. Metall. Mater. 19 (2012) 372–376.

[46] P. Robinson, R.J. Harrison, K. Fabian, S.A. McEnroe, Chemical and magnetic properties of rapidly cooled metastable ferri-ilmenite solid solutions: implications for magnetic self-reversal and exchange bias—III. Magnetic interactions in samples produced by Fe-Ti ordering, Geophys. J. Int. 191 (2012) 1025–1047.

Paper II

Phase and orientation control of NiTiO$_3$ thin films

Jon E. Bratvold, Helmer Fjellvåg and Ola Nilsen

Phase and orientation control of NiTiO$_3$ thin films

Jon E. Bratvold, Helmer Fjellvåg, Ola Nilsen

Centre for Materials Science and Nanotechnology (SMN), Department of Chemistry,

University of Oslo, P.O. Box 1033 Blindern, N-0315 Oslo, Norway

Abstract

Subtle changes in the atomic arrangement of NiTiO$_3$ in the ilmenite structure affects its symmetry and properties. At high temperatures, the cations are randomly distributed throughout the structure, resulting in the corundum structure with $R-3c$ symmetry. Upon cooling, the cations order in alternating layers along the crystallographic c axis, resulting in the ilmenite structure with $R-3$ symmetry. Related to this is the $R3c$ symmetry, where the cations alternate both perpendicular and along the c axis. NiTiO$_3$ with the latter structure is highly interesting as it exhibits ferroelectric properties. The close relationship between structure and properties for ilmenite related structures emphasizes the importance of being able to control the symmetry during synthesis. We show that the orientation and symmetry of thin films of NiTiO$_3$ formed by atomic layer deposition (ALD) can be controlled by choice of substrate. The disordered phase ($R-3c$), previously only observed at elevated temperatures, have been deposited at 250 °C on α-Al$_2$O$_3$ substrates, while post deposition annealing at moderate temperatures (650 °C) induces ordering ($R-3$). We have in addition explored the symmetry and epitaxial orientation obtained when deposited on substrates of LaAlO$_3$(100)$_c$, SrTiO$_3$(100) and MgO(100). The presented work demonstrates the possibilities of ALD to form metastable phases through choice of substrates.

Keywords

1. Introduction

NiTiO$_3$ (NTO) is a technologically relevant material proven suitable within photo catalysis, high-k dielectrics and nonvolatile memory [1-5]. In addition, *ab initio* calculations predict ferroelectricity and crystal structure dependent weak ferromagnetism, potentially suitable for sensor, microwave and spintronic applications [6]. At elevated temperatures, NTO adopts the corundum structure (space group $R-3c$, Figure 1) with random distribution of cations [7]. This disordered phase has so far been unquenchable, as cooling induces ordering of the two different

cations in alternating layers perpendicular to the crystallographic c axis. As ordering occurs the c glide plane is lost, and the structure is known as the ilmenite structure ($R-3$, Figure 1) [8]. This is also the case for ilmenite ($FeTiO_3$) itself, which additionally has been proven to adopt the related and technologically interesting $LiNbO_3$ structure ($R3c$, Figure 1) at high temperature and pressure [9]. In the $R3c$ structure, the two different cations alternate perfectly, both parallel and perpendicular to the c axis (Figure 1). Distinguishing between the three different symmetries by the position of the reflections from x-ray diffraction is difficult. Unit cell values obtained from density functional theory calculations on $R-3c$ and $R3c$ are virtually the same [10], and effects from strain or off-stoichiometry are likely to be much larger. However, determining whether the symmetry is $R-3$ or $R-3c/R3c$ is easy, as the diffraction pattern from $R-3$ has reflections from ordering not allowed with the c glide plane of $R-3c/R3c$ due to extinction rules. While there are no reports of bulk NTO with $R3c$ structure, the phase was claimed to have been obtained by Varga et. al on α-Al_2O_3 substrates as thin films made by pulsed laser deposition [10]. Even though the symmetry was not unambiguously confirmed, some degree of lattice polarization was observed, and possibly also weak ferromagnetism, indicating the presence of the $LiNbO_3$ structure [11, 12]. Ferroelectricity and weak ferromagnetism have indeed been observed in bulk samples of NTO as well [13], but the report did not discuss the crystal symmetry of the samples.
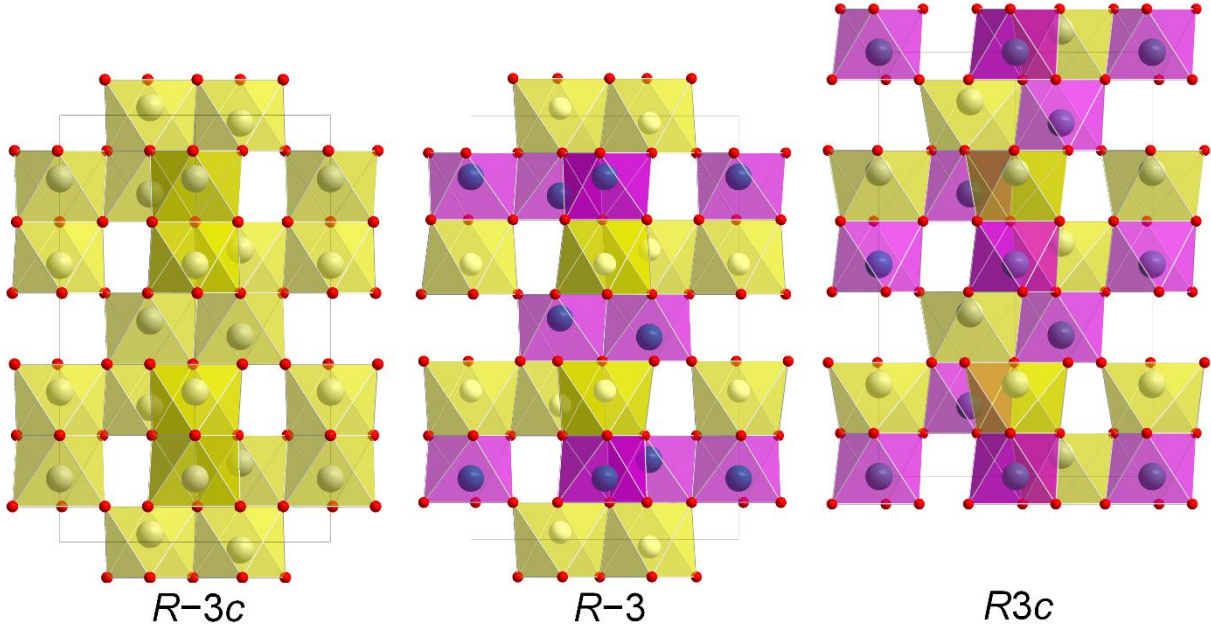
Figure 1: Schematic showing the similarity between the unit cells of space groups $R-3c$ (left), $R-3$ (center) and $R3c$ (right), viewed along [110]. The $R3c$ structure is shifted up one cation layer to emphasize the relation to the two other structures.

Thin films of NTO have previously been made by various deposition techniques, including aerosol-assisted CVD [2], sol-gel methods [3, 14-17], dip-coating [18] and RF-sputtering [4, 5], as well as with the previously mentioned pulsed laser deposition [10-12]. Especially for the latter technique, compositional control seems to be challenging. In addition, all methods require elevated temperatures (> 500 °C) either during deposition or by post-deposition annealing. While amorphous films might be desirable for some applications, a well-defined crystallinity and orientation is usually required to make use of the material. The atomic layer deposition (ALD) technique offers an alternative route for deposition of epitaxial thin films, provided careful selection of substrates [19, 20], at relatively low temperatures (typically < 400 °C). We have previously reported details about the deposition of NTO by ALD [21]. As deposited films on Si(100) with a 1:1 ratio between Ni and Ti (within 1%, as measured by X-ray fluorescence), all showed a preferred (00l) orientation in the deposition temperature range 175–275 °C. No sign of the ordering reflections belonging to the $R-3$ symmetry were visible at any temperature, neither before nor after annealing. Given the difficulty of obtaining the $R3c$ phase in bulk, the films deposited on Si(100) were assumed to have the disordered $R-3c$ symmetry. However, from the limited amount of data the $R3c$ symmetry can not be ruled out. In the work presented here, we show the possibility to control the orientation and crystallinity of deposited NTO films with the use of various single crystal substrates. As with the previously reported films deposited on Si(100), the films discussed here are assumed to have the $R-3c$ symmetry whenever the ordering reflections are not present.

2. Experimental

The films were deposited in an F-120 Sat reactor (ASM Microchemistry Ltd.) using the precursors Ni(acac)$_2$ (nickel acetylacetonate, 95%, Aldrich Chemistry) in combination with O$_3$ (produced in a BMT Messtechnik GMBH ozone generator from 99.6% O$_2$, AGA), and TTIP (Titanium(IV) tetraisopropoxide, 97%, Aldrich Chemistry) with deionized water. A pulsing and purging sequence of (2 s Ni(acac)$_2$ – 1.5 s purge – 3 s O$_3$ – 2 s purge) + (0.5 s TTIP – 1 s purge – 2 s H$_2$O – 3 s purge) were used for all depositions, as described more thoroughly in our prior work on deposition of NTO [21]. Substrates used were 3 x 3 cm^2 single crystals of Si(100), for thickness and composition determination, as well as α-Al$_2$O$_3$(001) (referred to simply as Al$_2$O$_3$ from now on), LaAlO$_3$(100) (LAO), SrTiO$_3$(100) (STO) and MgO(100) for structural analysis. All substrates were blown clean of dust using pressurized air before being placed in the reaction chamber, and subjected to 15 s of O$_3$ immediately before deposition. The films grown on Al$_2$O$_3$ and MgO were deposited in the same experiment with a nominal thickness of 165 nm (measured

on Si(100) substrates). Likewise, the films grown on STO and LAO were deposited in the same experiment with a nominal thickness of 130 nm (measured on Si(100) substrates). All depositions were performed at 250 °C. Annealing was done in air by rapid thermal processing (RTP) in an MTI Corporation OTF-1200X furnace. The heating program consisted of a 15 min. ramp from room temperature to 650 °C, followed by a dwell time of 15 min., and subsequent cooling in the furnace to room temperature, for a typical duration of 30 min.

The film thicknesses were measured by spectroscopic ellipsometry on Si(100) substrates, using a J. A. Woollam alpha-SE ellipsometer. The CompleteEASE software package was used to fit a Cauchy function to the obtained data in the 390–900 nm wavelength range. The cationic composition was determined by X-ray fluorescence (XRF) measurements on the Si substrates using a Philips PW2400 spectrometer and the UniQuant analysis software [22]. All θ-2θ X-ray diffraction (XRD) was performed on a Bruker AXS D8 Discover diffractometer in Bragg-Brentano configuration with Cu Kα radiation. The diffractometer was equipped with a Ge(111) monochromator and a LynxEye strip detector. Reciprocal space maps and φ scans were collected using a PANalytical Empyrean diffractometer, equipped with a Cu Kα source powered at 45 kV/40 mA, a hybrid monochromator and a PIXcel[3D] detector. Atomic force microscopy (AFM) was performed with a Park Systems XE-70 AFM, equipped with a PPP-CONSTCR tip (Nanosystems) in contact mode.

Literature values for NTO in this paper are referring to the PDF# 01-075-3757 (ICDD) [23]. The listed cell parameters of the unit cell, having the ilmenite structure ($R-3$), are $a = 5.0321$ Å and $c = 13.7924$ Å.

3. Results

To provoke different crystallographic orientations, films were deposited on a range of single crystalline substrates: Al_2O_3(001), LAO(100), STO(100) and MgO(100). The results will be presented in this order below.

3.1 On Al_2O_3(001)

An obvious choice of substrates for growth of NTO thin films is Al_2O_3, as the two materials adopt closely related crystal structures. Al_2O_3 lends its mineral name to the corundum structure ($R-3c$), while $NiTiO_3$ has the same structure as its iron counterpart ilmenite ($FeTiO_3$), at room temperature ($R-3$) (Figure 1). The unit cell parameters of Al_2O_3 ($a = 4.76$ Å, $c = 12.99$ Å, PDF

00-046-1212 [24]) are distinctly smaller than for NTO (a = 5.03 Å, c = 13.79 Å, PDF 01-075-3757 [23]).

As deposited NTO films were (00l) oriented on Al_2O_3(001), as observed by θ-2θ X-ray diffraction (Figure 2). Upon annealing, two additional reflections appeared: (003) and (009). These reflections are only present for the R−3 symmetry due to extinction rules, and can thus be used to differentiate between cation order (R−3) and disorder (R−3c). It should be noted that the (003) and (009) reflections are also absent for the $R3c$ symmetry. However, as mentioned in the introduction, since this symmetry has never been irrefutably observed for NTO it is assumed in the following that the (00l) oriented films presented here have the R−3c symmetry, whenever the (003) and (009) reflections are not present.
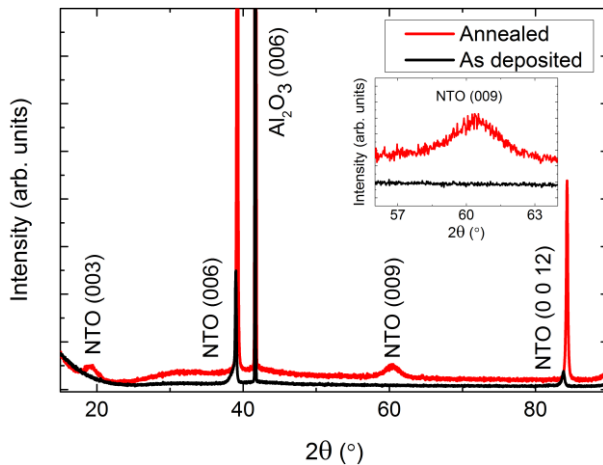
Figure 2: XRD of (00l) oriented NTO on Al_2O_3(001) showing the transition from space group R−3c as deposited (black line) to R−3, upon annealing (red line). The ordering reflections (003) and (009) are not visible for the as deposited films, as shown in the inset.

The crystallinity of the film improved drastically upon annealing, clearly visible from the reciprocal space map (RSM) of the NTO (006) reflection by an increase in intensity (Figure 3). A decrease in full width at half maximum (FWHM) along $q_\parallel$, from 1.0° to 0.7°, was also observed. Annealing shortened the c axis length, visible as a shift of the position of the (006) reflection to a larger q value, along $q_\perp$. The c axis was 0.4% longer in the as deposited film and 0.1% shorter in the annealed film, compared to the literature value.
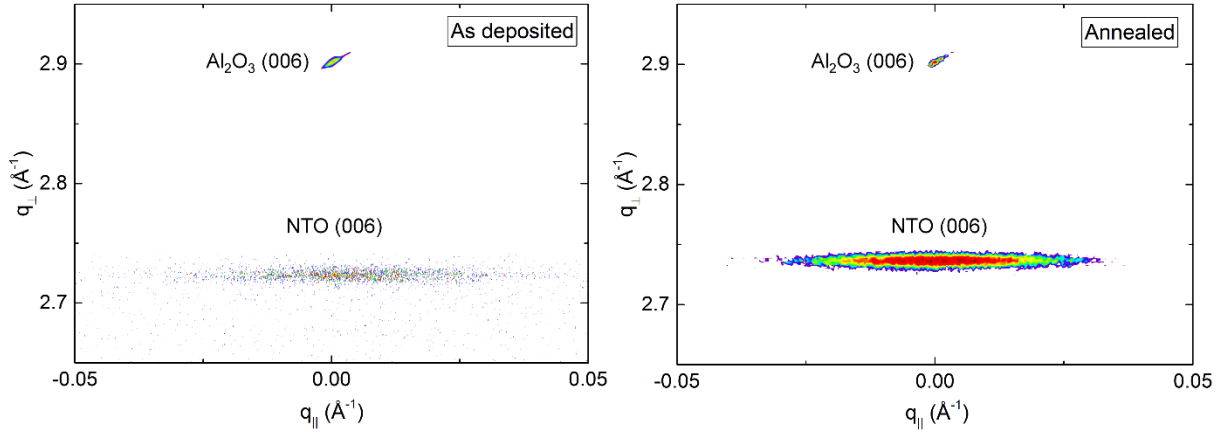
Figure 3: RSM of the symmetrical (006) reflections from NTO and Al₂O₃ as deposited (left) and after annealing (right).

RSM of the (1 0 10) asymmetrical reflections in Figure 4 show the in-plane relaxation of the film upon annealing. For the as deposited film, the position of the NTO (1 0 10) reflection indicated an *a* axis 0.1% shorter than the literature value. Annealing resulted in a 0.1% longer *a* axis, again, compared to the literature value. The FWHM along the Ewald sphere was also reduced upon annealing, from 1.2° to 1.0°.
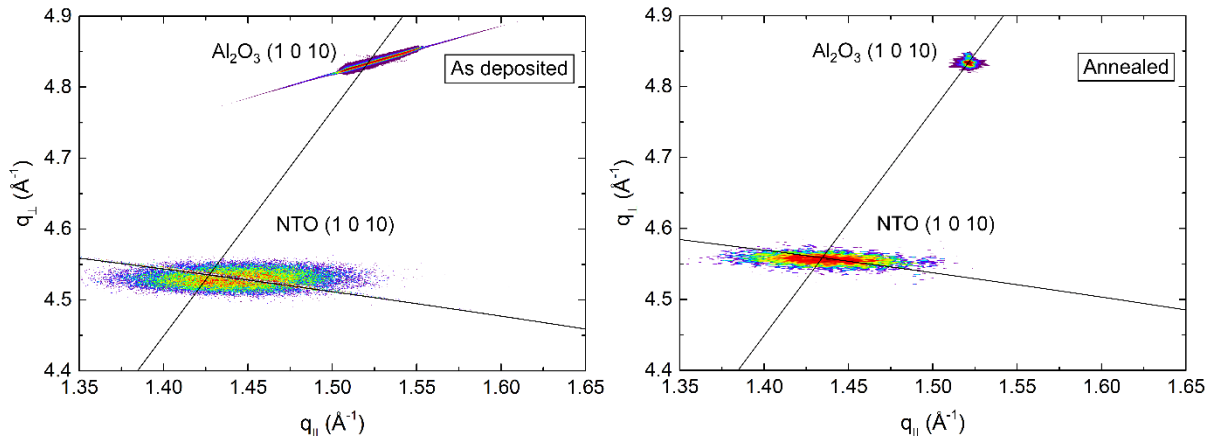
Figure 4: RSM of the asymmetrical (1 0 10) reflections from NTO and Al₂O₃ before (left) and after (right) annealing. The arced lines illustrate the Ewald sphere, while the straight lines are a guide to the eye that intersects the origin and the Al₂O₃ (1 0 10) reflection.

The φ scans of the (1 0 10) reflection revealed a six-fold rotational symmetry (Figure 5), with three of the reflections overlapping those from the substrate, and the other three shifted by 60°.
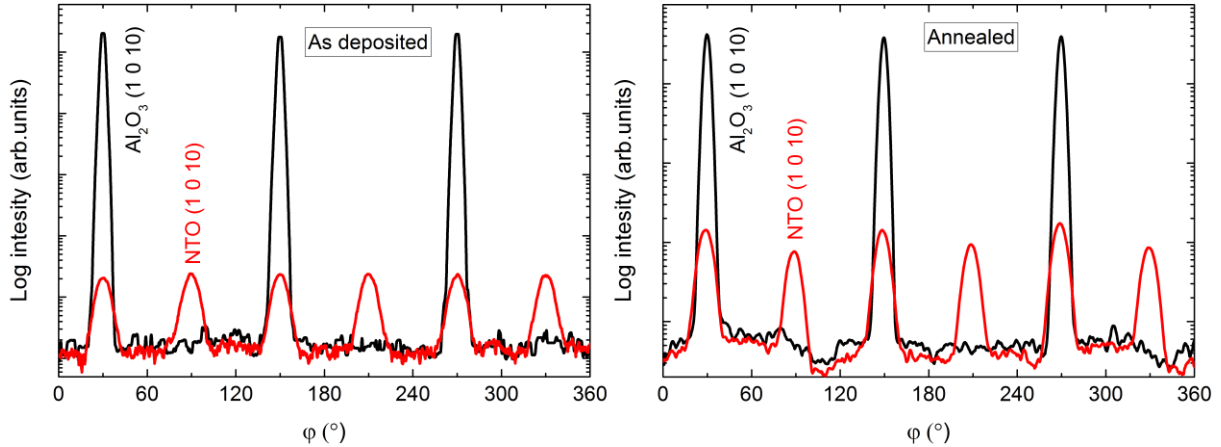
Figure 5: *φ* scan of the (1 0 10) reflections from NTO (red lines) and Al_2O_3 (black lines) as deposited (left) and after annealing (right).

AFM investigations of the as deposited films showed a very flat surface, with a root mean square (rms) roughness of only 0.21 nm (Figure 6). After annealing, the roughness increased only slightly, to 0.24 nm. No recognizable facets could be identified, but rather many smaller, round crystallites, possibly convoluted by the AFM tip itself.
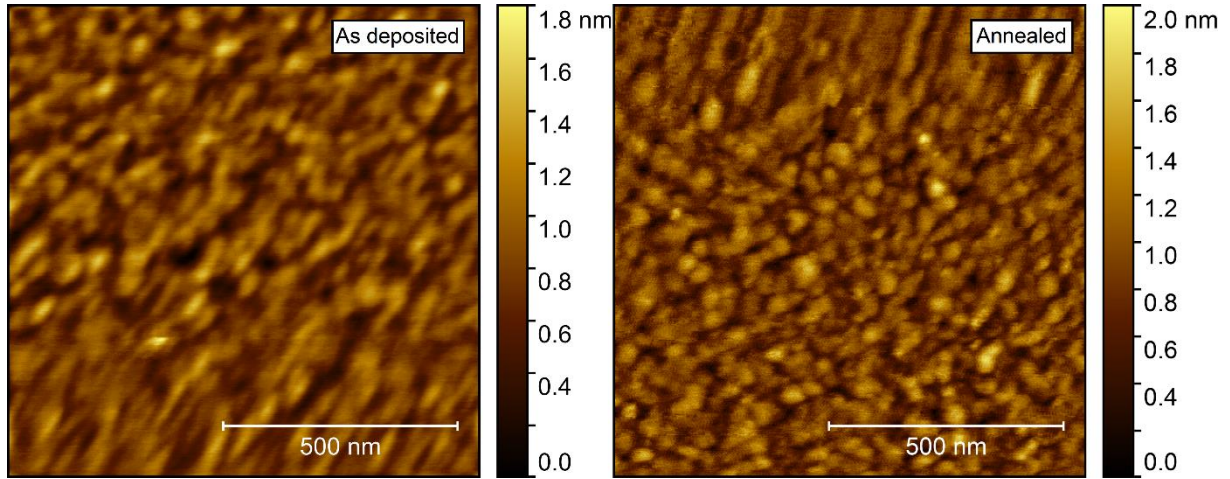
Figure 6: AFM images of NTO deposited on Al_2O_3(001). As deposited rms = 0.21 nm (left), increasing to rms = 0.24 nm after annealing (right).

On LaAlO₃(100)

LAO has a distorted perovskite crystal structure, with space group symmetry *R−3c*, the same as the high temperature disordered phase of NTO. Compared to NTO, LAO (PDF 00-031-0022 [25]) has a longer *a* axis (5.36 Å vs. 5.03 Å), but a shorter *c* axis (13.11 Å vs. 13.79 Å). However, LAO can also be represented as a pseudocubic structure, with angles that are less than 0.1° off from 90°. In this regard, the unit cell space group is *Pm−3m*, and *a* = 3.79 Å.

Hereof comes the given orientation of the substrates used in this work: LAO(100), which is the same as LAO(012) in the rhombohedral system. The orientation and reflections of LAO in this text refer to the pseudocubic system, unless otherwise stated. There is no pseudocubic symmetry for NTO similar to LAO, given the same orientation as for LAO, with pseudocubic(100) = rhombohedral(012). The closest equivalent is a unit cell with dimensions $a = 5.44$ Å; $b = 5.03$ Å; $c = 3.66$ Å, and angles $\alpha = 90°$; $\beta = 83.1°$; $\gamma = 90°$.

NTO films deposited on LAO(100) substrates had two preferred orientations: $(00l)$ and $(h0h)$ (Figure 7). Reflections from the $(h0h)$ orientation were considerably weaker and broader than from the $(00l)$ orientation. In addition, annealing increased the intensity and reduced the FWHM for all reflections, with $(h0h)$ reflections remaining distinctly broader.
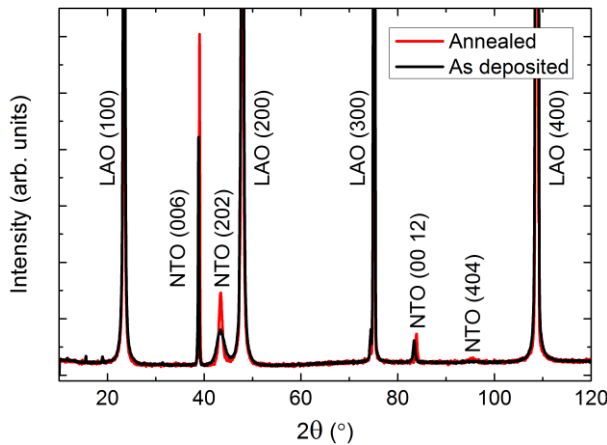
Figure 7: XRD of NTO deposited on LAO(100), as deposited (black line) and after annealing (red line).

RSM of the (006) reflection revealed a small shift in $q_\perp$ direction upon annealing, with the length of the c axis being 0.8% and 0.2% larger than the literature value before and after annealing, respectively (Figure 8). Annealing also reduced the FWHM from 2.3° to 2.1°, along $q_\parallel$. Extensive efforts were made to collect decent RSMs of the $(h0h)$ reflection, but with no success. This was also the case for any related asymmetrical reflections.
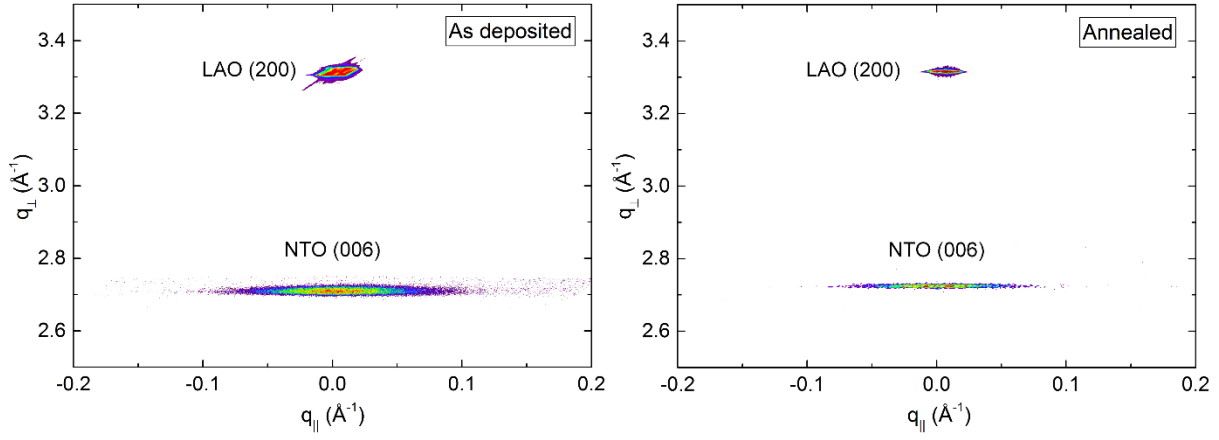
Figure 8: RSM of the symmetrical (006) reflection from NTO along with the LAO (200) reflection, before (left) and after (right) annealing.

From the (00l) related asymmetrical reflection (1 0 10) in Figure 9, the a axis was calculated to be 0.3% and 0.5% shorter compared to the literature value before and after annealing, respectively. The shift along $q_\perp$ corresponded well with the compression of the c axis upon annealing, and a distinct reduction of the FWHM along the Ewald sphere from 1.5° to 1.1° was also observed.
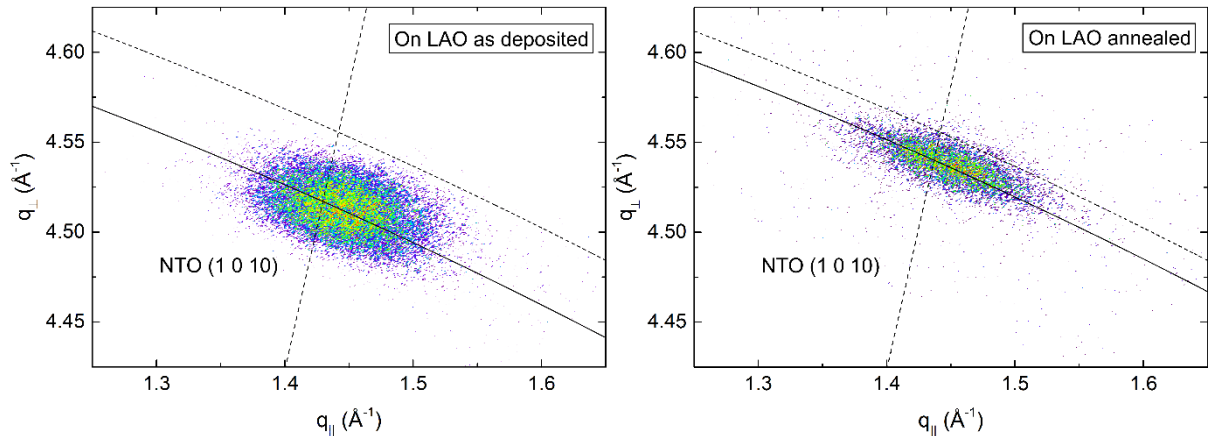
Figure 9: RSM of the asymmetrical NTO (1 0 10) reflection from a film deposited on LAO(100), as deposited (left) and after annealing (right). The solid arced lines illustrate the curvature of the Ewald sphere. The intersection of the dashed lines mark the theoretical position of the NTO (1 0 10) reflection.

The φ scans revealed a twelve-fold symmetry out-of-phase with the four-fold symmetry of the selected substrate reflection (Figure 10). Annealing did not affect the symmetry, and the only observable change was a slight increase in intensity.
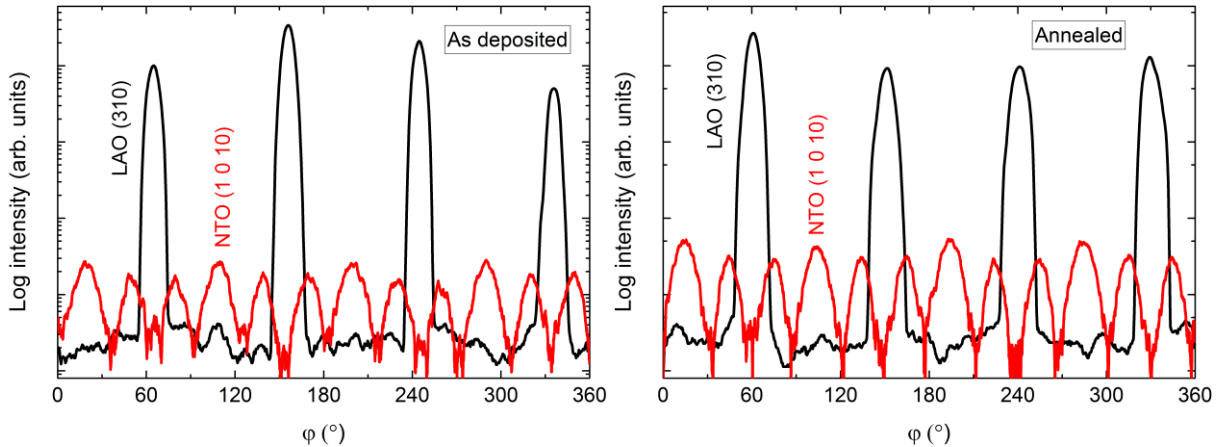
Figure 10: φ scans of the NTO (1 0 10) reflection (red line) along with the LAO (310) reflection (black line), before (left) and after (right) annealing.

Annealing induced no apparent change in the topography, as observed by AFM (Figure 11). The surface was comprised of spherical-like crystallites, similar to the films deposited on Al_2O_3, but with a larger rms roughness, at 0.9–1.0 nm.
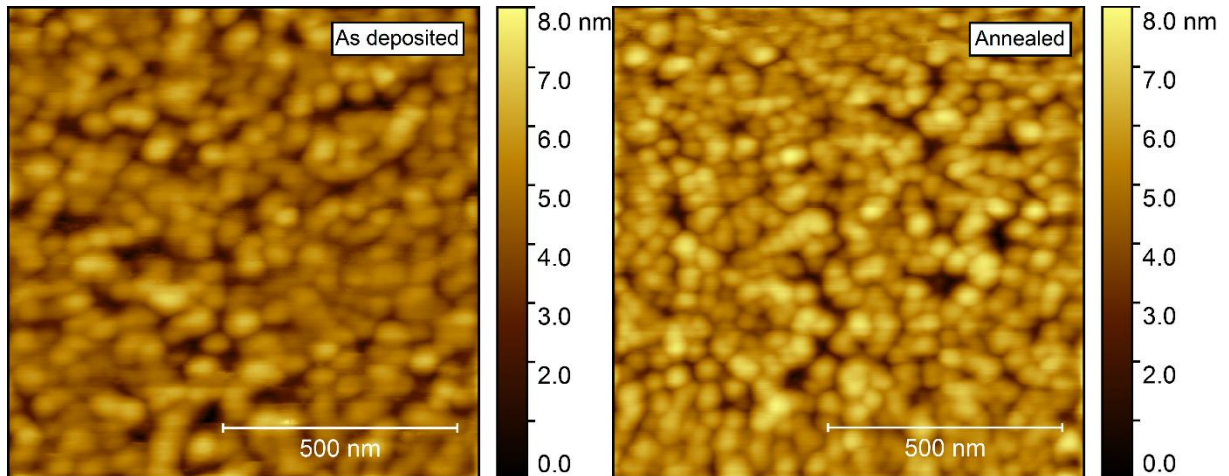

Figure 11: AFM images of NTO deposited on LAO(100). As deposited rms = 0.9 nm (left). Annealed rms = 1.0 nm (right).

On SrTiO₃(100)

The pseudocubic representation of LAO is closely related to STO, a perovskite structure with *Pm*3*m* symmetry. The cell parameters of STO are slightly larger compared to LAO, with *a* = 3.90 Å (PDF 00-035-0734 [26]).

Depositions on STO(100) resulted in (*h*0*h*) orientated NTO (Figure 12**Error! Reference source not found.**). The intensity of the reflections were higher compared to the same

reflections on LAO, but the relative increase upon annealing was smaller, indicating an initial higher crystallinity of the as deposited film. The FWHM values were very similar for the two systems, both as deposited and after annealing.
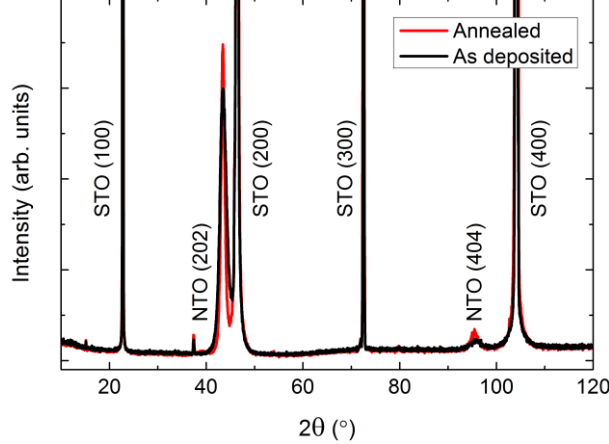
Figure 12: XRD of (*h0h*) oriented NTO deposited on STO(100). A slight increase in intensity was observed after annealing (red line), compared to the as deposited film (black line).

RSM of the symmetrical (202) reflection of as deposited and annealed films revealed a reduction in the FWHM from 3.4° to 2.5° along $q_\parallel$ upon annealing (Figure 13). A small shift in the $q_\perp$ direction was also observed, with the calculated c axis being 0.8% (as deposited) and 0.5% (annealed) larger than the literature value.
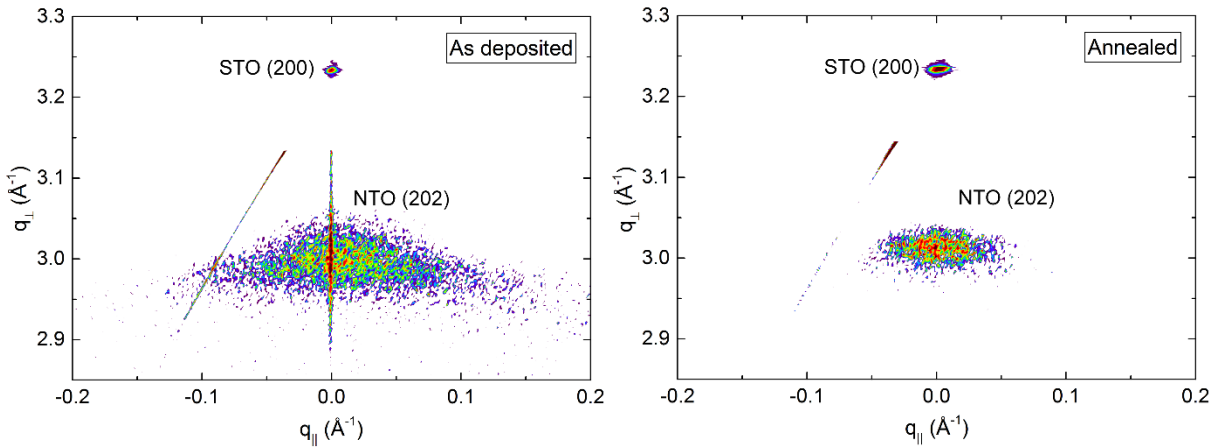
Figure 13: RSM of the symmetrical NTO (202) reflection along with STO (200) before (left) and after (right) annealing. Detector streaking is visible in both RSMs, with the as deposited data also showing wavelength streaking through the film reflection.

Conversely, investigations of the asymmetrical reflection showed a clear shift along the Ewald sphere (Figure 14), indicating a pronounced relaxation of the structure. However, a low intensity reflection closer to the relaxed position was visible for the as deposited film as well,

indicating that the initial strain did not persist throughout the as deposited film. A reduction in FWHM along the Ewald sphere was observed upon annealing, from 1.6° to 0.8°. As the NTO(220) reflection was very close to the edge of the accessible region of the instrument, and possibly out of reach for the as deposited film, these values are very uncertain. This is also reflected in the calculated a axis values. Compared to literature, the a axis was 5.0% and 1.5% smaller for the as deposited and annealed films, respectively.
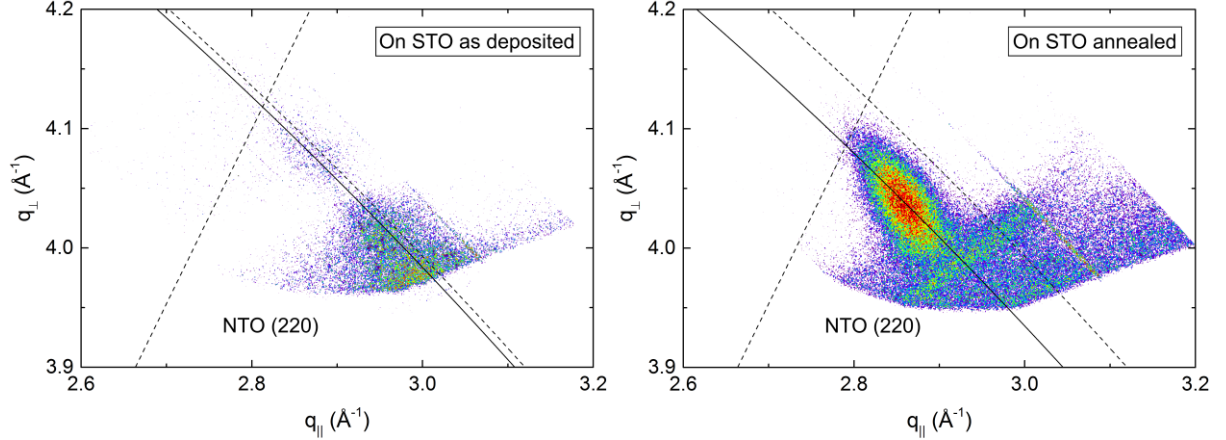
Figure 14: RSM of the asymmetrical (220) reflection from NTO on STO(100) as deposited (left) and after annealing (right). The solid arced lines illustrate the curvature of the Ewald sphere. The intersection of the dashed lines mark the theoretical position of the NTO (220) reflection.

The φ scan of the asymmetrical (220) reflection displayed a four-fold symmetry out-of-phase with the selected asymmetrical reflection from the substrate (Figure 15). Again, a slight increase in intensity was observed upon annealing.
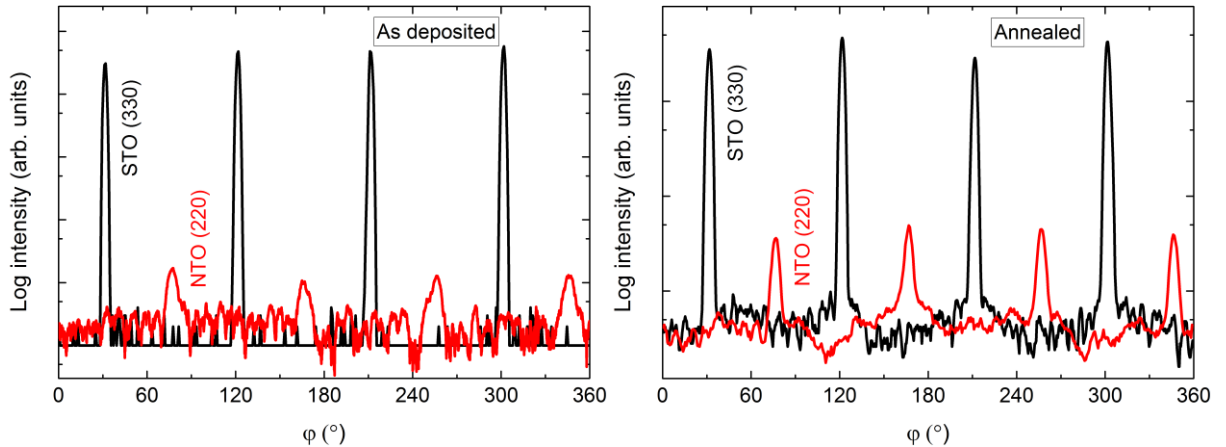

Figure 15: φ scans of the (220) reflection from NTO (red line) superimposed on the φ scan of the STO (330) reflection (black line) before (left) and after annealing (right).

Compared to films deposited on Al$_2$O$_3$, AFM of films deposited on STO revealed a considerably higher rms roughness, increasing from 1.5 to 1.7 nm upon annealing (Figure 16). As for the films deposited on Al$_2$O$_3$, the surface consisted of numerous round crystallites with no recognizable facets.
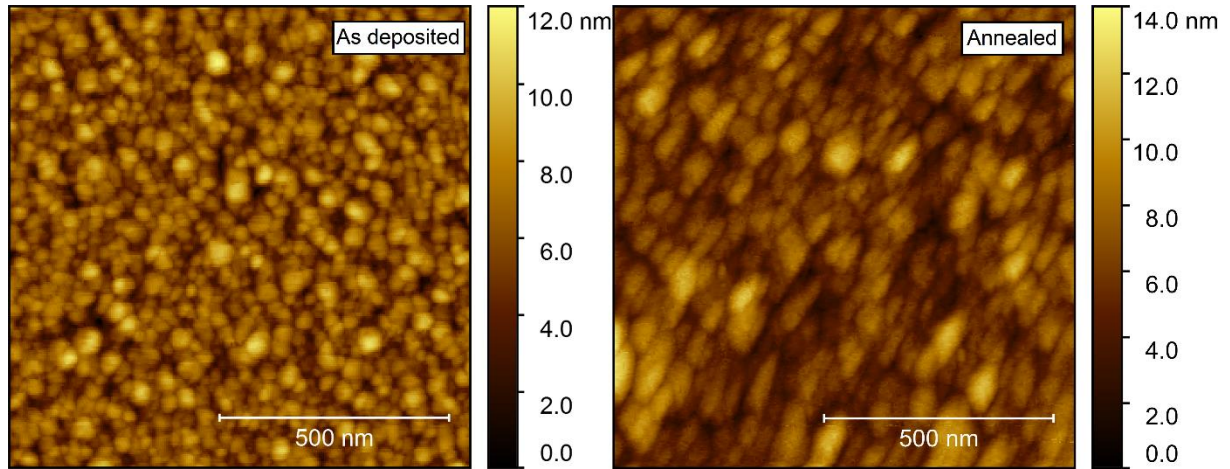

Figure 16: AFM images of NTO on STO(100), with rms roughness of 1.5 nm as deposited (left) and 1.7 nm after annealing (right).

On MgO(100)

MgO also has a cubic structure (*Fm−3m*), but with larger unit cell parameters (*a* = 4.21 Å, PDF 00-045-0946 [27]) compared to STO. As on STO, the deposited film was (*h*0*h*) oriented (Figure

17). Since the *d* spacing of NTO(*h0h*) and MgO(*h00*) are almost the same a diffractogram of the pure MgO substrate is shown in Figure 17.
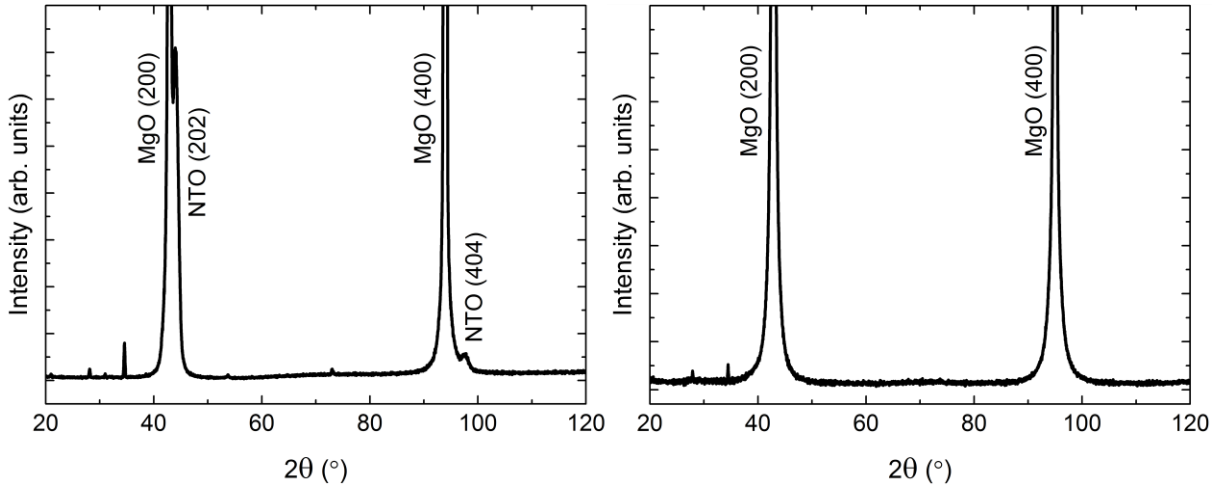

Figure 17: XRD of NTO on MgO(100) (left), showing the (*h0h*) orientation of the film. A diffractogram of an uncoated MgO(100) substrate is shown to the right for comparison. Minor substrate artefacts are visible at $2\theta = 28°, 34°, 54°$ and $73°$.

RSM of the symmetrical (202) reflection disclosed a very sharp peak with FWHM along $q_{\parallel}$ of only $0.2°$ (Figure 18). The position of the reflection along $q_{\perp}$ corresponds to a unit cell with a calculated *c* axis 1.2% shorter than the literature value.
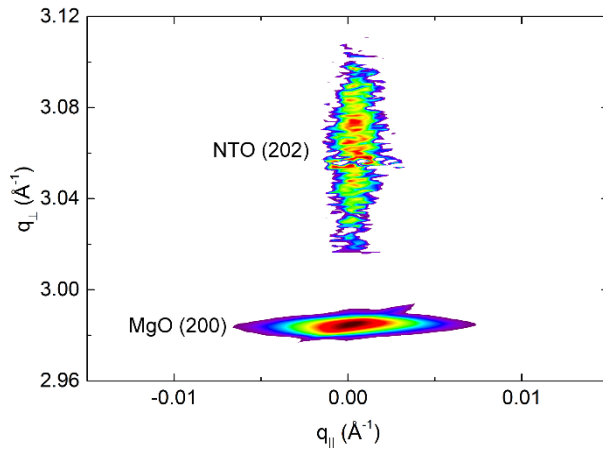

Figure 18: RSM of the symmetrical NTO (202) reflection as deposited, along with the MgO (200) reflection.

The position of the asymmetrical reflection (220) (Figure 19) was close to that observed for the annealed film deposited on STO (assumed to be relaxed). The FWHM along the Ewald sphere,

at 1.5°, was slightly smaller than for as deposited NTO on STO. The calculated *a* axis was 1.2% shorter compared to the literature value.
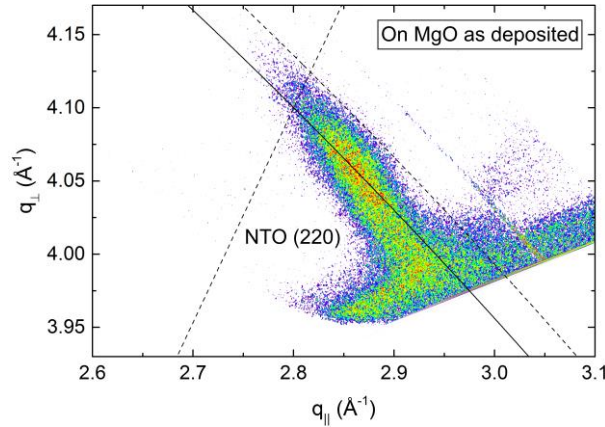

Figure 19: RSM of the asymmetrical NTO (220) reflection, as deposited on MgO(100). The Ewald sphere is illustrated as an arced solid line. The intersection of the dashed lines mark the theoretical position of the NTO (220) reflection.

In the same manner as for films on STO, the φ scan revealed a four-fold rotational symmetry of the film (Figure 20), but this time in-phase with the selected substrate reflection.
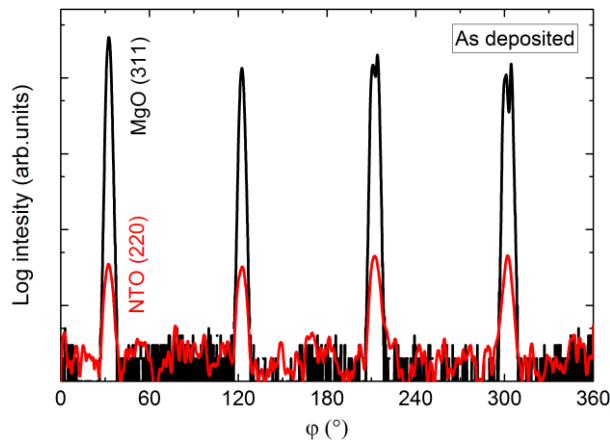

Figure 20: φ scan of the NTO (220) reflections (red line) superimposed on the φ scan of the MgO (311) reflections (black line).

Compared to the films deposited on other substrates, the surface topography of films grown on MgO was rather different. AFM scans revealed clear protrusions from a flatter bed of smaller crystals (Figure 21), with the flatter areas resembling the surfaces observed on the other substrates. The larger platelets, or flattened crystals, had no obvious collective orientation, and the rms roughness of the scanned area was 1.9 nm.
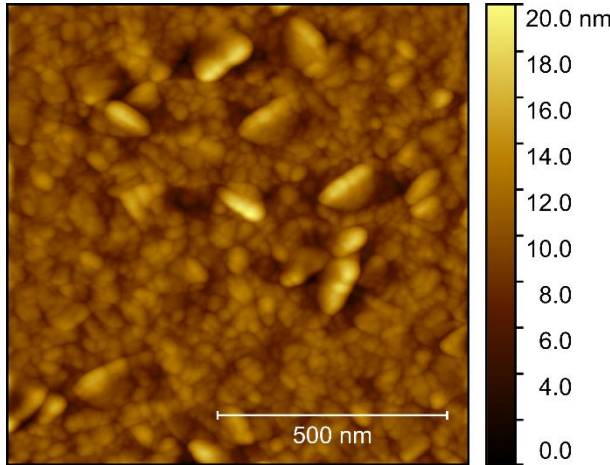
Figure 21: AFM image of NTO as deposited on MgO(100), with rms roughness = 1.9 nm.

An overview of the results is given in Table 1.

Table 1: Summary of results for NTO films deposited on various single crystal substrates. AD and Ann refers to as deposited and annealed samples, respectively. The c and a values were calculated from the positions of the symmetrical and asymmetrical reflections in the RSMs, respectively, and are relative to the literature values. The ω_{FWHM} values are the full width at half maximum of Gauss functions fitted to the RSMs of symmetrical reflections along $q_{\parallel}$. The ES_{FWHM} values are the full width at half maximum of Gauss functions fitted to the asymmetrical reflections along the Ewald sphere. The φ values are the number of film reflections in the φ scans. Root mean square (rms) roughness values are from the built in analysis tool in the Gwyddion software.

Substrate	Film	State	c (%)	ω_{FWHM} (°)	a (%)	ES_{FWHM} (°)	φ refl.	rms (nm)
Al$_2$O$_3$(001)	(00l)	AD	0.36	1.03	−0.13	1.16	6	0.21
		Ann	−0.11	0.67	0.09	0.96		0.24
LAO(100)	(00l)	AD	0.81	2.26	−0.29	1.49	12	0.90
		Ann	0.24	2.10	−0.45	1.06		0.96
STO(100)	(h0h)	AD	0.84	3.41	−5.01	1.61	4	1.50
		Ann	0.47	2.50	−1.52	0.77		1.71
MgO(100)	(h0h)	AD	−1.22	0.22	−1.20	1.46	4	1.93

4. Discussion

On Al$_2$O$_3$

Our previous report on growth of NTO [21] showed that films deposited on Si(100) were (00l) oriented, with the orientation assumed to be from an inherent preferred growth direction. Annealing of those samples improved the crystallinity, but did not alter the symmetry, as seen

by the absence of the (003) and (009) reflections. On Al_2O_3, the same $R-3c$ symmetry is observed for as deposited films, but annealing induces ordering of the structure, resulting in the $R-3$ symmetry. For NTO, the disordered phase is only thermodynamically stable at temperatures above 1292 °C [7, 8, 28], and has not previously been obtained at room temperature by any other technique. The present case is thus yet another example of the ability of ALD to produce films with metastable phases, given careful selection of substrates and temperature treatment [29].

The mismatch factor, f, is usually given as $100\% \cdot (a_s - a_f)/a_s$, where a_s and a_f denotes the lattice parameters of the substrate and the film, respectively. With a mismatch (f) of −6.2% for the [001] direction, Al_2O_3 is an acceptable candidate with regards to epitaxial growth of NTO. However, perhaps a more relevant way of looking at film-substrate mismatch would be to compare the oxygen lattices at the interface. This gives a mismatch of −3.0%, when comparing the average O–O distances for the (001) surface of Al_2O_3 and NTO. The negative value of the mismatch indicates that the film will experience a compressive strain from the substrate. Indeed, the as deposited film has a shorter a axis, compared to the literature value. At the same time, the c axis is longer, due to the Poisson effect. Annealing relaxes the film, both in the basal plane and in the (00l) direction, with only 0.1% strain left.

The broadening of the symmetrical NTO (006) reflection along $q_{\parallel}$ and the asymmetrical NTO (1 0 10) reflection along the Ewald sphere indicates that the film consist of numerous crystallites with somewhat random texture. This could stem from abundant nucleation early on in the deposition, and that the numerous crystals grow as narrow pillars throughout the film. The resulting film would have many grain boundaries and a surface with many smaller crystallites, which consequentially results in a low roughness, as indeed observed by AFM.

With an epitaxial relationship between substrate and film, one might expect the same multiplicity of reflections in the φ scan. However, as presented above, the NTO film has twice the number of reflections compared to Al_2O_3. We hypothesize that this comes from atomic steps on the substrate surface revealing trigonal surface terminations rotated at 60° from each other (Figure 22), as also seen for growth of $CaCO_3$ on Al_2O_3(001) [30]. The apparent six-fold rotational symmetry of the NTO film stem from two sets of crystallites, each with three-fold rotational symmetry, superimposed on each other. This feature also increases the likelihood of high nucleation density. The heteroepitaxial film is both out-of- and in-plane oriented, even

though the number of reflections in the φ scan is different for the film and the substrate, resulting in the film‖substrate epitaxial relationship: NTO(001)[100]‖Al$_2$O$_3$(001)[100].
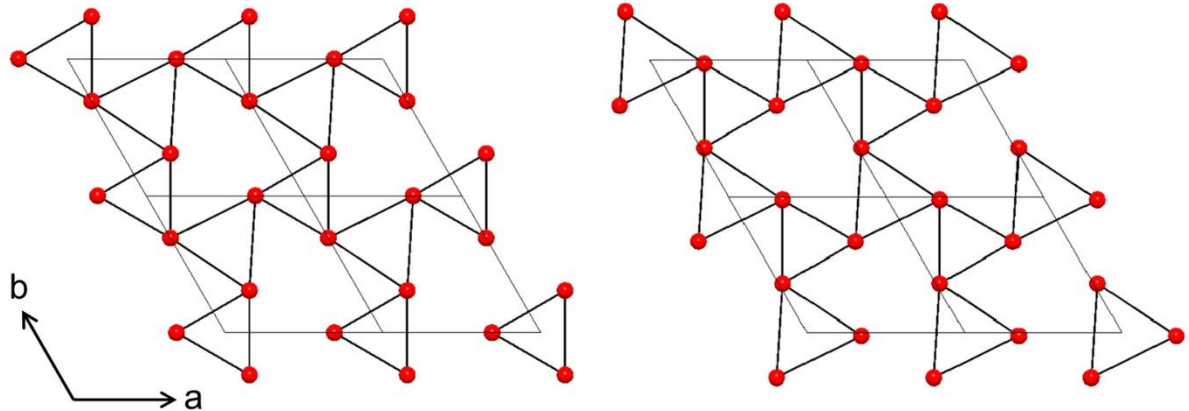

Figure 22: Oxygen lattices of the (001) plane in Al$_2$O$_3$, viewed along the c axis, showing the 60° rotation between the top (left) and bottom (right) of octahedrons around Al^{3+}. The four grey diamonds in each cartoon indicate the edges of four unit cells.

On LAO

While the epitaxial relationship for NTO‖Al$_2$O$_3$ is easy to envision, the same is not true for NTO‖LAO. There are no obvious lattice matches between either of the two preferred orientations of the deposited film and the (100) surface of the LAO substrate. In addition, it is hard to untangle the nature of the ($h0h$) orientation, as it was impossible to map any related asymmetrical reflections.

With two preferred orientations the film can grow in one of three ways: either (a) the film consists of a layer with (00l) orientation close to the substrate and a ($h0h$) oriented layer on top, (b) the layers in (a) are inverted, or (c) there is a mix of crystallites with both orientations and no layered structure (Figure 23).
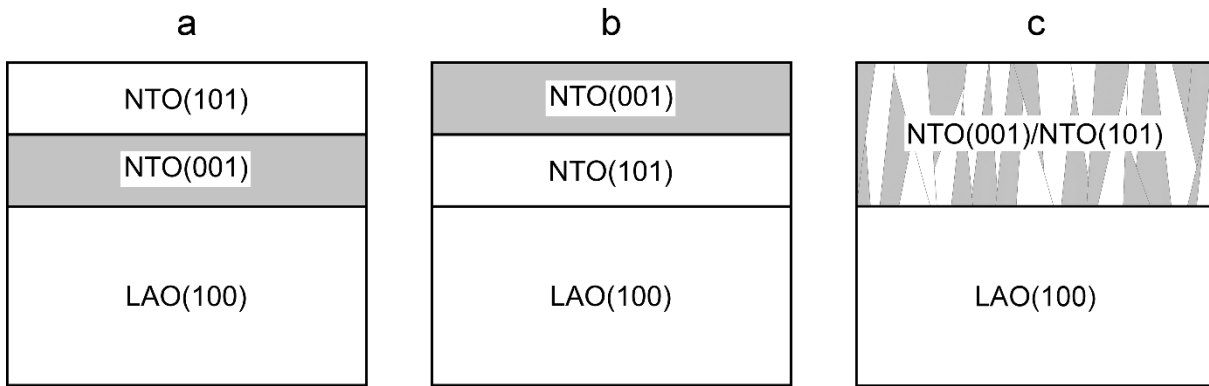
Figure 23: Cartoon of possible constellations for the two orientations observed in NTO on LAO.

We are unfortunately unable to conclude which constellation is the most probable, even with basis in the observed variations in texture and surface roughness of the films obtained in this work (see supplementary S3).

The twelve NTO (1 0 10) reflections observed in the φ scan can be explained similarly to NTO on Al_2O_3. That is, the film does not actually have a twelve-fold rotational symmetry, but four sets of crystallites—each set in-plane oriented, with a three-fold rotational symmetry. The orientation of the sets of crystallites are shifted by 90° with respect to each other, resulting in twelve reflections in the φ scan. Both the substrate and a NTO($h0h$) layer could facilitate this. In any case, it is clear that the nucleation density is high, as the different sets of NTO($00l$) crystallites must have nucleated separately. If the NTO($00l$) crystallites nucleated on the LAO(100) surface, as in constellation (a) or (c), the epitaxial relationship with the substrate would be: NTO(001)[100]‖LAO(100)⟨010⟩, with ⟨010⟩ representing the four identical (010) directions on the LAO(100) surface.

On STO

As with NTO on LAO, there are no obvious lattice matches between the film and the substrate. Still, the deposited film shows an in-plane ($h0h$) orientation. The four asymmetrical reflections from the film are perfectly out of phase with the four reflections from the substrate. This means that the direction of the NTO (220) scattering vector, projected down to the substrate surface, is 45° off from the same projection of the STO (330) scattering vector. Figure 24 shows the STO(100) and NTO(101) oxygen lattices, with the film lattice rotated according to the projections of the asymmetrical scattering vectors (See Supporting Information for details). The average O–O distance of the film lattice perpendicular to the projection of the NTO (220)

direction is close to the oxygen spacing of STO(100). The mismatch along one row of NTO oxygen atoms is only −0.6%. However, when regarding the direction along the NTO (220) scattering vector the mismatch between every second layer of oxygen atoms in STO(100) compared to every layer in NTO(101) is 18.4%.
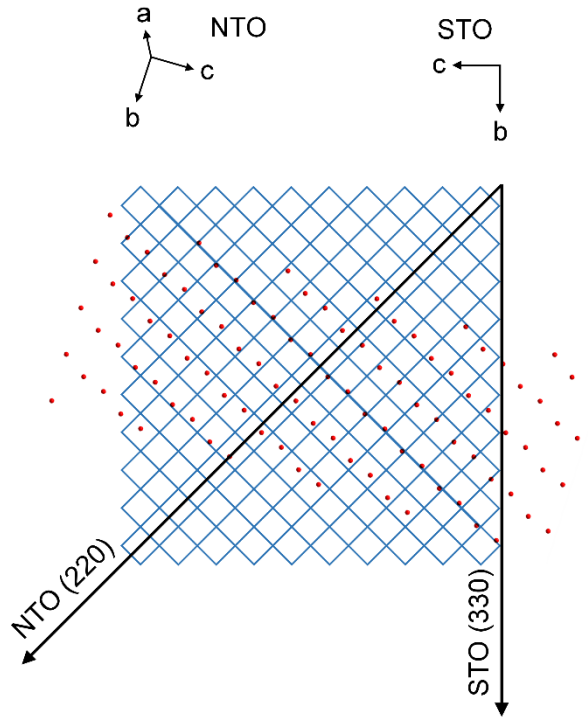

Figure 24: Schematic showing the direction of the STO (330) scattering vector projected down on the oxygen lattice of the STO(100) plane, represented by the corners of the blue matrix. Superimposed is the direction of the NTO (220) scattering vector projected down on the substrate plane, and the oxygen lattice of the NTO(101) plane, represented by red circles.

The number of reflections in the φ scan can be explained in the same way as for NTO on Al$_2$O$_3$ and LAO. A single crystalline, ($h0h$) oriented, NTO film would have only one ($hh0$) reflection in a φ scan. The STO(100) surface has four identical (010) directions: (010), (0$\bar{1}$0). (001) and (00$\bar{1}$), resulting in the four-fold rotational symmetry seen in the φ scan. As the NTO film does not nucleate as a continuous layer, the initial islands of ($h0h$) oriented crystallites do not differentiate between the STO⟨010⟩ directions. Some of the crystallites will be in-plane oriented with the STO(010) direction, and some with the other directions. An epitaxial relationship between film and substrate can thus be described as: NTO(101)[220]∥STO(100)⟨010⟩.

On MgO

Unlike the previous cases, AFM of NTO on MgO show clear signs of bigger crystals. This resonates well with the smaller FWHM of the symmetrical NTO (202) reflection, indicating the

presence of larger and/or less tilted crystallites. However, again, there are no obvious lattice matches between the MgO(100) surface and NTO, neither in general, nor when comparing the NTO(101) oxygen lattice with the oxygen lattice of the MgO(100) surface. Nevertheless, the film is indeed in-plane orientated with the substrate, but in the same manner as for NTO on STO. The φ scan reflections from the substrate and film are overlapping. This means that the direction of the asymmetrical scattering vectors, when projected down on the MgO(100) surface plane, are pointing in the same direction (Figure 25). Regarding a row of NTO oxygen atoms perpendicular to the projection of the MgO (311) scattering direction, there is a seemingly good lattice match for every second layer of oxygen atoms. The calculated mismatch is only 2.4%, but as can be seen from Figure 25, this is only true for selected rows of NTO oxygen atoms. When considering the whole oxygen lattice of NTO it does not correspond very well with the MgO(100) oxygen lattice. Still, the film is in-plane oriented with all the identical MgO⟨011⟩ directions, and the epitaxial relationship is determined to be: NTO(101)[220]∥MgO(100)⟨011⟩.
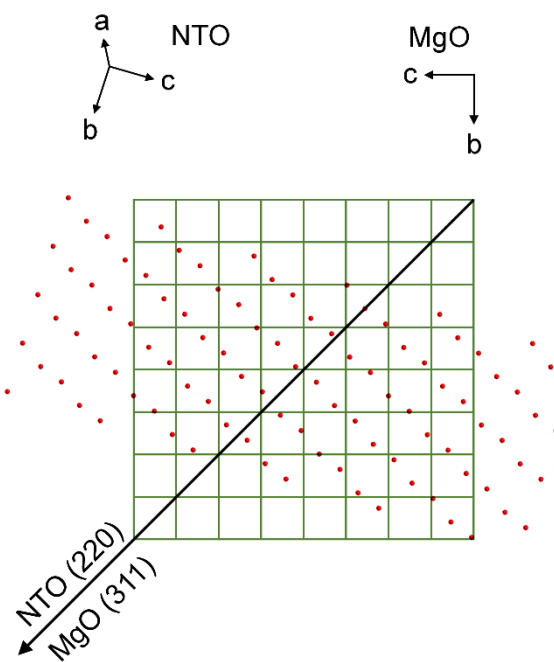

Figure 25: Schematic showing the direction of the MgO (311) scattering vector projected down on the oxygen lattice of the MgO(100) plane, represented by the corners of the green matrix, which also corresponds to the unit cell of MgO. Superimposed is the direction of the NTO (220) scattering vector projected down on the substrate plane, and the oxygen lattice of the NTO(202) plane, represented by red circles.

5. Conclusions

Oriented NTO films were successfully deposited at 250 °C by ALD on various single crystalline substrates. All films had preferred orientations as deposited. Crystallinity improved after annealing at 650 °C for 15 minutes, but did not change the preferred orientations. Interestingly, no signs of the (003) and (009) reflections were observed for the as deposited films. These reflections are not allowed for the $R-3c$ symmetry, where the cations are randomly distributed throughout the structure. On Al_2O_3(001), annealing led to cation ordering, and a change of symmetry to $R-3$, visible by the appearance of mentioned reflections. However, the intensity was much lower, and the FWHM much larger, than for the other (00l) reflections, indicating that only parts of the film underwent cation ordering. AFM revealed very low rms roughnesses of about 0.2 nm, both for the as deposited and annealed film. The film‖substrate epitaxial relationship was determined to be NTO(001)[100]‖Al_2O_3(001)[100]. Depositions on LAO(100) resulted in films with two preferred orientations: NTO($h0h$) and NTO(00l). Annealing improved the crystallinity slightly, but did not alter the orientation of the film nor change the rms roughness significantly, remaining at approximately 1 nm. Films deposited on STO(100) had a NTO(101)[220]‖STO(100)⟨010⟩ epitaxial relationship with the substrate. Annealing resulted in a slight improvement of crystallinity and increase in roughness, from 1.5 to 1.7 nm. On MgO(100), the film‖substrate epitaxial relationship was NTO(101)[220]‖MgO(100)⟨011⟩. Reciprocal space mapping of the symmetrical NTO (202) reflection revealed a very small FWHM along $q_∥$, indicating large crystallites in the film, and/or a very low tilt of the crystallites. No annealing was performed, but AFM investigations displayed larger crystallites protruding from a more flat surface, and the rms roughness was significantly larger than for films on other substrates, at 1.9 nm.

[1] P.-h. Yuan, C.-m. Fan, G.-y. Ding, Y.-f. Wang, X.-c. Zhang, Preparation and photocatalytic properties of ilmenite $NiTiO_3$ powders for degradation of humic acid in water, International Journal of Minerals, Metallurgy, and Materials, 19 (2012) 372-376.
[2] A.A. Tahir, M. Mazhar, M. Hamid, K.G. Wijayantha, K.C. Molloy, Photooxidation of water by $NiTiO_3$ deposited from single source precursor $[Ni_2Ti_2(OEt)_2(μ-OEt)_6(acac)_4]$ by AACVD, Dalton Trans., (2009) 3674-3680.

[3] S.-H. Chuang, M.-L. Hsieh, S.-C. Wu, H.-C. Lin, T.-S. Chao, T.-H. Hou, Fabrication and Characterization of High-k Dielectric Nickel Titanate Thin Films Using a Modified Sol-Gel Method, Journal of the American Ceramic Society, 94 (2011) 250-254.

[4] A.I. Inamdar, J. Kim, B. Jang, D. Kim, H. Im, W. Jung, H. Kim, Memory Conductance Switching in a Ni–Ti–O Compound Thin Film, Japanese Journal of Applied Physics, 51 (2012) 104102.

[5] M.A. Ruiz-Preciado, A. Bulou, M. Makowska-Janusik, A. Gibaud, A. Morales-Acevedo, A. Kassiba, Nickel titanate ($NiTiO_3$) thin films: RF-sputtering synthesis and investigation of related features for photocatalysis, CrystEngComm, 18 (2016) 3229-3236.

[6] C. Xin, Y. Wang, Y. Sui, Y. Wang, X. Wang, K. Zhao, Z. Liu, B. Li, X. Liu, Electronic, magnetic and multiferroic properties of magnetoelectric $NiTiO_3$, Journal of Alloys and Compounds, 613 (2014) 401-406.

[7] K.T. Jacob, V.S. Saji, S.N.S. Reddy, Thermodynamic evidence for order–disorder transition in $NiTiO_3$, The Journal of Chemical Thermodynamics, 39 (2007) 230-235.

[8] M. Lerch, H. Boysen, R. Neder, F. Frey, W. Laqua, Neutron scattering investigation of the high temperature phase transition in nickel titanium oxide ($NiTiO_3$), J. Phys. Chem. Solids, 53 (1992) 1153-1156.

[9] L.C. Ming, Y.-H. Kim, T. Uchida, Y. Wang, M. Rivers, In situ X-ray diffraction study of phase transitions of $FeTiO_3$ at high pressures and temperatures using a large-volume press and synchrotron radiation, American Mineralogist, 91 (2006) 120-126.

[10] T. Varga, T.C. Droubay, M.E. Bowden, P. Nachimuthu, V. Shutthanandan, T.B. Bolin, W.A. Shelton, S.A. Chambers, Epitaxial growth of $NiTiO_3$ with a distorted ilmenite structure, Thin Solid Films, 520 (2012) 5534-5541.

[11] T. Varga, T.C. Droubay, M.E. Bowden, R.J. Colby, S. Manandhar, V. Shutthanandan, D. Hu, B.C. Kabius, E. Apra, W.A. Shelton, S.A. Chambers, Coexistence of weak ferromagnetism and polar lattice distortion in epitaxial $NiTiO_3$ thin films of the $LiNbO_3$-type structure, Journal of Vacuum Science & Technology B: Microelectronics and Nanometer Structures, 31 (2013) 030603.

[12] T. Varga, T.C. Droubay, M.E. Bowden, S.A. Stephens, S. Manandhar, V. Shutthanandan, R.J. Colby, D. Hu, W.A. Shelton, S.A. Chambers, Strain-dependence of the structure and ferroic properties of epitaxial $Ni_{1-x}Ti_{1-y}O_3$ thin films grown on sapphire substrates, Thin Solid Films, 578 (2015) 113-123.

[13] T. Acharya, R.N.P. Choudhary, Structural, Ferroelectric, and Electrical Properties of $NiTiO_3$ Ceramic, Journal of Electronic Materials, 44 (2014) 271-280.

[14] A.R. Phani, S. Santucci, Microwave irradiation as an alternative source for conventional annealing: a study of pure TiO_2, $NiTiO_3$, $CdTiO_3$ thin films by a sol–gel process for electronic applications, Journal of Physics: Condensed Matter, 18 (2006) 6965-6978.

[15] A.R. Phani, S. Santucci, Structural characterization of nickel titanium oxide synthesized by sol–gel spin coating technique, Thin Solid Films, 396 (2001) 1-4.

[16] D.J. Taylor, P.F. Fleig, S.T. Schwab, R.A. Page, Sol-gel derived, nanostructured oxide lubricant coatings, Surf. Coat. Technol., 120-121 (1999) 465-469.

[17] M.R. Mohammadi, D.J. Fray, Mesoporous and nanocrystalline sol–gel derived $NiTiO_3$ at the low temperature: Controlling the structure, size and surface area by Ni:Ti molar ratio, Solid State Sciences, 12 (2010) 1629-1640.

[18] D. Ortiz de Zárate, C. Boissière, D. Grosso, P.-A. Albouy, H. Amenitsch, P. Amoros, C. Sanchez, Preparation of multi-nanocrystalline transition metal oxide (TiO_2–$NiTiO_3$) mesoporous thin films, New J. Chem., 29 (2005) 141-144.

[19] V. Miikkulainen, M. Leskelä, M. Ritala, R.L. Puurunen, Crystallinity of inorganic films grown by atomic layer deposition: Overview and general trends, Journal of Applied Physics, 113 (2013) 021301.

[20] J. Faugier-Tovar, F. Lazar, C. Marichy, C. Brylinski, Influence of the Lattice Mismatch on the Atomic Ordering of ZnO Grown by Atomic Layer Deposition onto Single Crystal Surfaces with Variable Mismatch (InP, GaAs, GaN, SiC), Condensed Matter, 2 (2017) 3.

[21] J.E. Bratvold, H. Fjellvåg, O. Nilsen, Atomic Layer Deposition of oriented nickel titanate (NiTiO$_3$), Applied Surface Science, 311 (2014) 478-483.

[22] UniQuant Version 2 User Manual, in, Omega Data Systems, Veldhoven, The Netherlands, 1994.

[23] R.P. Liferovich, R.H. Mitchell, Rhombohedral ilmenite group nickel titanates with Zn, Mg, and Mn: synthesis and crystal structures, Physics and Chemistry of Minerals, 32 (2005) 442-449.

[24] E.N. Maslen, V.A. Streltsov, N.R. Streltsova, N. Ishizawa, Y. Satow, Synchrotron X-ray Study of the Electron Density in α-Al$_2$O$_3$, Acta Crystallographica Section B, 49 (1993) 973-980.

[25] M. Mizuno, R. Berjoan, J.P. Coutures, M. Foex, Phase diagram of the system Al$_2$O$_3$-La$_2$O$_3$ oxide at elevated temperatures, Yogyo Kyokai Shi, 82 (1974) 631-636.

[26] H.E. Swanson, R.K. Fuyat, G.M. Ugrinic, Standard x-ray diffraction powder patterns, Natl. Bur. Stand. Circ. (U. S.), No. 539 (1954) 73 pp.

[27] A. Kern, R. Doetzer, W. Eysel, Mineralogisch-Petrographisches Inst., Univ. Heidelberg, Germany. ICDD Grant-in-Aid, (1993).

[28] H. Boysen, F. Frey, M. Lerch, T. Vogt, A neutron powder investigation of the high-temperature phase transition in NiTiO$_3$, Z. Kristallogr., 210 (1995) 328-337.

[29] H.H. Sønsteby, J.E. Bratvold, K. Weibye, H. Fjellvåg, O. Nilsen, Phase Control in Thin Films of Layered Cuprates, Chemistry of Materials, (2018).

[30] O. Nilsen, H. Fjellvåg, A. Kjekshus, Growth of calcium carbonate by the atomic layer chemical vapour deposition technique, Thin Solid Films, 450 (2004) 240-247.

Supporting Information

S1. Projection of asymmetrical scattering vectors down to substrate surface plane

Finding the direction of asymmetrical scattering vectors in the substrate surface plane is done by simple trigonometry. The direction of reflections from the substrates are found by disregarding the out-of-plane component. To find the direction of the reflection from the deposited film the unit cell needs to be tilted so that the planes giving symmetrical reflections are parallel with the substrate surface. But firstly, the height of the unit cell is needed. The basal plane of the NTO unit cell can be divided into two equilateral triangles. The height, as shown in Figure S1, can be found by using Equation 1.

$$h = b \cdot \sin 60° = 5.03 \text{ Å} \cdot sin60° = 4.36 \text{ Å} \qquad \text{Equation 1}$$
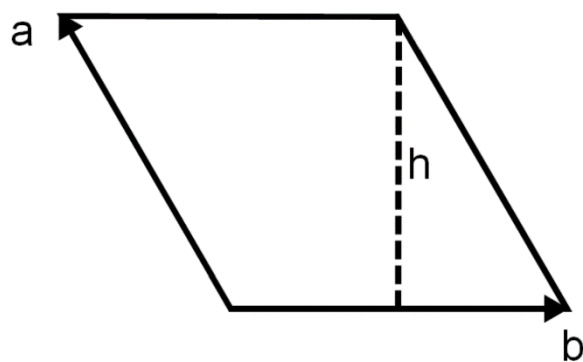

Figure S1: Height of the unit cell. Notice that the height intersect at the midpoint on the b axis.

The NTO($h0h$) planes must be parallel to the substrate surface. This can be done by fixing the b axis of the NTO unit cell along the b axis of the substrate unit cell and tilting the NTO unit cell (Figure S2). The angle of the tilt is given by Equation 2.

$$\alpha = \text{atan}\frac{h}{c} = \text{atan}\frac{4.36 \text{ Å}}{13.79 \text{ Å}} = 17.55° \qquad \text{Equation 2}$$
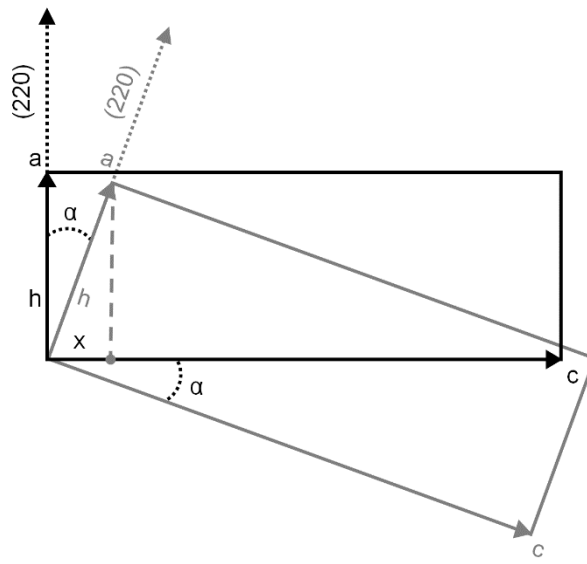
Figure S2: The NTO unit cell before (black) and after (grey) tilt to align the NTO(101) plane parallel to the substrate surface.

Next, the *x* in Figure S2 is found by using Equation 3:

$$x = h \cdot \sin \alpha = 4.36 \text{ Å} \cdot \sin 17.55° = 1.31 \text{ Å} \qquad \text{Equation 3}$$

Lastly, the angle between the *b* axes of the unit cells, as shown in Figure S3, can be found from Equation 4:

$$\omega = \text{atan} \frac{x}{\frac{b}{2}} = \text{atan} \frac{1.31 \text{ Å}}{2.515 \text{ Å}} = 27.51° \qquad \text{Equation 4}$$
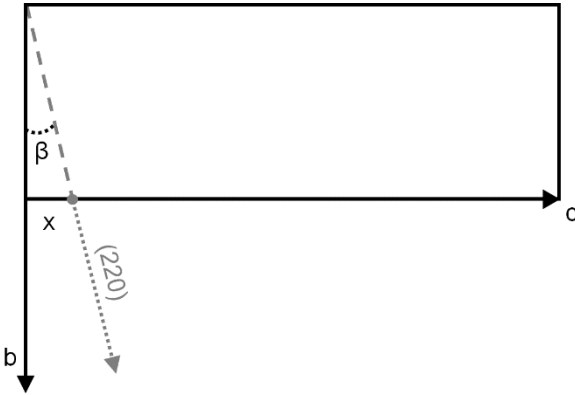
Figure S3: Direction of the NTO (220) scattering vector projected down on the substrate surface plane. The unit cell at the starting point is marked out in black as a reference point.

The angle between the b axis and the projected direction of the NTO (220) scattering vector can now be used to rotate the NTO(101) oxygen lattice in-plane to align it according to the φ scan. For the NTO‖STO case, the investigated asymmetrical reflections lie 45° apart. This means that the oxygen lattice needs to be rotated approximately 17.5° (45°−27.55°), as this is the rotation needed to get a 45° separation between the NTO (220) and STO (330) projections. In the NTO‖MgO case, the asymmetrical reflections have the same rotational direction, but the projected direction of the MgO (311) reflection is 45° off from the b axis. Thus, the rotation of the NTO(101) oxygen lattice is the same as for NTO on STO.

S2. Calculated cell parameters from reciprocal space maps

Substrate	Film orient.	State	c (Å)	a (Å)
$Al_2O_3(001)$	$(00l)$	AD	13.842	5.026
		Ann	13.777	5.037
LAO(100)	$(00l)$	AD	13.905	5.017
		Ann	13.826	5.009
STO(100)	$(h0h)$	AD	13.908	4.780
		Ann	13.857	4.956
MgO(100)	$(h0h)$	AD	13.624	4.972

S3. NTO on LAO

From the FWHM (along $q_{\parallel}$) of the symmetrical reflections it is clear that the (006) reflection is significantly broader than for NTO on Al_2O_3, while the (202) reflection is slightly broader than for NTO on STO. This means that both orientations have smaller crystallites and/or that the crystallites are tilted more than for the respective films with only one orientation. The surface roughness value for NTO on LAO is halfway between the values for films deposited on Al_2O_3 and STO. For comparison, the two different orientations are assumed to have similar surface roughnesses as on other substrates, regardless of the layer beneath. The roughness value of NTO on LAO should then be larger than what is observed if the film is ($h0h$) terminated. Conversely, if the film surface is ($00l$) terminated, a lower roughness value is expected. However, for crystalline films, the surface roughness is usually also dependent on the film thickness. That is, a thicker, crystalline, film will have a higher roughness than a thinner one. In this respect, the film on LAO could very well have constellation (a). The films on LAO and STO are from the same deposition and hence their overall thickness is the same. A terminating ($h0h$) layer would therefore have to be thinner than the film on STO. However, the surface roughness of crystalline ALD films is indeed affected by the layer beneath, and the assumption above is thus void. If the film has constellation (b), the terminating ($00l$) layer grows on a much rougher surface than a polished substrate. This is expected to yield a higher roughness than for NTO on Al_2O_3. Finally, constellation (c) might also be probable, as the roughness value is almost exactly between the values found for films on STO and Al_2O_3. Without more information on the ($h0h$) orientation, it is hard to determine which of the proposed constellation the film actually has.

Paper III

An iron(II) diketonate–diamine complex as precursor for thin film fabrication by atomic layer deposition

Jon E. Bratvold, Giorgio Carraro, Davide Barreca and Ola Nilsen

An iron(II) diketonate–diamine complex as precursor for thin film fabrication by atomic layer deposition

Jon E. Bratvold [a],[*], Giorgio Carraro [b], Davide Barreca [c], Ola Nilsen [a]

[a] Centre for Materials Science and Nanotechnology (SMN)/Department of Chemistry, University of Oslo, PO Box 1033, Blindern, N-0315 Oslo, Norway
[b] Department of Chemistry, University of Padova and INSTM, via F. Marzolo 1, I-35131 Padova, Italy
[c] CNR-IENI and INSTM, Department of Chemistry, University of Padova, via F. Marzolo 1, I-35131 Padova, Italy

ARTICLE INFO

ABSTRACT

A new divalent Fe precursor has been explored for deposition of iron-containing thin films by atomic layer deposition and molecular layer deposition (ALD/MLD). The Fe(II) β-diketonate-diamine complex, Fe(hfa)$_2$TMEDA, (hfa = 1,1,1,5,5,5-hexafluoro-2,4-pentanedionate, TMEDA = N,N,N',N'-tetramethylethylenediamine) can be handled in air, and sublimation at 60 °C ensures a satisfactory vaporization rate. The reactivity of the precursor does not allow for direct reaction with water as co-reactant. Nevertheless, it reacts with carboxylic acids, resulting in organic–inorganic hybrid materials, and with ozone, yielding α-Fe$_2$O$_3$. The divalent oxidation state of iron was maintained during deposition when oxalic acid was used as co-reactant, demonstrating the first preservation of Fe(II) from precursor to film during an MLD process. A self-saturating growth mode was proven by in situ quartz crystal microbalance (QCM) measurements, and the films were further characterized by grazing incidence X-ray diffraction (GIXRD), Fourier transform infrared spectroscopy (FTIR), and X-ray photoelectron spectroscopy (XPS).

© 2015 Elsevier B.V. All rights reserved.

1. Introduction

Although used for thousands of years, iron-containing compounds are still of great importance for technological applications. The magnetic and electronic properties exhibited by various iron oxides make them strategic candidates for use in biomedicine, lithium ion batteries, photoelectrochemical hydrogen production, and spintronic devices [1–4]. Particularly interesting with respect to spintronics are solid solutions of hematite–ilmenite, α-Fe$_2$O$_3$-FeTiO$_3$. Both naturally occurring minerals are antiferromagnetic insulators, but when combined in a layered structure they exhibit very stable magnetization and large exchange bias due to a phenomenon known as lamellar magnetism [5,6]. With the coexistence of ferrimagnetic and semiconducting properties [7–9], these systems show great promise for applications in electronics and spintronics [10]. The end-uses require materials in form of thin films/nano-laminates with precise thicknesses, possibly covering complex high aspect ratio surfaces. To this regard, a viable and attractive option is offered by atomic layer deposition (ALD), which enables the tailored growth of ultra-thin, conformal and pin-hole free films with controlled properties even on porous structures.

This technique is already being employed on an industrial scale to fabricate microelectronic devices [11,12]. Although versatile, ALD is usually limited to deposition of either fully reduced phases, i.e. metals, or fully oxidized materials. The possibility to deposit intermediate oxidation states by ALD enables the preparation of a wide range of phases with tailored properties. With this in mind, we have investigated the reactivity of a new divalent iron-containing compound as precursor for ALD and molecular layer deposition (MLD).

Iron oxide films deposited by ALD were first prepared more than 10 years ago, and since then a variety of different precursors have been utilized. Pure α-Fe$_2$O$_3$ films have been obtained starting from various Fe(III) complexes, including Fe(acac)$_3$ (Hacac = 2,4-pentanedione) combined with O$_2$ [13], Fe(thd)$_3$ (Hthd = 2,2,6,6-tetramethyl-3,5-heptanedione) with O$_3$ [14,15], as well as iron(III) *tert*-butoxide (Fe$_2$(O^{t}Bu)$_6$) [16] and FeCl$_3$ [17], both with H$_2$O as co-reactant. Depositions starting from Fe(II) precursors on the other hand require a more careful selection of the oxidizing agent and deposition temperature to produce pristine films. Rooth et al. [18] reported that ferrocene [Fe(Cp)$_2$] in combined with oxygen enabled the deposition of pure α-Fe$_2$O$_3$ films above 500 °C, whereas a mixture of α-Fe$_2$O$_3$ (hematite) and γ-Fe$_2$O$_3$ (maghemite)/Fe$_3$O$_4$ (magnetite) was obtained at lower temperatures. Conversely, phase-pure α-Fe$_2$O$_3$ films could be fabricated in a broader temperature range by Martinson et al. using

O_3, rather than O_2, as the oxidizing agent [19]. Preparation of single phase Fe(II)-containing films, such as Fe_3O_4, traditionally required post-deposition annealing, as reported by Bachmann et al. [16], using H_2/Ar mixtures. Kukli et al. [20] reduced α-Fe_2O_3 films deposited from ferrocene and O_3 by treatments under H_2/N_2 atmospheres, but phase-pure Fe_3O_4 was not obtained. Direct deposition of Fe_3O_4 was first achieved in 2013 by utilization of a novel precursor, (dimethylaminomethyl)ferrocene (CpFeC$_5$H$_4$CHN(CH$_3$)$_2$), together with O_3 [20]. The direct ALD preparation of phase-pure Fe_3O_4 was also reported by Riha et al. in 2014 [21], combining another novel precursor, bis(2,4-methylpentadienyl)iron (Fe(2,4-C$_7$H$_{11}$)$_2$), with H_2O_2. To the best of our knowledge, no reports on the direct deposition of films exclusively containing Fe(II) by ALD are available in the literature up to date, nor are we aware of any reports on the combination of iron-containing precursors and carboxylic acids to form hybrid materials by MLD.

The current work focuses on the investigation of Fe(hfa)$_2$TMEDA (hfa = 1,1,1,5,5,5-hexafluoro-2,4-pentanedione, TMEDA = N,N,N′,N′-tetramethylethylenediamine) as a possible precursor for the ALD/MLD of Fe(II)-containing compounds. Whereas this precursor has been widely used in CVD and PE-CVD processes to yield various Fe_2O_3 polymorphs [3,22,23], its use in ALD/MLD processes has not been reported so far. The suitability of the precursor for ALD/MLD purposes was tested in combination with water, carboxylic acid, and ozone. Water and ozone are commonly used co-reactants in ALD, while the motivation for the choice of oxalic acid was threefold. First, it presents an intermediate between water and ozone, with respect to reactivity, but could still preserve the oxidation state of iron. In addition, the suitability of dicarboxylic acid for MLD has already been proven [24], thus potentially enabling the first deposition of hybrid thin films containing iron by MLD. Finally, the expected hybrid material would be iron(II) oxalate (FeC$_2$O$_4$), a much used precursor in solid-state chemistry for synthesizing metal oxide nanoparticles by thermal decomposition [25].

2. Experimental

ALD depositions were performed in a F-120 Sat-type ALD-reactor (ASM Microchemistry Ltd) starting from Fe(hfa)$_2$TMEDA, synthesized as previously reported [26,27]. De-ionized water (type 2), anhydrous oxalic acid (Sigma-Aldrich >99%), and O_3, produced from 99.8% O_2 (AGA) in an In USA 2025 ozone generator, were used as co-reactants. N_2 was used as carrier and purging gas, and was separated from air in a nitrogen generator (Schmidlin UHPN3001 N_2 purifier, >99.999% N_2 + Ar purity). Based on previous results [23,24], the vaporization temperatures of Fe(hfa)$_2$TMEDA and oxalic acid were set at 60 and 100 °C, respectively, and the water reservoir was kept at room temperature. Films were deposited on polished 3 cm × 3 cm Si (100) substrates, rinsed in ethanol and blown dry with pressurized air without any pre-etching process. The thickness of the native SiO_2 layer was measured by Spectroscopic ellipsometry (SE) on each substrate prior to deposition and taken into account when determining the film thickness.

SE data was collected using a J. A. Wollam α-SE spectroscopic ellipsometer in the 390–900 nm wavelength range, and subsequently modeled to a Cauchy-function using the CompleteEASE software package, in order to extract thickness and refractive index values (at λ = 632.8 nm).

FTIR measurements were carried out using a Nicolet iS 50 FT-IR Continuum Spectrometer in Attenuated Total Reflectance (ATR) mode. To clarify the data, the signal from a blank Si substrate was subtracted from each spectrum before baseline correction.

In situ QCM analyses were conducted using AT cut quartz crystals (resonance frequency = 6 MHz) mounted on a home-made

holder and recorded using a Maxtek TM-400. The signals were further processed by typically averaging over 16 consecutive cycles, in order to improve statistics. The signal from the QCM analysis was converted from Hz to ng/cycle·cm^2 and ng/cm^2 by calibrating the sensitivity of each sensor with the thickness and density data measured by X-ray reflectivity (XRR) of films deposited separately from the QCM measurements.

GIXRD analyses were performed at an incident angle of ω = 0.23° on a PANalytical Empyrean diffractometer, equipped with a Cu Kα source powered at 45 kV/40 mA (λ = 1.5406 Å), a parallel beam X-ray mirror and a proportional point detector (PW 3011/20). The recorded diffractograms were smoothed using an Origin Lab 9.1 in-built Savizky-Golay method, with a regression window of 30 points. XRR data was obtained from the same instrument used for GIXRD measurements, scanning 2θ from 0.16° to 8°, and analyzed using the X'Pert Reflectivity software provided by PANalytical.

XPS data was acquired using a Thermo Scientific Theta Probe MKII, equipped with a standard Al Kα source (hν = 1486.6 eV), at a total pressure lower than 10^{-8} mbar. Pass energy values of 200 and 50 eV were employed for surveys and detailed scans, respectively. After a Shirley-type background subtraction, raw XPS spectra were fitted using a non-linear least-squares deconvolution program, adopting Gaussian–Lorentzian peak shapes. The reported binding energies (BEs) were corrected for charging effects by assigning the C1s line of adventitious carbon to a position of 284.8 eV [28].

3. Results and discussions

3.1. Depositions with Fe(hfa)$_2$TMEDA, oxalic acid and water

Initial tests with oxalic acid as co-reactant demonstrated viable film growth at a deposition temperature of 200 °C, whereas combination with water did not lead to any detectable film under the same conditions. The Fe(hfa)$_2$TMEDA + oxalic acid system was preliminarily studied by QCM analysis, performed at 130 and 200 °C with the aim of mapping the self-saturating ALD growth conditions (Fig. 1). The pulsing and purging times were varied one by one, and otherwise kept constant at: 2 s Fe(hfa)$_2$TMEDA, 2 s purge, 1.5 s oxalic acid, 1 s purge.

These analyses show that self-saturating conditions are achieved at 130 and 200 °C for both Fe(hfa)$_2$TMEDA and oxalic acid. In the latter case the growth appeared to saturate faster at 200 than at 130 °C. This indicates that the reaction between oxalic acid and the Fe-terminated surface may either be kinetically limited or require a surface rearrangement during growth [29]. The reaction between Fe(hfa)$_2$TMEDA and the oxalic acid-terminated surface was almost unaffected by temperature, and the effects of changes in purging times were relatively modest. Taking the above into account, pulsing and purging parameters chosen for the remainder of the studies were: 1 s Fe(hfa)$_2$TMEDA, 1 s purge, 2 s oxalic acid, 1 s purge.

The growth rate was investigated in the range 125–375 °C (Fig. 2), revealing a reduction in growth per cycle (GPC) with increasing deposition temperature. Three different growth regimes could be identified: the 125–175 °C interval, characterized by a steep decrease in GPC, followed by a plateau between 175 and 200 °C, and slowly decreasing GPC values for temperatures above 200 °C. The refractive index trend, also shown in Fig. 2, divides the growth regime into two parts. Below 200 °C, lower refractive indices are observed, whereas values for deposition temperatures above 200 °C are higher, particularly at 375 °C.

Combining Fe(hfa)$_2$TMEDA and oxalic acid, as in the present work, is expected to result in films of iron(II) oxalate. The thermal behavior of iron(II) oxalate under different atmospheres has been widely studied for more than 40 years [30], with the
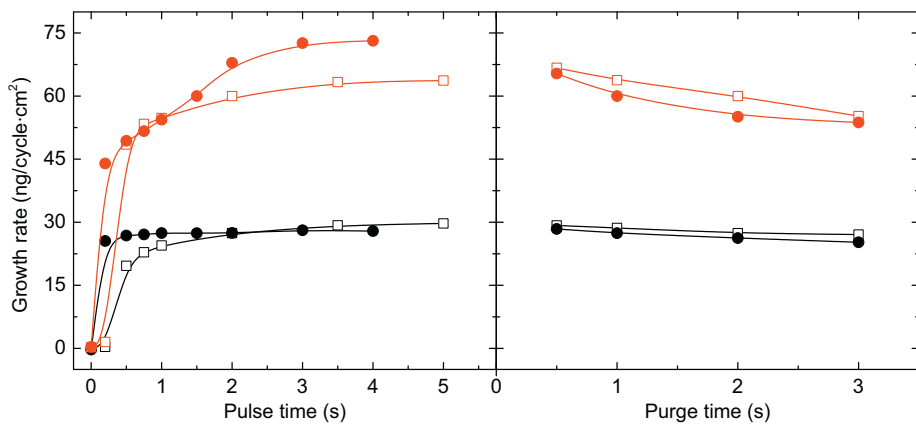
Fig. 1. Individually varied pulse (left) and purge (right) times as measured by QCM at deposition temperatures of 130 °C (red) and 200 °C (black). Open squares represent parameters related to Fe(hfa)$_2$TMEDA, while parameters related to oxalic acid are denoted by closed circles. The uncertainty of the linear fit providing the growth rates are all within the data points. (For interpretation of the references to color in this figure legend, the reader is referred to the web version of this article.)

starting material usually being Fe(COOH)$_2$·2H$_2$O. The crystal structure containing water is stable up to 130 °C [31] or, according to other investigators, 170 °C [25], above which water is lost. Depending on the atmosphere, the anhydrous phase starts to decompose at temperatures as low as 230 °C [25,31]. Interestingly, the different stability regions of iron(II) oxalate overlap quite well with the regimes observed from the GPC of the deposited films. It is worthwhile remembering that, in the absence of O$_2$, iron(II) oxalate decomposes into Fe/Fe$_3$O$_4$, releasing CO and CO$_2$ above 300 °C [30]. Fig. 2 reveals no indication of this process occurring, except for the sudden increase in refractive index at 375 °C, reaching values expected for bulk Fe$_3$O$_4$ [32].

The surface chemical composition of films deposited at selected temperatures was investigated by XPS, revealing the presence of carbon, oxygen, nitrogen and iron. A careful analysis of the Fe2p peak shape and position (Fig. 3a) clearly highlighted the occurrence of Fe(II) species (BE(Fe2p$_{3/2}$) = 710.3 eV; spin–orbit splitting = 13.6 eV; shake-up satellites located 4.3 eV higher than the main components [33–36]).

Regarding C1s and O1s photopeaks, all the investigated films showed qualitatively similar spectral features. As a representative example, peak fitting results for the film deposited at 200 °C are displayed in Fig. 3b and c. The C1s peak could be deconvoluted into three main components: (I), the prevailing one, with BE = 288.9 eV, attributed to C=O bonds; (II), located at BE = 286.5 eV,

due to C—O moieties, and (III), with BE = 284.8 eV, ascribed to C—C bonds and/or adventitious carbon species [34,36]. The O1s signal could be deconvoluted into three contributing bands: (IV), at BE = 532.8 eV, due to oxygen in C—O bonds; (V), with BE = 532.0 eV, attributed to hydroxyl groups and carbonates, and a minor contribution (VI) located at BE = 530.3 eV due to oxide traces [33–36]. Survey scans revealed no traces of fluorine, but rather the presence of nitrogen in all investigated films, and the pertaining signal was more pronounced at lower deposition temperatures (see Supplementary information). The TMEDA ligand of the precursor molecule poses the most plausible source of nitrogen in the films, suggesting an incomplete reaction with oxalic acid during deposition.

In order to attain further insight into the composition of the deposited material, FTIR analyses were performed (Fig. 4). The spectra from films deposited at 200 and 275 °C were relatively similar, whereas the spectral shape at 130 °C appeared to be different.

The broad band around 3300 cm^{-1}, whose intensity decreased upon increasing deposition temperature, could be attributed to the presence of —OH groups [37,38]. The band broadening of the very strong OH band is typical for solid state samples [37]. Bands in the range 3000–2800 cm^{-1}, present in all specimens but more pronounced at lower deposition temperatures, could be traced back to CH$_2$/CH$_3$ stretching modes of TMEDA moieties in the precursor molecule [26]. This is another indication of an incomplete deposition reaction, along with the previously mentioned XPS data (see above and Supplementary information). In the 1700–1400 cm^{-1} interval, the detected signals were assigned to the asymmetric and symmetric stretching vibrations of carboxylate moieties [37,38]. The splitting of these two bands (Δ) can be used as a marker to identify the nature of the interaction between the carboxylate moiety and the metal center [39]. A splitting in the range Δ = 50–150 cm^{-1} indicates a bidentate configuration of the carboxylate group, whereas Δ values between 130–200 cm^{-1} correspond to a bridging coordination. Conversely, Δ values higher than 200 cm^{-1} are associated with a monodentate complex. At a deposition temperature of 130 °C, the splitting was observed to be 57 cm^{-1}, while its values for 200 and 275 °C were 133 and 87 cm^{-1}, respectively. All the measured values were consistent with a bidentate interaction between the ligand and the metal center, although the film prepared at 200 °C could also present bridging interaction. Bands located between 1485 and 1410 cm^{-1} agreed to a good extent with signals from deformation modes of methyl and methylene moieties, especially for a deposition temperature of 130 °C [26]. This supports the more pronounced presence of precursor residuals in films obtained at low deposition temperatures.
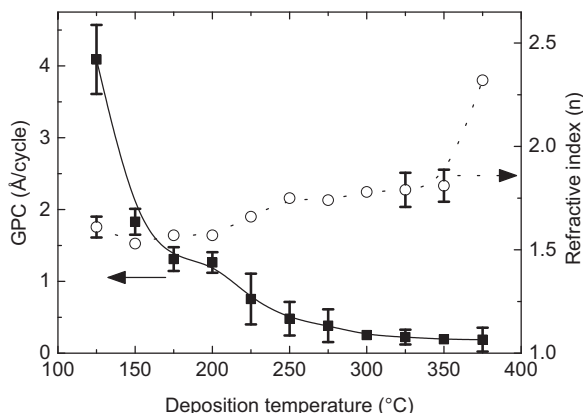

Fig. 2. Growth per cycle (GPC) and refractive index as a function of temperature for films grown from Fe(hfa)$_2$TMEDA + oxalic acid.
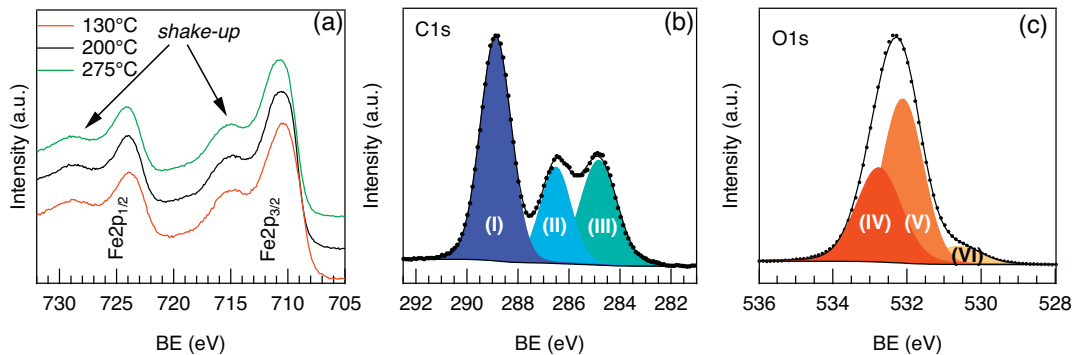
Fig. 3. (a) Surface Fe2p photoelectron peaks for selected specimens synthesized at different temperatures. (b) C1s and (c) O1s photoelectron signals for the sample deposited at 200 °C. For carbon and oxygen, the different fit components are also displayed along with the raw spectrum.
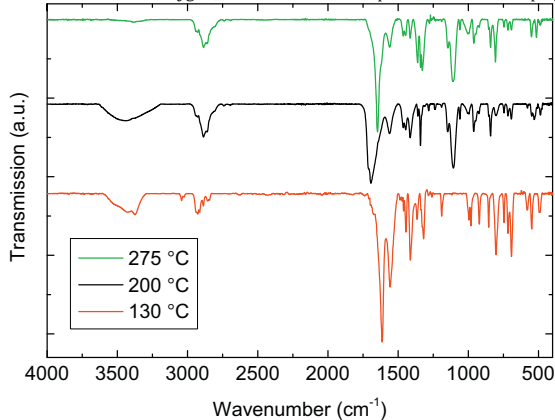

Fig. 4. FTIR spectra of films deposited using Fe(hfa)$_2$TMEDA and oxalic acid at selected growth temperatures.
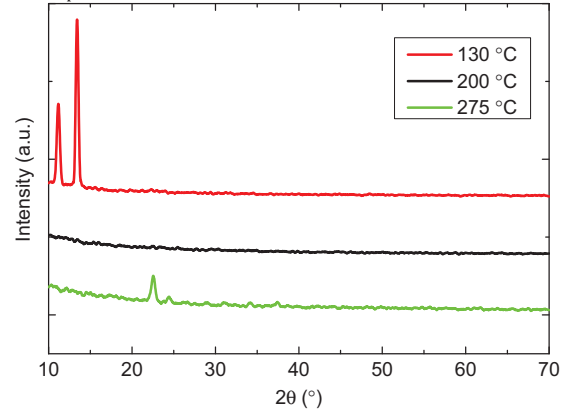

Fig. 5. GIXRD patterns for films deposited using Fe(hfa)$_2$TMEDA and oxalic acid at selected growth temperatures.

The system microstructure was investigated by GIXRD, and representative patterns are displayed in Fig. 5. The recorded data revealed the occurrence of two reflections at low 2θ values (11.2° and 13.4°) for the film deposited at 130 °C. At 200 °C, no appreciable diffraction peaks could be detected, whereas at 275 °C only a very weak reflection at $2\theta = 22.6°$ was observed. In general, deposition of hybrid materials by MLD quite often result in amorphous films, although examples with reflections at low angular values have been reported, as with the present case. These low-angle reflections might originate from a layered structure of the investigated material, rather than traditional crystal lattice diffraction [40]. In the present study, the observed reflections did not match those related to known phases of iron oxalates, hydroxides, oxides or their hydrates, and the limited number prevented a detailed phase attribution.

The growth dynamics of the Fe(hfa)$_2$TMEDA + oxalic acid system was further investigated with QCM by monitoring the signal over longer pulse/purge times at 130 and 200 °C (Fig. 6). At both temperatures, the main mass increase occurred upon exposure to Fe(hfa)$_2$TMEDA. As expected, an immediate drop in mass occurred as oxalic acid was pulsed, resulting from the reaction with, and subsequent removal of, the heavy precursor ligands from the surface. The steady, minor mass gain observed throughout each pulse of both reactants indicated some physisorption of precursor molecules, on top of the already saturated surface. However, immediate desorption was visible through the mass decrease during the subsequent purges. The overall mass increase over a complete cycle was larger at 130 than 200 °C, as expected from the higher growth rate at lower temperature.
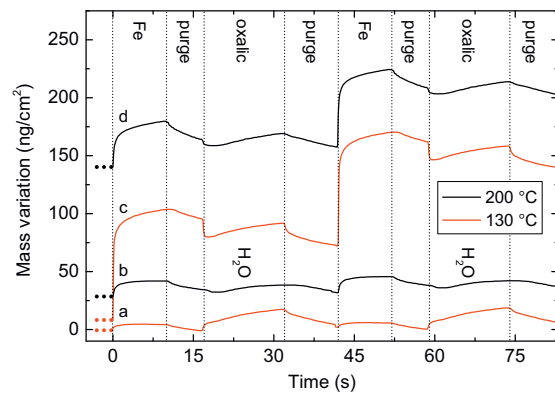

Fig. 6. Mass variations as recorded by QCM during pulsing and purging of Fe(hfa)$_2$TMEDA (denoted Fe) and water at 130 °C (a) and 200 °C (b), with one cycle consisting of: 10 s Fe(hfa)$_2$TMEDA + 7 s purge + 15 s H$_2$O + 10 s purge. Also, mass variations as recorded by QCM during pulsing and purging of Fe(hfa)$_2$TMEDA (denoted Fe) and oxalic acid at 130 °C (c) and 200 °C (d), with one cycle consisting of: 10 s Fe(hfa)$_2$TMEDA + 7 s purge + 15 s oxalic acid + 10 s. Uncertainty is within the width of the lines.

In general, an ALD cycle can be divided into four parts: (1a) chemisorption of the first reactant (typically a metal reactant); (1b) purge to remove unreacted precursor and gaseous by-products; (2a) chemisorption of a second reactant (typically a metal-free one); (2b) purge to remove unreacted precursor and gaseous by-products [11]. The mass gain/loss from the two half-cycle reactions

Table 1

Mass changes for half-cycle reactions and mass change ratios at selected deposition temperatures, as measured by QCM.

T (°C)	m_1 (ng/cm^2)	m_2 (ng/cm^2)	Δm
130	89.86	−23.25	−0.26
200	51.44	−6.74	−0.13

(1) and (2) can be defined as m_1 and m_2. A relative, dimensionless, mass change ration over a complete cycle can be calculated from:

$$\Delta m = \frac{m_2}{m_1} \qquad (3.1)$$

The recorded mass variations in Fig. 6 enabled estimation of the mass gain/loss and corresponding Δm values (Table 1).

The experimental data presented so far can be rationalized in relation to the possible reaction mechanisms, proposed by calculating the Δm values from possible reaction routes and comparing them with the experimental data. A first reasonable route (a) for the two half-cycle reactions could be the following:

$$2\cdot|{-}COOH + Fe(hfa)_2TMEDA(g) \rightarrow$$

$$|{-}(COO)_2{-}FeTMEDA + 2Hhfa(g) \qquad (3.2)$$

$$|{-}(COO)_2{-}FeTMEDA + (COOH)_2(g) \rightarrow$$

$$|{-}(COO)_2{-}Fe{-}(OCOH)_2 + TMEDA(g) \qquad (3.3)$$
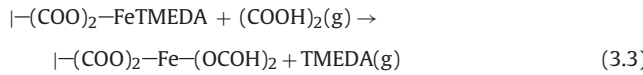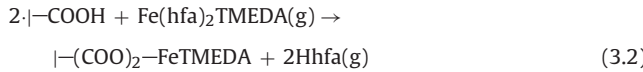
where | symbolizes the surface. In Eq. (3.2), two surface −COOH groups react with gaseous Fe(hfa)$_2$TMEDA. The −COOH groups can transfer hydrogen to hfa, resulting in the protonated ligand (Hhfa) release, whereas the TMEDA ligand remains bonded to Fe. By subtracting the molar mass of the outgoing group (2Hhfa in Eq. (3.2)) from the incoming precursor (Fe(hfa)$_2$TMEDA in Eq. (3.2)), the mass increase for this reaction step can be calculated, yielding m_{a1} = 170.04 g/mol. In Eq. (3.3), the incoming oxalic acid bonds as a bidentate ligand to Fe and, simultaneously, TMEDA is released. The corresponding mass change is m_{a2} = −26.17 g/mol. Considering the whole cycle and based on Eq. (3.1), a Δm_a value of −0.15 is obtained, in good agreement with the observed Δm at a deposition temperature of 200 °C (see Table 1). Nevertheless, the observed Δm at 130 °C is appreciably higher, suggesting the occurrence of a different reaction mechanism. Taking into account the presence of N in the films arising from TMEDA moieties (see above and Supplementary information), a second mechanism (b) can be proposed:

$$|{-}COOH + Fe(hfa)_2TMEDA(g) \rightarrow$$

$$|{-}COO{-}Fe(hfa)TMEDA + Hhfa(g) \qquad (3.4)$$

$$|{-}COO{-}Fe(hfa)TMEDA + (COOH)_2(g) \rightarrow$$

$$|{-}COO{-}FeTMEDA{-}(OCO)(OCOH) + Hhfa(g) \qquad (3.5)$$
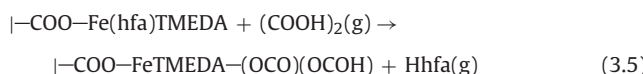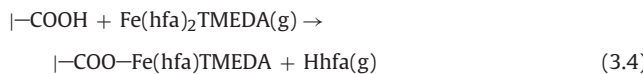
In reaction (3.4), one of the hfa groups is displaced from Fe(hfa)$_2$TMEDA as the surface −COOH protonates it to yield Hhfa, and the remaining COO$^-$ bonds to Fe. The mass increase for this reaction step is m_{b1} = 378.10 g/mol. In the second step (3.5), the remaining hfa group leaves as Hhfa after receiving H from the incoming oxalic acid, which bonds to the iron center. Correspondingly, the mass difference is m_{b2} = −118.02 g/mol. Unlike the previous case (a), the TMEDA group remains bonded to Fe (b) and is incorporated into the film. The mass change ratio calculated according to Eq. (3.1), Δm_b = −0.31, is slightly higher than the observed mass change ratio for a deposition temperature of 130 °C (Table 1). An explanation for this difference can be the concomitant occurrence of both of the proposed reaction routes (a) and (b). Supposing
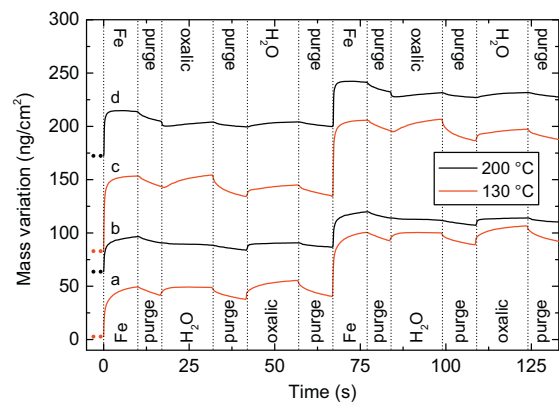

Fig. 7. Mass variations as recorded by QCM during different sequences of pulsing and purging of Fe(hfa)$_2$TMEDA (denoted Fe), H$_2$O and oxalic acid at 130 °C (a and c) and 200 °C (b and d). For a and b one cycle consisted of: 10 s Fe(hfa)$_2$TMEDA + 7 s purge + 15 s H$_2$O + 10 s purge + 15 s oxalic acid + 10 s purge. For c and d one cycle consisted of: 10 s Fe(hfa)$_2$TMEDA + 7 s purge + 15 s oxalic acid + 10 s purge + 15 s H$_2$O + 10 s purge. Uncertainty is within the width of the lines.

that half of the reactions follow route (a) and the other half route (b), the average Δm would be −0.23, close to the observed Δm recorded at 130 °C (Table 1). Nevertheless, other reactions might also come into play and a detailed discussion of this issue requires further investigation on the process mechanism.

The reactivity of Fe(hfa)$_2$TMEDA with water was also investigated, but as evidenced in Fig. 6 no significant mass gain took place, irrespective of the adopted temperature. Nevertheless, various pulse sequences of Fe(hfa)$_2$TMEDA, oxalic acid and water were studied by QCM to further investigate the possible influence of water introduction on the target process (Fig. 7).

From the data in Fig. 7 it was evident that the mass deposited over a complete cycle was unaffected by the pulsing order. As with only Fe(hfa)$_2$TMEDA + oxalic acid (Fig. 6), the growth rate was somewhat higher at lower temperature. A detailed comparison of the data presented in Figs. 6 and 7 revealed that the amount of deposited mass over a complete cycle was actually slightly lower when both water and oxalic acid took part in the process, as opposed to only oxalic acid. Thus, suggesting that water had a limiting effect on the deposition reaction.

3.2. Depositions with Fe(hfa)$_2$TMEDA and O$_3$

The Fe(hfa)$_2$TMEDA precursor was also combined with ozone in the aim of depositing iron(III) oxide films. The pulse and purge parameters for Fe(hfa)$_2$TMEDA were chosen based on the results from using oxalic acid (Fig. 1) while the parameters for ozone were chosen based on previous experience with similar systems [15]. No attempts were made at performing a QCM measurement since ozone obscures the signal due to the thermal load from decomposition of ozone. However, the dependence of deposition temperature on growth rate and refractive index was investigated in the range 150–350 °C (Fig. 8). The results revealed lower or similar growth rates compared with other iron oxide ALD processes using O$_3$ [15,16,41]. No ALD window with constant growth rate was observed, instead the growth per cycle increased linearly with deposition temperature throughout the investigated range. For temperatures above 250 °C, the refractive index stabilized at ≈2.8, a value, comparable with the one pertaining to bulk α-Fe$_2$O$_3$ [32].

XPS analyses evidenced the presence of Fe(III) free from other iron oxidation states [22,23,28] for films deposited at 200 and 300 °C (Fig. 9). In agreement with these data, GIXRD analysis
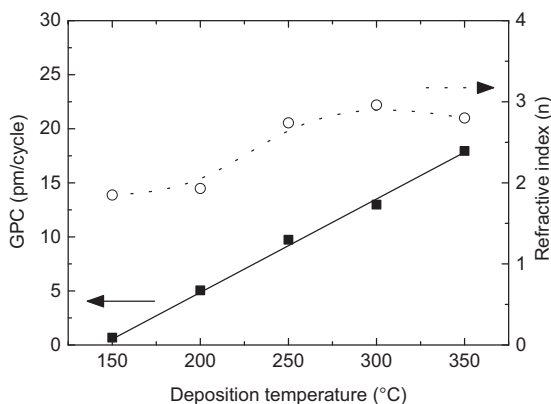
Fig. 8. Growth per cycle (GPC) and refractive index of films deposited with Fe(hfa)$_2$TMEDA and ozone as a function of temperature. The pusle and purge times used were: 1 s Fe(hfa)$_2$TMEDA + 1 s purge + 2 s O$_3$ + 2 s purge. All error bars are within data points.
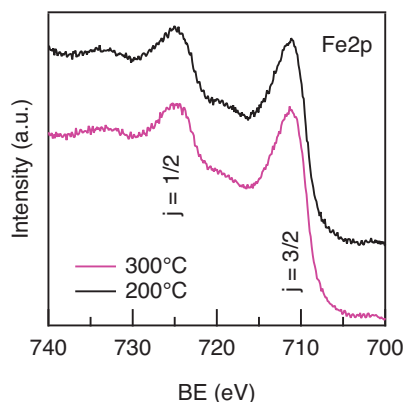

**Fig. 9.** Surface Fe2p photoelectron peaks for selected specimens deposited at different temperatures.
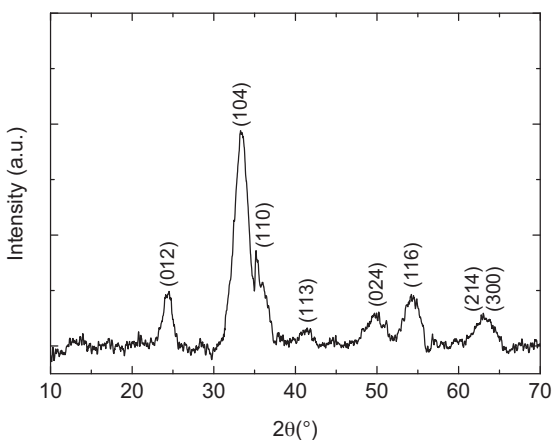
Fig. 10. GIXRD pattern for a film deposited by pulsing Fe(hfa)$_2$TMEDA + O$_3$ at 350 °C.

yielded reflections that corresponded to those expected for α-Fe$_2$O$_3$ (Fig. 10) [42].

The current growth system results in relatively low growth rates, as compared to most other ALD deposition systems. This may be due to the size of the chemisorbed Fe(hfa)$_2$TMEDA fragment, limiting the access to reaction sites [29]. Even though such

low growth rates may seem as a drawback, it may be exploited for introduction of dopants in a diluted manner, i.e. without clustering, as an alternative to active inhibition of growth [43].

4. Conclusions

The present work was aimed at investigating the suitability of Fe(hfa)$_2$TMEDA for ALD/MLD applications, with particular attention to maintaining the divalent oxidation state of iron in the resulting films. Depositions with O$_3$ as co-reactant resulted in Fe$_2$O$_3$ films, as expected due to the oxidizing nature of ozone. Nevertheless, using oxalic acid as co-reactant led to Fe(II)-containing materials throughout the investigated growth temperature range, as demonstrated by XPS analyses. The use of water as co-reactant, either alone or in combination with oxalic acid, was not favorable over oxalic acid itself. The Fe(hfa)$_2$TMEDA + oxalic acid system did not evidence the occurrence of any temperature range wherein the growth rate remained unchanged, as typically observed for ALD processes. However, QCM analyses revealed a self-limiting surface saturation at the investigated temperatures. The resulting hybrid films could possibly be decomposed at moderate temperatures to remove organic constituents. In addition, the present ALD process, in combination with TiO$_2$ deposition and thermal treatment could pave the way to the fabrication of FeTiO$_3$, a very interesting material when combined with Fe$_2$O$_3$. To this regard, our future attention will be devoted both to the preparation of such materials, as well as to a detailed investigation of hybrid systems obtained by the developed MLD route. Efforts in this direction are already under way.

Acknowledgements

Appendix A. Supplementary data

Supplementary data associated with this article can be found, in the online version, at http://dx.doi.org/10.1016/j.apsusc.2015.04.154

References

[1] P. Tartaj, M.P. Morales, T. Gonzalez-Carreño, S. Veintemillas-Verdaguer, C.J. Serna, The iron oxides strike back: from biomedical applications to energy storage devices and photoelectrochemical water splitting, Adv. Mater. 23 (2011) 5243–5249.
[2] G. Carraro, D. Barreca, M. Cruz-Yusta, A. Gasparotto, C. Maccato, J. Morales, C. Sada, L. Sánchez, Vapor-phase fabrication of β-iron oxide nanopyramids for lithium-ion battery anodes, ChemPhysChem 13 (2012) 3798–3801.
[3] G. Carraro, C. Maccato, A. Gasparotto, T. Montini, S. Turner, O.I. Lebedev, V. Gombac, G. Adami, G. Van Tendeloo, D. Barreca, P. Fornasiero, Enhanced hydrogen production by photoreforming of renewable oxygenates through nanostructured Fe$_2$O$_3$ polymorphs, Adv. Funct. Mater. 24 (2014) 372–378.
[4] R. Mantovan, S. Vangelista, B. Kutrzeba-Kotowska, A. Lamperti, N. Manca, L. Pellegrino, M. Fanciulli, Fe$_{3-\delta}$O$_4$/MgO/Co magnetic tunnel junctions synthesized by full in situ atomic layer and chemical vapour deposition, J. Phys. D: Appl. Phys. 47 (2014) 102002.
[5] S.A. McEnroe, B. Carter-Stiglitz, R.J. Harrison, P. Robinson, K. Fabian, C. McCammon, Magnetic exchange bias of more than 1 Tesla in a natural mineral intergrowth, Nat. Nanotechnol. 2 (2007) 631–634.
[6] K. Fabian, S.A. McEnroe, P. Robinson, V.P. Shcherbakov, Exchange bias identifies lamellar magnetism as the origin of the natural remanent magnetization in titanohematite with ilmenite exsolution from Modum, Norway, Earth Planet. Sci. Lett. 268 (2008) 339–353.

[7] Y. Ishikawa, S. Akimoto, Magnetic properties of the FeTiO$_3$–Fe$_2$O$_3$ solid-solution series, J. Phys. Soc. Jpn. 12 (1957) 1083–1098.

[8] Y. Ishikawa, Electrical properties of FeTiO$_3$–Fe$_2$O$_3$ solid solution series, J. Phys. Soc. Jpn. 13 (1958) 37–42.

[9] H. Hojo, K. Fujita, K. Tanaka, K. Hirao, Room-temperature ferrimagnetic semiconductor 0.6FeTiO$_3$·0.4Fe$_2$O$_3$ solid solution thin films, Appl. Phys. Lett. 89 (2006) 142503.

[10] R.K. Pandey, P. Padmini, P. Kale, J. Dou, C. Lohn, R. Schad, R. Wilkins, W. Geerts, Multifunctional nature of modified iron titanates and their potential applications, Ceram. Trans. 226 (2011) 61–75.

[11] V. Miikkulainen, M. Leskelä, M. Ritala, R.L. Puurunen, Crystallinity of inorganic films grown by atomic layer deposition: overview and general trends, J. Appl. Phys. 113 (2013) 021301.

[12] C. Wiemer, L. Lamagna, M. Fanciulli, Atomic layer deposition of rare-earth-based binary and ternary oxides for microelectronic applications, Semicond. Sci. Technol. 27 (2012) 074013.

[13] M. de Ridder, P.C. van de Ven, R.G. van Welzenis, H.H. Brongersma, S. Helfensteyn, C. Creemers, P. Van Der Voort, M. Baltes, M. Mathieu, E.F. Vansant, Growth of iron oxide on yttria-stabilized zirconia by atomic layer deposition, J. Phys. Chem. B 106 (2002) 13146–13153.

[14] O. Nilsen, M. Lie, S. Foss, H. Fjellvåg, A. Kjekshus, Effect of magnetic field on the growth of α-Fe$_2$O$_3$ thin films by atomic layer deposition, Appl. Surf. Sci. 227 (2004) 40–47.

[15] M. Lie, H. Fjellvåg, A. Kjekshus, Growth of Fe$_2$O$_3$ thin films by atomic layer deposition, Thin Solid Films 488 (2005) 74–81.

[16] J. Bachmann, J. Jing, M. Knez, S. Barth, H. Shen, S. Mathur, U. Gösele, K. Nielsch, Ordered iron oxide nanotube arrays of controlled geometry and tunable magnetism by atomic layer deposition, J. Am. Chem. Soc. 129 (2007) 9554–9555.

[17] M. Aronniemi, J. Saino, J. Lahtinen, Characterization and gas-sensing behavior of an iron oxide thin film prepared by atomic layer deposition, Thin Solid Films 516 (2008) 6110–6115.

[18] M. Rooth, A. Johansson, K. Kukli, J. Aarik, M. Boman, A. Hårsta, Atomic layer deposition of iron oxide thin films and nanotubes using ferrocene and oxygen as precursors, Chem. Vap. Deposition 14 (2008) 67–70.

[19] A.B.F. Martinson, M.J. DeVries, J.A. Libera, S.T. Christensen, J.T. Hupp, M.J. Pellin, J.W. Elam, Atomic layer deposition of Fe$_2$O$_3$ using ferrocene and ozone, J. Phys. Chem. C 115 (2011) 4333–4339.

[20] K. Kukli, M.C. Dimri, A. Tamm, M. Kemell, T. Käämbre, M. Vehkamäki, M. Puttaswamy, R. Stern, I. Kuusik, A. Kikas, M. Tallarida, D. Schmeisser, M. Ritala, M. Leskelä, Structural magnetic studies on iron oxide and iron–magnesium oxide thin films deposited using ferrocene and (dimethylaminomethyl)ferrocene precursors, ECS J. Solid State Sci. Technol. 2 (2013) N45–N54.

[21] S.C. Riha, J.M. Racowski, M.P. Lanci, J.A. Klug, A.S. Hock, A.B. Martinson, Phase discrimination through oxidant selection in low-temperature atomic layer deposition of crystalline iron oxides, Langmuir 29 (2013) 3439–3445.

[22] G. Carraro, A. Gasparotto, C. Maccato, E. Bontempi, O.I. Lebedev, S. Turner, C. Sada, L.E. Depero, G. Van Tendeloo, D. Barreca, Fluorine doped Fe$_2$O$_3$ nanostructures by a one-pot plasma-assisted strategy, RSC Adv. 3 (2013) 23762.

[23] G. Carraro, C. Maccato, E. Bontempi, A. Gasparotto, O.I. Lebedev, S. Turner, L.E. Depero, G. Van Tendeloo, D. Barreca, Insights on growth and nanoscopic investigation of uncommon iron oxide polymorphs, Eur. J. Inorg. Chem. 2013 (2013) 5454–5461.

[24] K.B. Klepper, O. Nilsen, P.A. Hansen, H. Fjellvåg, Atomic layer deposition of organic–inorganic hybrid materials based on saturated linear carboxylic acids, Dalton Trans. 40 (2011) 4636–4646.

[25] M. Hermanek, R. Zboril, M. Mashlan, L. Machala, O. Schneeweiss, Thermal behaviour of iron(II) oxalate dihydrate in the atmosphere of its conversion gases, J. Mater. Chem. 16 (2006) 1273.

[26] D. Barreca, G. Carraro, A. Gasparotto, C. Maccato, R. Seraglia, G. Tabacchi, An iron(II) diamine diketonate molecular complex: synthesis, characterization and application in the CVD of Fe$_2$O$_3$ thin films, Inorg. Chim. Acta 380 (2012) 161–166.

[27] D. Barreca, G. Carraro, A. Devi, E. Fois, A. Gasparotto, R. Seraglia, C. Maccato, C. Sada, G. Tabacchi, E. Tondello, A. Venzo, M. Winter, β-Fe$_2$O$_3$ nanomaterials from an iron(II) diketonate–diamine complex: a study from molecular precursor to growth process, Dalton Trans. 41 (2012) 149–155.

[28] D. Briggs, M.P. Seah, Practical Surface Analysis, second ed., Wiley, New York, NY, 1990.

[29] M. Ylilammi, Monolayer thickness in atomic layer deposition, Thin Solid Films 279 (1996) 124–130.

[30] G.C. Nicholson, The thermal decomposition of ferrous oxalate dihydrate, J. Inorg. Nucl. Chem. 29 (1967) 1599–1604.

[31] R.L. Frost, M.L. Weier, Thermal decomposition of humboldtine—a high resolution thermogravimetric and hot stage Raman spectroscopic study, J. Therm. Anal. Calorim. 75 (2004) 277–291.

[32] R.M. Cornell, U. Schwertmann, The Iron Oxides: Structure, Properties, Reactions Occurrences and Uses, second ed., Wiley-VCH, Weinheim, 2003.

[33] W. Su, J.O. Iroh, IR and XPS studies on the interphase and poly(N-methylpyrrole) coatings electrodeposited on steel substrates, Electrochim. Acta 44 (1999) 3321–3332.

[34] W. Prissanaroon-Ouajai, P.J. Pigram, R. Jones, A. Sirivat, A sensitive and highly stable polypyrrole-based pH sensor with hydroquinone monosulfonate and oxalate co-doping, Sens. Actuators, B: Chem. 138 (2009) 504–511.

[35] NIST X-ray Photoelectron Spectroscopy Database, Version 4.1, National Institute of Standards and Technology, Gaithersburg, 2012; http://srdata.nist.gov/xps/

[36] J.F. Moulder, W.F. Stickle, P.E. Sobol, K.D. Bomben, Handbook of X-ray photoelectron spectroscopy, second ed., Perkin-Elmer Corporation, Eden Prairie, MN, 1992.

[37] R.M. Silverstein, F.X. Webster, D.J. Kiemle, Spectrometric Identification of Organic Compounds, seventh ed., John Wiley & Sons Inc., Hoboken, NJ, 2005.

[38] H.F. Shurvell, Sample characterisation and spectral data processing, in: J.M. Chalmers, P.R. Griffiths (Eds.), Handbook of Vibrational Spectroscopy, vol. 3, John Wiley & Sons Ltd., Chichester, 2002, pp. 1783–1816.

[39] F. Verpoort, T. Haemers, P. Roose, J.-P. Maes, Characterization of a surface coating formed from carboxylic acid-based coolants, Appl. Spectrosc. 53 (1999) 1528–1534.

[40] K.B. Klepper, O. Nilsen, S. Francis, H. Fjellvåg, Guidance of growth mode and structural character in organic–inorganic hybrid materials—a comparative study, Dalton Trans. 43 (2014) 3492–3500.

[41] B.M. Klahr, A.B. Martinson, T.W. Hamann, Photoelectrochemical investigation of ultrathin film iron oxide solar cells prepared by atomic layer deposition, Langmuir 27 (2011) 461–468.

[42] Pattern no. 00-033-0664, JCPDS (2000).

[43] S.B. Ogale, Dilute doping, defects, and ferromagnetism in metal oxide systems, Adv. Mater. 22 (2010) 3125–3155.